

The Pennsylvania State University
The Graduate School
College of Engineering

SHARP-EDGE-BASED ACOUSTOFLUIDICS

A Dissertation in
Engineering Science and Mechanics
by
Po-Hsun Huang

© 2016 Po-Hsun Huang

Submitted in Partial Fulfillment
of the Requirements
for the Degree of

Doctor of Philosophy

August 2016

The dissertation of Po-Hsun Huang was reviewed and approved* by the following:

Tony Jun Huang
Professor of Engineering Science and Mechanics
Dissertation Advisor, Chair of Committee

Bernhard R. Tittmann
Schell Professor of Engineering Science and Mechanics

Francesco Costanzo
Professor of Engineering Science and Mechanics

Corina Drapaca
Associate Professor of Engineering Science and Mechanics

Siyang Zheng
Associate Professor of Biomedical Engineering

Judith A. Todd
Professor of Engineering Science and Mechanics
P. B. Breneman Department Head of Engineering Science and Mechanics

*Signatures are on file in the Graduate School.

Abstract

Over the past few decades, microfluidics has emerged as a powerful tool for a wide variety of applications, from chemical applications, such as monitoring of chemical reactions and material synthesis, to biological applications, such as cell differentiation and single-cell analysis. We have also witnessed the rapid advancement of related technologies. Despite the advancement, the adoption of microfluidic devices in daily human life for diagnostic and therapeutic purposes is still very limited, the reason being that to date, only a few powerful fluid manipulation devices have been proposed. This thesis has centered on understanding, designing, and prototyping a new class of acoustofluidic (*i.e.*, the fusion of acoustics and microfluidics) devices to pave the foundation for applications, ranging from biomedical/chemical research to clinical applications. Implementing the acoustic streaming effect induced by oscillating sharp-edge structures in microfluidics, we have developed a series of sharp-edge-based acoustofluidic technologies that are able to control and manipulate fluids and micro-objects.

First of all, an acoustofluidic micromixer is developed where rapid and homogeneous mixing of fluid was achieved *via* the acoustic streaming induced by oscillating sharp-edge structures. The acoustic streaming induced by the oscillation of sharp-edge structures allows two fluids to interchange and thus enhances the mass transport across the channel, greatly improving the mixing efficiency. Our sharp-edge-based acoustofluidic micromixer possesses desirable characteristics, including excellent mixing performance, simplicity, convenient and stable operation, fast mixing speed, and ability to be toggled on-and-off, which makes it a promising candidate for a wide variety of lab-on-a-chip applications.

Built directly on the sharp-edge-based acoustofluidic micromixer, a modified sharp-edge-based acoustofluidic micromixer is developed for the mixing of highly-viscous fluid samples. The capability of our sharp-edge-based acoustofluidic micromixer for the mixing of highly-viscous samples is demonstrated by liquefying

human sputum samples on-chip, which, to the best of our knowledge, is the first microfluidic sputum liquefaction device, also known as acoustofluidic sputum liquefier. Our sharp-edge-based acoustofluidic sputum liquefier is a promising candidate for incorporation with other on-chip components that will enable the development of a fully integrated, self-contained sputum processing and analysis platform. In addition, our device can possibly be employed for applications that require the processing of highly viscous fluids.

By engineering the acoustic streaming patterns generated inside the microfluidic channel, a sharp-edge-based acoustofluidic chemical gradient generator is presented. The generation of concentration gradients of chemical is due to the serial mixing of different solutions. Through the modulation of the driving signals of piezoelectric transducer, our sharp-edge-based acoustofluidic gradient generator can generate spatiotemporally controllable concentration gradients. The biocompatibility of our sharp-edge-based acoustofluidic gradient generator is validated by carrying out experiments of cell migration, as well as by preserving the cell viability after long-term exposure to an acoustic field. Our device features advantages such as simple fabrication and operation, compact and biocompatible device, and generation of spatiotemporally tunable gradients.

Finally, to expand the potential of the acoustic streaming induced by oscillating sharp-edge structure, a highly reliable, programmable acoustofluidic micropump is developed. By engineering the geometry of sharp-edge structure, specifically, tilting the sharp-edge structure, the acoustic streaming pattern generated inside the channel is altered. This altered streaming pattern then produces a net force pointing toward the direction where the sharp-edge structure is tilted; as a result of the net force, fluid pumping motion occurs along the parallel direction where the sharp-edge structure was tilted. Our sharp-edge-based acoustofluidic micropump offers advantages over other microfluidic pumps in terms of not only simplicity, stability, reliability and cost-effectiveness, but also controllability and flexibility, which, when combined, make it valuable for many lab-on-a-chip applications.

To sum up, a series of acoustofluidic devices are developed and presented to control and manipulate fluids *via* the acoustic streaming effect induced by oscillating sharp-edge structures. Due to the advantages of high biocompatibility, ease of manipulation, high flexibility and controllability, and low power consumption, the acoustofluidic technologies that we have developed are invaluable for many microfluidic applications. The work presented in this dissertation serves as an important example and the foundation for the future development of sharp-edge-based acoustofluidic devices.

Table of Contents

List of Figures	viii
Acknowledgments	xvii
Chapter 1	
Motivation and Overview	1
1.1 Acoustic streaming	1
1.2 Literature review	2
1.2.1 Acoustic streaming based on oscillating bubbles	2
1.2.1.1 Fluid mixing based on oscillating microbubbles	3
1.2.1.2 Fluid pumping based on oscillating microbubbles	5
1.2.2 Acoustic streaming based on oscillating flow	7
1.3 Motivation	9
1.4 Dissertation outline	10
Chapter 2	
Acoustic streaming by oscillating sharp-edge structures	13
2.1 Generation of acoustic streaming by oscillating sharp-edge structures	13
2.1.1 Acoustic streaming effect under no background flow	15
2.1.2 Acoustic streaming effect under a background flow	17
2.2 Numerics of acoustic streaming effect induced by oscillating sharp-edge structure	18
2.2.1 Governing equations	19
2.2.2 Boundary Conditions	21
2.2.2.1 Actuation for sharp-edge devices	21
2.2.2.2 Periodic Boundary Conditions	22
2.2.2.3 Boundary conditions on second-order problem	22

2.2.3	Mean trajectories	23
2.2.4	Numerical Implementation	25
2.2.5	Overview of algorithm	25
2.3	Summary	26
Chapter 3		
	Sharp-edge-based acoustofluidic micromixer	27
3.1	Motivation	27
3.2	Working mechanism	29
3.3	Results and Discussions	30
3.3.1	Determination of driving frequency	30
3.3.2	Mixing performances of various tip angles	32
3.3.3	Mixing performances under different driving voltages	36
3.3.4	Mixing performances under different flow rates	38
3.4	Summary	39
Chapter 4		
	Sharp-edge-based acoustofluidic sputum liquefier	41
4.1	Motivation	41
4.1.1	Standard liquefaction procedure	43
4.2	Working concept	43
4.3	Materials and methods	46
4.3.1	Device fabrication and operation	46
4.3.2	Determination of device working frequency	48
4.3.3	Mixing performance inside the channel	49
4.3.4	Human sputum samples	51
4.3.5	Cell Viability	51
4.3.6	Modified Wright-Giemsa staining	51
4.3.7	Statistical analysis	52
4.4	Results and discussion	52
4.4.1	Visual comparison	52
4.4.2	Viability of cells in liquefied sputum samples	53
4.4.3	Cells morphology and identification of immune cells	54
4.4.4	Flow cytometry analysis	56
4.5	Summary	57
Chapter 5		
	Sharp-edge-based acoustofluidic chemical gradient generator	59
5.1	Motivation	60

5.2	Concept and device design	62
5.3	Materials and methods	65
5.3.1	Experiment setup and operation	65
5.3.2	Determination of device working frequency	66
5.3.3	Cell preparation	67
5.3.4	Cell migration	67
5.3.5	Cell viability	68
5.3.6	Statistical analysis	69
5.4	Results and discussion	70
5.4.1	Characterization of flow patterns in the gradient generator	70
5.4.2	Generation of concentration gradients	71
5.4.3	The effect of flow rate on the gradient generation	74
5.4.4	Temporal control of gradient generation	76
5.4.5	Cell migration in our acoustofluidic device	78
5.4.6	Cell viability in the presence of lasting acoustic field	79
5.5	Summary	81
Chapter 6		
Sharp-edge-based acoustofluidic micropump		83
6.1	Motivation	84
6.1.1	Device design and concept	85
6.2	Results and discussion	87
6.2.1	Streaming patterns and numerical simulations	87
6.2.2	Visualization and characterization of pumping performance	87
6.3	Summary	91
Chapter 7		
Conclusions and Prospects		93
7.1	Conclusions	93
7.2	Prospects	96
Bibliography		99

List of Figures

1.1	Schematic showing the category of acoustic streaming based on different generating mechanisms: (a) bulk-driven acoustic streaming, and (b) boundary-driven acoustic streaming. Green arrows: steady flow. Blue region: bulk of fluid. Pink lines: acoustic wave. Dark blue: boundary layers. This figure is adopted and reproduced from Ref. [4].	3
1.2	(Left) Schematics showing the experimental setup of the micromixer based on the oscillating microbubbles trapped in sidewall pre-defined cavities. (Right) Experimental images and characterization plot showing the mixing performance of two different liquids achieved by the bubble-based mixer. This figure is adopted and reproduced from Ref. [11].	4
1.3	(a) Schematic showing the experimental configuration of micropump based on a single microbubble by Cho <i>et al.</i> [13]. (b) Schematic showing the working concept of the micropump based on multiple microbubbles trapped in later cavities inside a microfluidic channel by Tovar and Lee [10]. This figure is adopted and reproduced from Ref. [10, 13]	5
1.4	Experimental images showing the expanding up of microbubbles over time during operation: (a) $t_0 = 0$ sec, (b) $t_1 = 3$ sec, and (c) $t_2 = 6$ sec. This would lead to the variation in the bubble size of each bubble and as a result, alter the driving frequency. Scale bar: $450 \mu\text{m}$	6
1.5	(a) Schematics showing the experimental setup and concept for the device that oscillates flow around solid structures to induce microeddies, <i>i.e.</i> , acoustic streaming. (b) Experimental and numerical images showing the streaming patterns when an oscillating flow is introduced around various geometries of solid structure in the channel. This figure is adopted and reproduced from Ref. [27].	8

1.6	(a) Fluorescent image showing acoustic streaming patterns under an oscillating flow when multiple solid structures are constructed in the channel. (b) Experimental image showing the trapping of 10 μm polystyrene particles. This figure is adopted and reproduced from Ref. [28].	9
2.1	(a) Schematic of the device showing a micro-fluidics channel with sharp-edge structures on its sidewalls. The channel walls are subjected to a time-harmonic excitation produced by a piezoelectric transducer placed on one side of the channel. (b) Typical micro streaming patterns produced in the fluid occupying the channel as a response to piezoelectric excitation. (c) Typical geometric dimensions of the corrugated channel.	14
2.2	Arrangement of the PDMS channel and piezoelectric transducer. . .	15
2.3	Fluorescent images showing flow patterns visualized using dragon-green fluorescent beads seeded randomly inside the channel under no background flow at different voltages: (a) 0 V_{PP} , <i>i.e.</i> , switched-OFF, (b) 10 V_{PP} , (c) 20 V_{PP} , (d) 30 V_{PP} , (e) 40 V_{PP} , and (f) 50 V_{PP} . When the piezoelectric transducer was inactivated (<i>i.e.</i> , switched OFF), the fluorescent beads remained stationary inside the channel. Once the piezoelectric transducer was activated under a driving voltage of 10 V_{PP} , acoustic streaming effect was developed around the tip of each sharp-edge structure and as the driving voltage was further increased, the strength of acoustic streaming effect was enhanced accordingly. Scale bar: 250 μm	16
2.4	Fluorescent images showing flow patterns visualized using dragon-green fluorescent beads seeded randomly inside the channel under a background flow at different voltages: (a) 0 V_{PP} , <i>i.e.</i> , switched-OFF, (b) 10 V_{PP} , (c) 20 V_{PP} , (d) 30 V_{PP} , (e) 40 V_{PP} , and (f) 50 V_{PP} . Upon the introduction of a background flow (from left to right), a laminar flow pattern was observed when the piezoelectric transducer was switched-OFF. Though the piezoelectric transducer was switched-ON with a driving voltage of 10 V_{PP} , the acoustic streaming effect could be hardly developed around the tip of each sharp-edge structure. Once the voltage was further increased from 10 V_{PP} to 50 V_{PP} , the asymmetric acoustic streaming patterns were generated and visibly observed around the tips of sharp-edge structures. Scale bar: 250 μm	17
2.5	(a) A portion of the microfluidics device. (b) Definition of a periodic cell forming the device.	22

3.1	(a) Schematic of the sharp-edge-based acoustofluidic mixing device. This device includes a PDMS microfluidic channel and a piezoelectric transducer. (b) Schematic showing the acoustic streaming phenomenon developed around the tip of an acoustically oscillated sharp-edge structure. (c) Schematic showing the detailed dimensions of the channel and sharp-edge structure.	30
3.2	Characterization of the flow pattern with/without acoustic streaming. (a) In the absence of acoustic waves, a laminar flow pattern was observed in a solution containing fluorescent beads. (b) In the presence of acoustic waves, acoustic streaming was developed in the liquid around the tips of sharp-edge structures.	31
3.3	Characterization of the mixing performance under different driving frequencies of the piezoelectric transducer for our sharp-edge-based acoustofluidic micromixer. (a) A laminar flow pattern was observed when the piezoelectric transducer was off. (b) 4.25 kHz: Incomplete mixing. (c) 4.50 kHz and (d) 4.75 kHz: Excellent mixing was achieved. (e) Plots of normalized fluorescent concentration across the width of channel.	33
3.4	Schematic of the microchannel with sidewall sharp-edge structures. The mixing index was characterized at five different positions (positions 1 – 5, indicated by the dashed white lines in the figure). . . .	34
3.5	Characterization of the mixing performance with different tip angles of sharp-edge structures. (a) 15°: Excellent mixing was quickly achieved after position 2. (b) 30°: Acceptable mixing was achieved after position 4. (c) 45°: Incomplete mixing. (d) 60°: A laminar flow pattern was observed even if the piezoelectric transducer was ON. (e) Plots of mixing indices at different positions along the microchannel with different tip angles of sharp-edge structures.	35
3.6	Schematic of the sharp-edge structure in the microfluidic channel.	36
3.7	Characterization of the mixing performance under different driving voltages. (a) 15 V _{PP} : Acceptable mixing was achieved after position 3. (b) 23 V _{PP} , (c) 31 V _{PP} , and (d) 39 V _{PP} : Acceptable mixing was quickly achieved after position 2. (e) Plots of mixing indices at different positions along the microchannel under different driving voltages.	37

3.8	Characterization of the mixing performance under different flow rates. (a) 1 $\mu\text{L}/\text{min}$: Excellent mixing due to low flow rate. (b) 2 $\mu\text{L}/\text{min}$: Acceptable mixing was achieved. (c) 3 $\mu\text{L}/\text{min}$ and (d) 4 $\mu\text{L}/\text{min}$: Acceptable mixing was achieved only after position 3. (e) Plots of mixing indices at different positions along the microchannel under different flow rates..	39
4.1	(a) Schematic of the acoustofluidic sputum liquefier. Experimental images showing the mixing of fluorescein and DI water when (b) PZT was off: a laminar flow pattern was observed; (c) PZT was on: excellent mixing of two fluids was achieved. (d) Photograph of our acoustofluidic sputum liquefier. (e) Drawing showing the detailed design of our acoustofluidic sputum liquefier. Simulated results showing the Lagrangian mean flow velocity when the fluid is (f) water and (g) a high viscosity fluid (such as sputum) with a viscosity ten times that of the water. Circular streamlines are observed in both cases indicating excellent mixing in both cases.	44
4.2	Drawing showing the detailed design of our acoustofluidic sputum liquefier.	45
4.3	Simulated results showing the Lagrangian mean flow velocity when the fluid is (a) water and (b) a high viscosity fluid (<i>e.g.</i> , sputum) with a viscosity ten times that of the water. Circular streamlines are observed in both cases, thereby indicating excellent mixing in both cases.	46
4.4	(d) Photograph of our acoustofluidic sputum liquefier. Experimental images showing the mixing of fluorescein and DI water when (b) PZT was off: a laminar flow pattern was observed; (c) PZT was on: excellent mixing of two fluids was achieved.	47
4.5	Characterization of the mixing performance at the beginning of the channel under different driving frequencies of the PZT. (a) A side-by-side laminar flow pattern was observed when the piezoelectric transducer was switched off. (b) 5.75 kHz: Incomplete mixing due to weaker acoustic streaming effect. (c) 5.50 kHz: Uniform mixing was observed. (d) 5.25 kHz: Excellent mixing was achieved, but not as complete as that obtained using 5.50 kHz. (e) Plots of normalized fluorescent intensity across the width of channel. The normalized intensity profiles were characterized along the dashed white lines in the figure. Scale bar: 500 μm	48

4.6	Characterization of the mixing performance at different regions under a total flow rate of 30 $\mu\text{L}/\text{min}$. (a) When the PZT was switched off: A side-by-side laminar flow pattern was first observed in the beginning of the long channel; partial, incomplete mixing due to diffusion was then observed at the middle and the end of the channel. (b) When the PZT was switched ON: Uniform, complete mixing was observed throughout the channel. (c) Plots of corresponding normalized fluorescent intensity across the width of channel at different regions. The normalized intensity profiles were characterized along the dashed white lines in the figure. Scale bar: 500 μm	50
4.7	Photograph showing the visual comparison of human sputum samples: (R) an un-liquefied raw sputum sample; (V) a sputum sample liquefied using a vortex mixer; (A) a sputum sample liquefied using our acoustofluidic device.	54
4.8	Cell viability of sputum samples liquefied using: (a) - (b) a standard sputum-liquefaction procedure; (c) - (d) our acoustofluidic sputum liquefier. (e) Statistical analysis showing the comparison of cell viability of two liquefaction procedures. Data represent an average of $n = 3$ to 4 independent experiments per group. In each independent experiment, over 500 cells were counted to assess cell viability. N.S. represents groups that are not statistically different ($p > 0.05$). Data are presented as group means \pm standard deviation (SD). Scale bar: 200 μm	55
4.9	Representative of optical images (100 \times) showing modified Wright–Giemsa staining results of cell samples obtained from sputum samples liquefied using (a) - (c) a vortex mixer or (d) - (f) our acoustofluidic sputum liquefier. Inflammatory cells, such as eosinophils (yellow) and neutrophils (red), are indicated by colored arrows. Scale bar: 50 μm	56
4.10	Quantification of cell content of induced sputum samples liquefied using a standard vortex mixer and our sputum liquefier (<i>i.e.</i> , acoustofluidic micromixer).	57
4.11	Fluorescence (CD45) vs. fluorescence (CD15) plot of the cell samples obtained from the sputum samples liquefied by (a) a standard sputum-liquefaction procedure and by (b) our acoustofluidic sputum liquefier. The percentage of co-population of eosinophils and neutrophils are 20.4% and 24.9% for (a) and (b), respectively.	58

5.1	(a) Schematic of the sharp-edge-based acoustofluidic chemical gradient generator. (b) Schematic of the sharp-edge structure within our device. (c) Optical image of the sharp-edge-based acoustofluidic chemical gradient generator.	63
5.2	Design of the sharp-edge-based acoustofluidic gradient generator. To demonstrate controllable spatial resolution of generated chemical gradients, the downstream region of the device is divided into three regions: region 1, region 2, and region 3.	64
5.3	Schematic showing our approach to characterize cell movement. 1, 2, and 3 mark, respectively, those cells which moved toward the center (high VEGF concentration), away from the center (low VEGF concentration), and barely moved, after 6 hours. Tracking the position of each cell, we determined the type of movement for each cell. By doing so, we were able to determine the number of cells for different types of movement.	69
5.4	(a) Fluorescent polystyrene beads seeded randomly inside the microchannel for visualization of flow profiles. (b) Experimentally observed streaming profile around the sharp-edge structure on acoustic actuation visualized via trajectories of 1.9 μm diameter fluorescent beads. (c) Numerically simulated trajectories of 80 beads seeded uniformly inside the channel showing good qualitative agreement with the experimental results in (b). (d) Flow profile around sharp-edge structures due to a background laminar flow in the absence of acoustic actuation. (e) Experimentally observed trajectories of 1.9 μm diameter fluorescent beads. These resulted from the combination of acoustically generated streaming and the background laminar flow. (f) Numerically simulated trajectories of 80 beads seeded uniformly inside the channel about the structures shown in (e). Scale bar: 500 μm	71
5.5	Fluorescent images of generated FITC-dextran gradients at different regions (from left to right: sharp-edge-structure region, region 1, region 2, and region 3) when (a) the piezoelectric transducer is inactive, and the piezoelectric transducer is on at (b) 10 V_{PP} and (c) 15 V_{PP} . The plots show the corresponding gradient profiles under different voltages at three regions downstream the channel: (d) region 1: 1500 μm wide, (e) region 2: 1000 μm wide, and (f) region 3: 700 μm wide. The results show that spatially controlled gradients may be generated by adjusting the input voltage of the piezoelectric transducer and the channel width downstream the channel.	73

5.6	(a) Schematic showing the alternative design (<i>i.e.</i> , to differently arrange sharp-edge structures inside the channel) of our sharp-edge-based acoustofluidic gradient generator to generate different gradient profiles. (b) Plot showing the corresponding gradient profiles at region of interest (dashed line) under different input voltages of the PZT. The results prove that by differently arranging the sharp-edge structures, various gradient profiles could be generated.	74
5.7	Fluorescent images of mixing behavior of FITC-dextran and DI water at the sharp-edge-structure region by varying (a) the total flow rates of the fluids inside the channel (the flow ratio remained constant), and (b) the flow rate ratio of the two fluids (the total flow rate remained constant). The plots show the corresponding gradient profiles at region 3 downstream the channel by changing (c) the total flow rates of the fluids inside the channel (the flow ratio remains constant, <i>i.e.</i> , $R_{FLOW} = 5$), (d) the flow rate ratio of the two fluids (the total flow rate remains constant), and (e) the flow ratio of the two fluids (the total flow rate is varied). These results demonstrate that by adjusting the total flow rate and the flow rate ratio, various gradient profiles may be generated using our acoustofluidic device.	75
5.8	Fluorescence images of mixing behavior of FITC-dextran and DI water at sharp-edge-structure region under different working voltages when the total flow rates of the fluids inside the channel is (a) $3 \mu\text{L}/\text{min}$ and (b) $6 \mu\text{L}/\text{min}$. The flow rate ratio remains constant, <i>i.e.</i> , $R_{FLOW} = 5$. These results clearly reveal that increasing the total flow rate inside the channel would significantly suppress the acoustic streaming and therefore, leads to different mixing behavior. On the other hand, however, various gradient profiles can be established by adjusting the total flow rates and the driving voltage. Scale bar: $500 \mu\text{m}$	76
5.9	(a) Fluorescent images showing a complete cycle of gradient generation at an ON/OFF frequency of 0.25 Hz ($T = 4 \text{ seconds}$). The plots show the corresponding fluorescence intensity profiles at regions of interest (ROI) in (a), when the gradient generator was operated at (b) an ON/OFF frequency of 0.25 Hz , (c) by sweeping the working frequency of the piezoelectric transducer from 13 kHz to 14 kHz within 4 seconds , and (d) within 8 seconds . The results demonstrate the spatiotemporal control of the chemical gradient generation using our sharp-edge-based acoustofluidic device.	77

5.10	HMVEC-d chemotaxis in the cell culture chamber. (a, b) Representative phase contrast image of cell positions at time = 0, 6 hours during chemotaxis. (c, d) Representative phase contrast images of cell positions at time = 0, 6 hours when only pure medium was present. The arrow points toward lower VEGF concentrations. (e) The percentage of cell movement in the cell culture chamber under various VEGF concentration conditions. Data represent averages of $n = 3$ independent experiments \pm standard deviation ($*p < 0.05$, $**p < 0.01$). Scale bar: 200 μm	78
5.11	(a) Representative bright field (BF) images showing the cell morphology at sharp-edge-structure regions and cell migration regions. Corresponding fluorescent images showing the cell viability after 6 hours (b) in the absence of an acoustic field (control group) and (c) in the presence of an acoustic field (experimental group). Scale bar: 200 μm	80
5.12	Representative bright field images taken at different regions in the channel showing the HMVEC-d cells morphology after 16 hours of the presence of acoustic field. The cells still appeared viable and active, demonstrating the biocompatibility of our acoustofluidic gradient generator for biological studies where long-term cell culture is needed. Scale bar: 200 μm	81
6.1	(a) Schematic of the sharp-edge-based acoustofluidic micropump. This device includes a PDMS microfluidic channel and a piezoelectric transducer. (b) Schematic showing the acoustic streaming phenomenon around the tip of a tilted oscillating sharp-edge structure. (c) Schematic showing the design of the channel and sharp-edge structure.	86
6.2	(a) Characterization of the acoustic streaming patterns developed around the tips of the 30° tilted sharp-edge structures. (b) Simulated results showing the streaming velocity in our pump in the presence of an acoustic field: a net flow of fluid from left to right is generated.	88
6.3	Experimental images showing the pumping behavior by indicating the movement of polystyrene beads at different time frames: a) $t_0 = 0$ sec, (b) $t_1 = 1$ sec, (c) $t_2 = 2$ sec, and (d) $t_3 = 3$ sec (red, yellow, and blue circles indicate three representative groups of beads). . . .	89

6.4	Experimental results illustrating the controllability and tunability of our sharp-edge-based acoustofluidic micropump. (a) Comparison of generated pumping flow rates with various tilting angles of sharp-edge structure as a function of the voltages applied to the PZT. The 30° tilted sharp-edge structures could generate a flow rate as high as 8 $\mu\text{L}/\text{min}$ under 50 V_{PP} . (b) Characterization of flow rate profiles by alternately switching the PZT on and off with different burst frequencies: burst frequency of 2 Hz (black) and burst frequency of 0.5 Hz (red).	91
-----	--	----

Acknowledgments

Firstly, I would like to express my sincere gratitude to my advisor, Prof. Tony Jun Huang, who has been there to provide unconditionally his constant supervision and support, trust and tolerance. About five years ago when I was very desperate, if it was not him, I would have given up on continuing my PhD study. Thanks to him, I had an opportunity to transfer from University of Michigan to Penn State, continuing my PhD study. After all these years, I have learned a lot from him — the way he handle people and things, the great enthusiasm he has about research, and even his life style — these altogether, have helped prepare me to strive for the best.

My sincere thankfulness also goes to my dissertation committee members: Prof. Bernhard R. Tittmann, Prof. Francesco Costanzo, and Prof. Corina Drapaca, all from Penn State Engineering Science and Mechanics, and Prof. Siyang Zheng from Penn State Biomedical Engineering. They have helped me with my thesis work in many different ways and their valuable suggestions are gratefully appreciated. I would also like to take this opportunity to acknowledge Prof. Judith Todd, the department head of Engineering Science and Mechanics, and her wonderful administrative staffs for their support and prompt assistance throughout my study at Penn State.

My dissertation work has been done primarily through collaborations with numerous graduate and undergraduate students, visiting scholars, and post-docs at The Acoustofluidics Reserach Group. I would also like to acknowledge all my former and current labmates for their academic as well as personall support and suggestions. Without their generous help and fuitful discussions, this dissertation would not be possible.

Lastly, I would like to thank my family for their love, caring, and constant encouragement that has made this dissertation possible. I would also like to thank my friends who have always been there for me.

Dedication

Dedicated to my beloved family and friends

Chapter 1

Motivation and Overview

Lab on a Chip (LOC) devices have attracted great interest and attention over the past decade due to their diverse applications in areas such as medicine, biology, chemistry, and physics, in which some of the laboratory functionalities can be shrunk and integrated onto a single microfluidic chip. Among the vital functionalities of microfluidic devices are fluid mixing and pumping. In this dissertation, a series of acoustofluidic technologies that exploit the acoustic streaming induced by acoustically oscillating sharp-edge structures are developed for the applications of fluid manipulation, specifically, fluid mixing and pumping. In this chapter, a brief introduction on the physical phenomena — **Acoustic Streaming** — is given along with a short literature review on the development of the microfluidic devices that are built based on acoustic streaming effect. Excellent, in-depth reviews on acoustic streaming are delivered by Lighthill [1], Riley [2], and Wiklund *et al.* [3], and the readers are encouraged to refer to these reviews for a broader scope.

1.1 Acoustic streaming

Acoustic streaming, referring to any flow induced by the force stemming from the presence of a gradient in the time-averaged acoustic momentum flux in a fluid [3], has been recently regarded as a powerful tool for a wide variety of microfluidic applications. Depending on the forms in which it may stem, acoustic streaming can be categorized into boundary-driven and bulk-driven acoustic streaming, as illustrated in Fig. 1.1 [4]. Both mechanisms originate from the attenuation of acoustic

energy flux, that in turn, induces momentum flux gradients and as such results in acoustic streaming. To be more specific, bulk-driven acoustic streaming, typically referred to as Eckart streaming, stems from the attenuation of acoustic energy in the bulk fluid, which decreases the amplitude of the acoustic pressure with the distance from the source of acoustic energy (typically an acoustic transducer) [5]; the attenuation of acoustic energy in turn drives a steady velocity in the propagation direction of the acoustic wave, as shown in Fig. 1.1(a). In boundary-driven acoustic streaming, which can be referred to as Schlichting streaming (*i.e.*, inner boundary layer streaming) [6] and Rayleigh streaming (*i.e.*, outer boundary layer streaming) [7], the acoustic energy dissipates primarily within the boundary layers at the solid walls because of the viscous stresses present in the boundary layer [5]. The attenuation within the boundary layer results in an acoustic velocity that transits from its bulk value to zero at the solid wall. As illustrated in Fig. 1.1(b) for the case of a standing wave parallel to the solid wall, the attenuation due to the viscous stresses induces a steady velocity that is parallel, close to the solid wall. The dominance of one mechanism over the other is determined based in large part on the size of the device that is studied. For example, devices that have comparatively smaller length scale of microchannel dimension in comparison to the acoustic wavelength and the attenuation length, will induce boundary-driven acoustic streaming upon acoustic actuation. It is important to note that in this work, the acoustic streaming generated in all of our devices are of boundary-driven acoustic streaming. As a result, only boundary-driven acoustic streaming is discussed and investigated in this dissertation.

1.2 Literature review

In this section, we give a brief review, specifically, on microfluidic devices that are built based mainly on boundary-driven acoustic streaming, and their applications.

1.2.1 Acoustic streaming based on oscillating bubbles

In the past decade, acoustically oscillating microbubble has been proved to induce acoustic streaming, also known as cavitation microstreaming, and has drawn much attention and interest due to its single-layer fabrication of device, ease of device

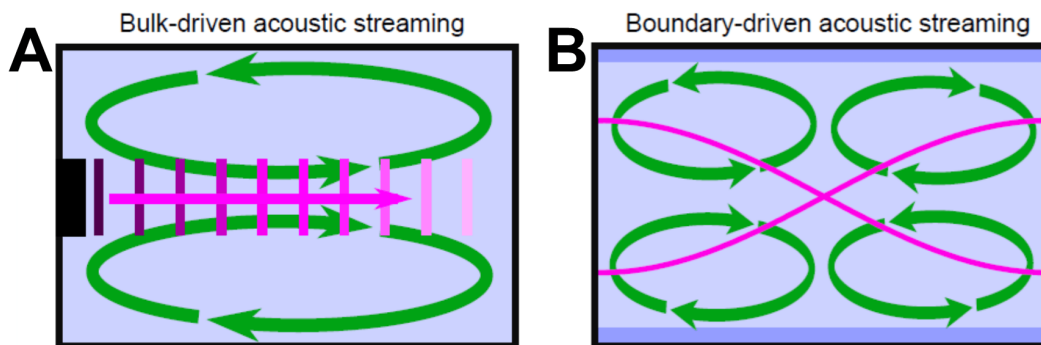


Figure 1.1. Schematic showing the category of acoustic streaming based on different generating mechanisms: (a) bulk-driven acoustic streaming, and (b) boundary-driven acoustic streaming. Green arrows: steady flow. Blue region: bulk of fluid. Pink lines: acoustic wave. Dark blue: boundary layers. This figure is adopted and reproduced from Ref. [4].

operation, and comparatively high streaming velocity. The acoustic streaming induced by oscillating microbubble can be viewed as the steady flow resulting from the viscous dissipation of acoustic energy in the boundary layer of the oscillating microbubble. The “soft” boundary layer of the microbubble, upon acoustic excitation, oscillates at a much higher amplitude than the oscillation of a solid boundary layer, thereby attenuating significantly the acoustic energy. This drastic loss of acoustic energy locally amplifies the first order velocity [8] and as a result, comparatively high-velocity streaming are induced near the surface of oscillating microbubble. Microbubbles of different sizes, when excited at or near their corresponding resonance frequencies, can induce acoustic streaming with a wide range of streaming velocity for various applications, including fluid mixing [9–12], pumping [10, 13–15], particle manipulation [16–19], cell manipulation [20, 21], micro-object manipulation [22–24], and cell lysis [25]. Among these applications, fluid mixing and pumping, the two most vital functions of microfluidic devices, have gained much attention and been proven as promising candidates to be integrated with other microfluidic components for the development of integrated LOC devices.

1.2.1.1 Fluid mixing based on oscillating microbubbles

Rapid mixing and homogenization of chemical/biological species at the microscale is of great importance for a wide variety of applications, including chemical kinetics studies and material synthesis. While microfluidic devices seem to be an excellent

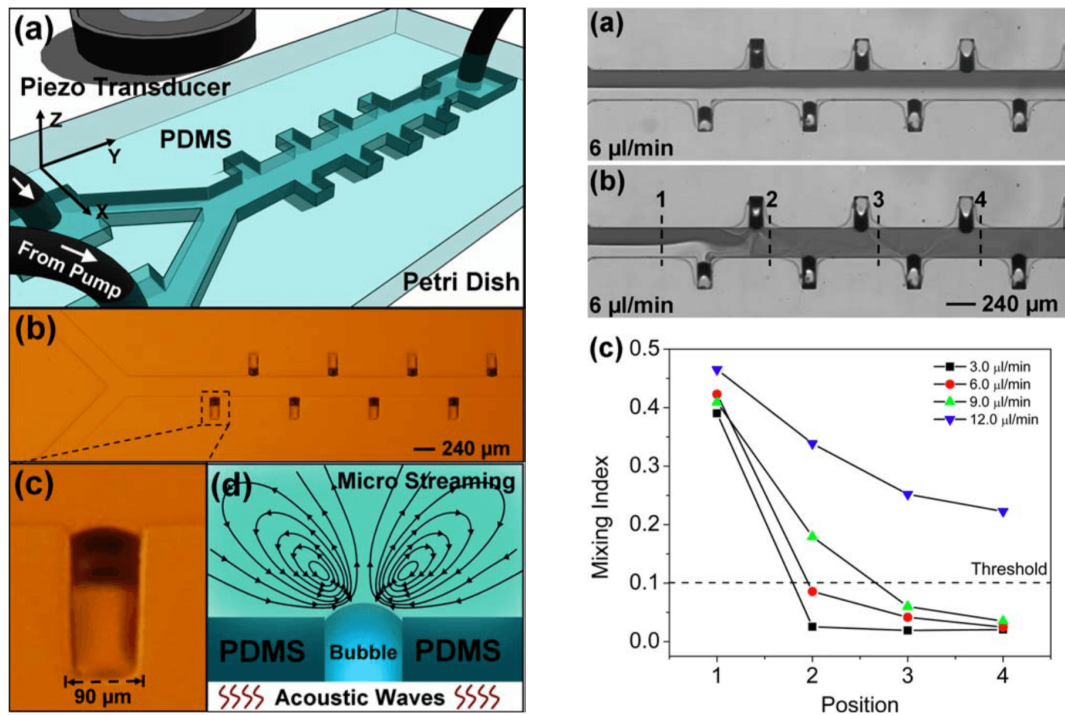


Figure 1.2. (Left) Schematics showing the experimental setup of the micromixer based on the oscillating microbubbles trapped in sidewall pre-defined cavities. (Right) Experimental images and characterization plot showing the mixing performance of two different liquids achieved by the bubble-based mixer. This figure is adopted and reproduced from Ref. [11].

platform for carrying out these studies due to their short reaction times, high throughput, and reduced reagent consumption, effectively mixing fluids at the microscale is not a trivial process. Due to inherently small channel dimensions, the flow of fluid in microfluidic devices is usually laminar; under laminar flow conditions, viscous forces dominate over inertial forces and fluids are not easily mixed. As shown in Fig. 1.2, one of the examples demonstrating fluid mixing was presented by Ahmed *et al.* [11], in which air microbubbles trapped in the pre-defined grooves, also known as horseshoe cavities, were acoustically oscillated to induce acoustic streaming to achieve fast and homogenized mixing of two side-by-side flowing fluids. A mixing time as short as 120 ms was achieved at a total flow rate of 12 $\mu\text{L}/\text{min}$ of the injected liquids, which corresponds to a flow velocity of ~ 5.4 mm/s. As another example, similar micromixer design using sidewall cavities to trap microbubbles was proposed by Tovar and Lee [10]. In their work, mixing of two different fluids was achieved at a flow rate of 0.25 $\mu\text{L}/\text{min}$ under a driving

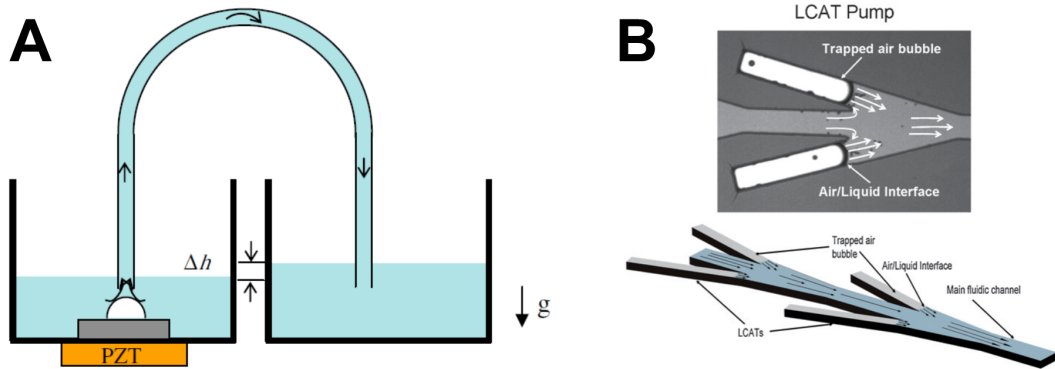


Figure 1.3. (a) Schematic showing the experimental configuration of micropump based on a single microbubble by Cho *et al.* [13]. (b) Schematic showing the working concept of the micropump based on multiple microbubbles trapped in later cavities inside a microfluidic channel by Tovar and Lee [10]. This figure is adopted and reproduced from Ref. [10, 13]

voltage of piezoelectric transducer of $35 V_{PP}$. Though this mixing performance was less promising, compared to the work conducted by Ahmed *et al.* [11], the micromixer presented still proved the acoustic streaming induced by oscillating microbubbles to be extremely useful for fluid mixing.

1.2.1.2 Fluid pumping based on oscillating microbubbles

Fluid pumping is one of the most vital functions needed to develop integrated LOC devices. Conventionally, the pumping of LOC devices relies on the external pumps, like syringe pumps, which remains bulky and challenging to integrate with existing microfluidic components, despite the superior stability of syringe pumps at low flow rates. Significant efforts have been made toward developing truly on-chip pumping using various pumping mechanisms. Exploiting the extremely high streaming velocity of the acoustic streaming induced by oscillating microbubble, Cho *et al.* [13] achieved a pumping flow rate of $11.4 \mu\text{L}/\text{min}$ under a pressure load of 253 Pa by acoustically exciting a microbubble of $400 \mu\text{m}$ in diameter. Though they have successfully achieved fluid pumping by implementing oscillating microbubble, their experimental setup, as provided in Fig. 1.3(a), is very unlikely to be integrated with existing microfluidic components, and the pumping performance has yet to be improved. In addition to fluid mixing, Tovar and Lee [10] also demonstrated fluid pumping based on the acoustic streaming induced by oscillating

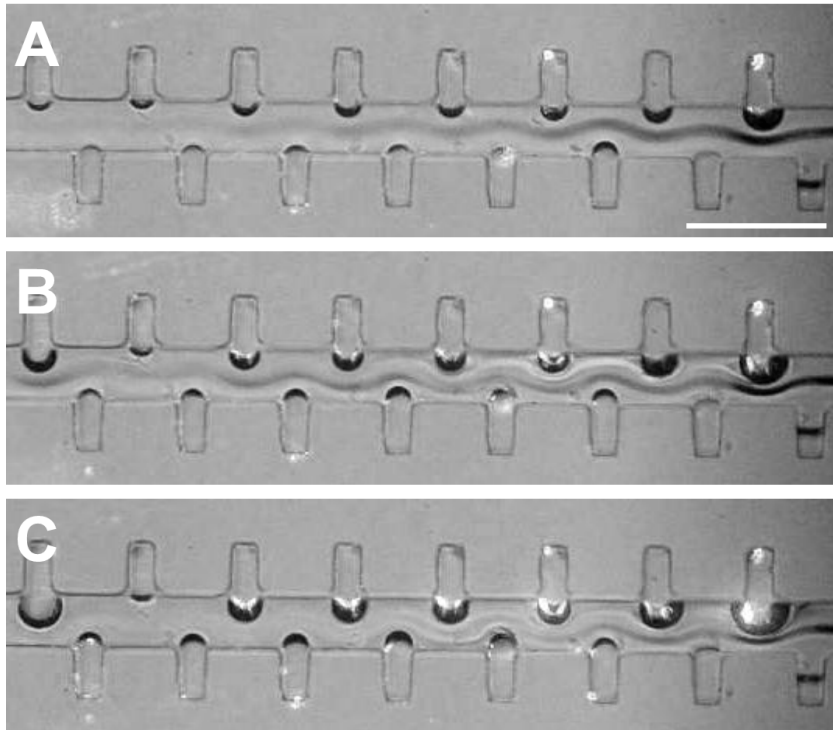


Figure 1.4. Experimental images showing the expanding up of microbubbles over time during operation: (a) $t_0 = 0$ sec, (b) $t_1 = 3$ sec, and (c) $t_2 = 6$ sec. This would lead to the variation in the bubble size of each bubble and as a result, alter the driving frequency. Scale bar: $450 \mu\text{m}$.

microbubbles. Upon acoustic actuation, as shown in Fig. 1.3(b), microbubbles oscillated to generate acoustic streaming and thus produced a net force pointing toward the direction that the lateral air cavity was orientated; this net force was the main force driving the fluid pumping motion. A pumping flow rate of $250 \text{ nL}/\text{min}$ was achieved under a driving voltage of piezoelectric transducer of 40 V_{PP} . With further optimization on the channel geometry and tilting angle of later air cavity of their oscillating-bubble-based pumping device, the same group achieved fluid pumping under a pressure load of 350 Pa (under a driving voltage of 25 V_{PP}) [14].

Through the examples we reviewed in this section, microfluidic devices that implements the acoustic streaming induced by oscillating bubbles are believed to be extremely useful and of great importance, specifically for fluid mixing and pumping. There are, however, several potential problems associated with the intrinsic characteristics of oscillating-bubble-based devices that have to be addressed. First

of all, for example, it is required to form microbubbles in pre-designed cavities or generate freely-suspended bubbles in the microchannel, complicating the operation of bubble-based platforms, although numerous techniques have been reported for generating microbubbles. Secondly, the care needs to be taken during experiments since the formed microbubbles may shrink or expand over time under different flow situations as shown in Fig. 1.4 [10, 26]. This results in the discrepancy in operating frequencies of microbubbles. In addition, the discrepancy in operating frequencies would be caused because the size or curvature for each single bubble is not perfectly identical when we re-form or re-generate microbubbles every time. Although theoretical models that can estimate the natural frequency of bubbles with different shapes have been reported, one way to possibly compensate for the change in the size or curvature of bubbles during experiments is to experimentally adjust the excited frequency. Through our previous study [26], we found that the bubble-based platforms would generate heat and then raise the ambient temperature inside the microchannel, hindering it from biological study since cells or other biological samples might be killed/damaged by high ambient temperatures. All these potential issues greatly limit the biological application of bubble-based platforms. To address these issues, there is an urgent need to develop an alternative platform where it is still possible to generate larger acoustic streaming velocities similar to those generated by oscillating microbubbles, while circumventing the limitation of the microbubbles.

1.2.2 Acoustic streaming based on oscillating flow

As an alternative, recently, acoustic streaming induced by oscillating fluid flow around the solid surface of fixed micro-posts, protrusions and cavities, also known as “Hydrodynamic Tweezers”, has been proposed and intensively studied by Schwart’s group [29, 30] for localized fluid mixing [31] and cell/particle trapping [27, 28, 32]. Among the application of the acoustic streaming induced by oscillating flow is particle/cell trapping that has been well received by the microfluidic community. Figure 1.5(a) shows a typical microfluidic device proposed by Schwart *et al.* [27] for particle trapping. In the device, solid structures of different feature geometries, including posts, protrusions, and cavities, were constructed and two piezoelectric disks were attached underneath each of the two inlets. Upon alternatively activat-

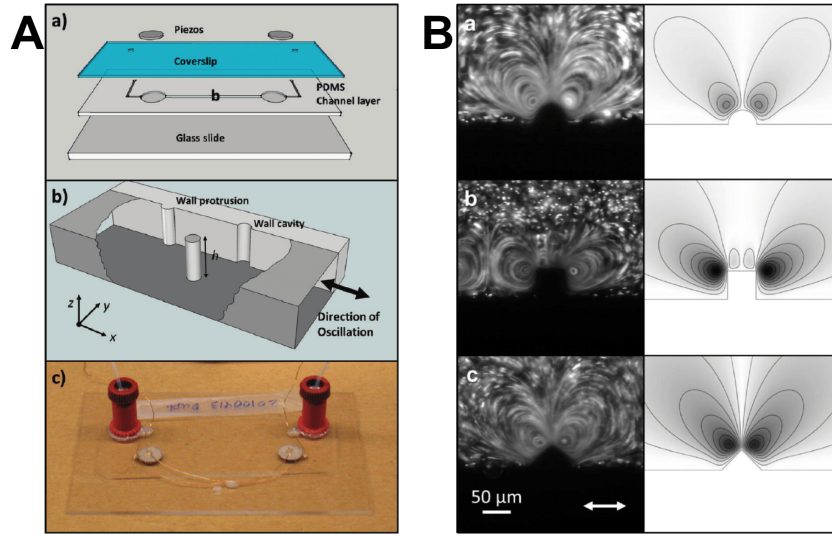


Figure 1.5. (a) Schematics showing the experimental setup and concept for the device that oscillates flow around solid structures to induce microeddies, *i.e.*, acoustic streaming. (b) Experimental and numerical images showing the streaming patterns when an oscillating flow is introduced around various geometries of solid structure in the channel. This figure is adopted and reproduced from Ref. [27].

ing the two piezoelectric disks, fluid displacement, namely, an oscillating flow field, was generated, which in turn, generates symmetric acoustic streaming patterns adjacent to those solid structures, as shown in Fig. 1.5(b). Extending the capability of this device, the same group further constructed multiple solid structures inside microfluidic channels, also named as "hydrodynamic tweezers arrays" [28]. With the advancement, symmetric as well as uniform acoustic streaming pattern were generated adjacent to each of the solid structures inside the channel, as can be seen in Fig. 1.6(a), and with these generated acoustic streaming pattern, a high-throughput particle/cell trapping might be enabled, as can be seen in Fig. 1.6(b). Schwartz *et al.* presented an easier way than trapping micorbubbles to induce acoustic streaming, because the acoustic streaming produces a non-contact force to trap micro-objects without the need of trapping microbubbles. It is important, however, to indicate that in this technique, the flow was stationary in the absence of acoustic field, meaning that the flow was not flowing and as a result, the application might be confined to the trapping of micro-objects. For most of the microfluidic applications (*e.g.*, fluid mixing and pumping), in fact, they are carried out under a continuous flow regime, instead of a stationary flow regime.

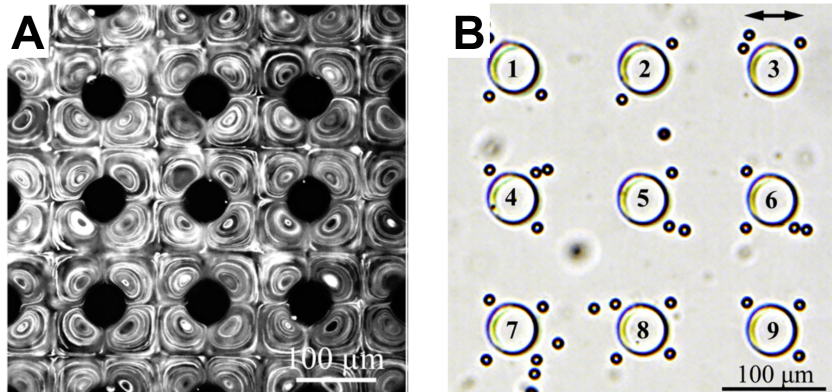


Figure 1.6. (a) Fluorescent image showing acoustic streaming patterns under an oscillating flow when multiple solid structures are constructed in the channel. (b) Experimental image showing the trapping of $10\ \mu\text{m}$ polystyrene particles. This figure is adopted and reproduced from Ref. [28].

While local mixing of two different liquids has been demonstrated by the same group [31] using this mechanism of oscillating flow, this mechanism, still, is not applicable for fluid mixing in a continuous flow regime. Moreover, the capability of this mechanism to induce acoustic streaming for fluid pumping is yet unproven; however, that is extremely challenging because of the oscillating flow field. Nevertheless, compared to the oscillating-bubble-based microfluidic devices (1.2.1, the oscillating-flow-based microfluidic devices are advantageous in terms of stability and controllability when conducting experiments.

1.3 Motivation

As pointed out in Section 1.2.1 and 1.2.2, we learn that both of the mechanisms to induce acoustic streaming possess their own intrinsic characteristics and limitations. The challenge is to achieve various microfluidic applications, still, by using acoustic streaming, while circumventing the disadvantages and preserving the uniqueness and advantages of these two mechanisms. The oscillation of microbubble, in fact, can be also seen as the oscillation of “softer” microstructure upon acoustic actuation. Under a steady acoustic actuation, the only difference between the oscillation of a soft structure (*e.g.*, the membrane of microbubble) and a hard structure (*e.g.*, PDMS microstructure) is the amplitude of oscillation; in

other words, the oscillation of microbubble may result in stronger acoustic streaming, whereas, the oscillation of hard, solid structure may result in weaker acoustic streaming. Besides, the oscillation of solid structure in a continuous flow regime under acoustic actuation, conceptually, is equivalent to the oscillation of microbubble in a continuous flow regime. Thus, building upon the two mechanisms — oscillating microbubble/flow — to induce acoustic streaming, in this dissertation we propose to develop microfluidic devices that utilize the acoustic streaming induced by oscillating so-called “sharp-edge” solid structures. Not only can the disadvantages from oscillating microbubbles and oscillating flow be overcome, but the uniqueness and advantages of acoustic streaming can be preserved. To be more specific, the advantage of using oscillating sharp-edge structures to induce acoustic streaming, when compared to oscillating microbubbles, lies in stability, reliability, bio-compatibility and controllability, and when compared to oscillating flow, it is versatile because oscillating sharp-edge structures can be operated under a continuous flow regime, thereby enabling various microfluidic applications instead of the trapping of micro-objects only.

1.4 Dissertation outline

This dissertation describes our research efforts on developing microfluidic devices that implement the acoustic streaming induced by oscillating sharp-edge structures for various microfluidic applications, particularly for fluid mixing and pumping. Chapter 2 presents preliminary results and numerics on the generation of acoustic streaming by oscillating sharp-edge structures. Chapter 3 – 6 are expanded versions of published, submitted or soon to be submitted technical research manuscripts. Each chapter starts with a short introduction/motivation section to justify the importance and objective of that particular chapter, followed by a brief literature review to further distinguish the novelty of our work when necessary. Chapter 7 outlines the summary of this dissertation and discusses the prospective directions for future research.

Chapter 2 — Acoustic streaming by oscillating sharp-edge structures

This chapter provides an introduction to the concept of generating acoustic streaming using oscillating sharp-edge structures. We introduce our typical experimental

setup, device configuration, as well as typical design parameter of sharp-edge structure for the generation of acoustic streaming. We conduct preliminary experiments to verify whether or not, acoustically oscillating sharp-edge structures can result in acoustic streaming. Based on these preliminary results, we are able to engineer acoustic streaming patterns by modifying sharp-edge structure for applications that are presented in Chapter 3 – 6. Furthermore, in this chapter we also provide a numeric model for the simulation of acoustic streaming induced by oscillating sharp-edge structures. By using the numerical model, we are able to match the experimental results with numerical simulation, enabling us to predict the performance of device for different applications before we fabricate devices.

Chapter 3 — Sharp-edge-based acoustofluidic micromixer

In Chapter 3, an acoustofluidic microfluidic mixer is developed where rapid and homogeneous mixing of fluid is achieved *via* the acoustic streaming induced by oscillating sharp-edge structures. We characterize the mixing performance of our sharp-edge-based acoustofluidic micromixer by evaluating the mixing index at different locations inside the channel along the direction of channel length. The mixing performance is compared among different driving frequency of piezoelectric transducer, different tip angles of sharp-edge structure, different driving voltages of piezoelectric transducer, as well as different flow-rate conditions.

Chapter 4 — Sharp-edge-based acoustofluidic sputum liquefier

In this chapter, extending the capability of our sharp-edge-based acoustofluidic micromixer, we mix highly viscous fluid, *i.e.*, human sputum sample, with another fluid, *i.e.*, sputolysin, which has a viscosity close to that of water, by using a modified sharp-edge-based acoustofluidic micromixer, also named as sputum liquefier. The sputum sample liquefied by our acoustofluidic sputum liquefier is characterized and compared with that liquefied by a standard vortex mixer through analysis including visual comparison in the composition, cell morphology, cell content, cell viability, and flow cytometry.

Chapter 5 — Sharp-edge-based acoustofluidic chemical gradient generator

To advance our sharp-edge-based acoustofluidic micromixer, in Chapter 5 we develop an sharp-edge-based acoustofluidic chemical gradient generator by engineering the acoustic streaming patterns generated inside the microfluidic channel. We demonstrate that by engineering the acoustic streaming patterns, concentration gradients of chemical of interest are generated because of the serial mixing of different solutions. The gradient profiles are characterized under different flow-rate conditions and different driving driving voltages of piezoelectric transducer. By alternating the piezoelectric transducer with different bursting frequencies, our acoustofluidic gradient generator generate spatiotemporally controllable gradient profiles. We also verify the biocompatibility of our gradient generator by conducting cell-migration experiments under concentration gradients generated using our device, as well as cell-viability tests.

Chapter 6 — Sharp-edge-based acoustofluidic micropump

In Chapter 6, we devote to developing a microfluidic pump using the acoustic streaming induced by oscillating sharp-edge structures. To do so, we engineer the geometry of sharp-edge structure , specifically, tilting the sharp-edge structure, which in turn, alters the acoustic streaming patterns generated inside the channel. The effect of the sharp-edge structures which are differently tilted on the pumping performance are investigated and characterized. By controlling the driving signals of piezoelectric transducer, including the driving frequency and voltage, the pumping performance can be controlled, which leads to versatile flow rate profiles.

Chapter 7 — Conclusions and Outlooks

We conclude this dissertation by summarizing the microfluidic applications that we have achieved utilizing the acoustic streaming induced by oscillating sharp-edge structures. Furthermore, we also give prospects for future directions of fundamental studies (*i.e.*, physics and mechanisms) and biological applications (*e.g.*, cell manipulation, lysis and enrichment) to advance the sharp-edge-based microfluidic platforms.

Acoustic streaming by oscillating sharp-edge structures

2.1 Generation of acoustic streaming by oscillating sharp-edge structures

In this work we will utilize the acoustic streaming effects induced by the oscillation of sharp-edge structures to realize various microfluidic applications for, particularly, fluid mixing and pumping. In this section, we present preliminary experimental results to show the acoustic streaming patterns induced by acoustically oscillating sharp-edge structures inside polydimethylsiloxane (PDMS)-based microfluidic channels.

Figure 2.1(a) shows a typical setup of a sharp-edge-based microfluidic device, which is consisted of a single-layer PDMS channel with sharp-edge structures protruding on its sidewall and is bonded onto a thin glass slide. A circular piezoelectric transducer is then attached adjacent to the PDMS channel using a thin layer of epoxy/glue. Upon the actuation of the piezoelectric transducer, the sharp-edge structures are acoustically oscillated to generate a pair of counter-rotating vortices (double-ring recirculating flows) in the fluid around the tip of each sharp-edge structure, as shown in Fig. 2.1(b). The typical design for the device and sharp-edge structure are shown in Fig. 2.1(c): the channel is $600\ \mu\text{m}$ in width and $50\ \mu\text{m}$ in length, while the sharp-edge structure is $250\ \mu\text{m}$ in height and 15° in tip angle. Depending upon various applications of interest, the dimensions of the channel

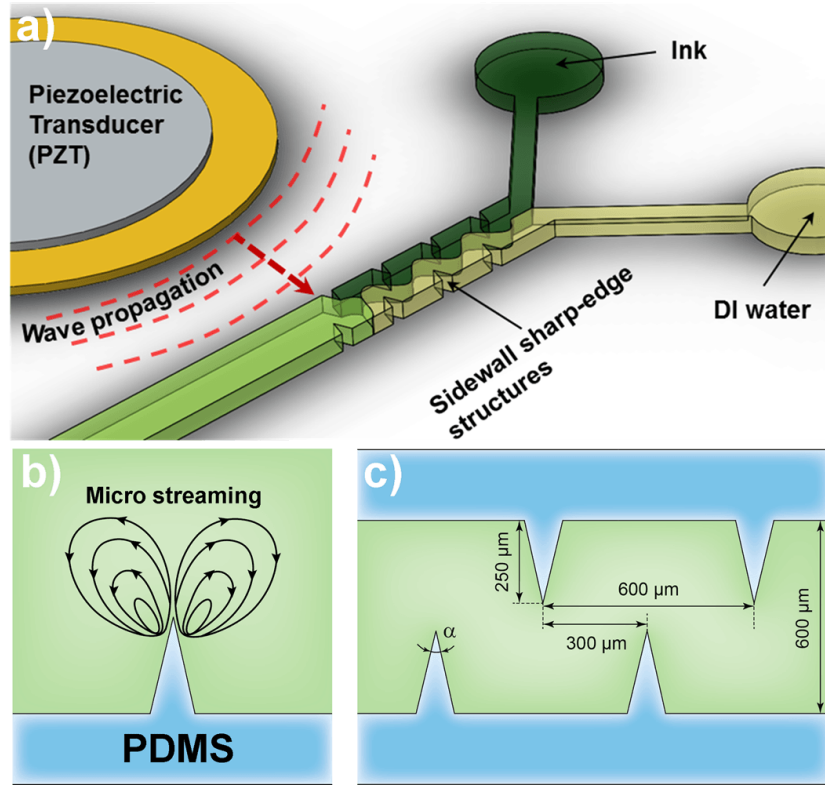


Figure 2.1. (a) Schematic of the device showing a micro-fluidics channel with sharp-edge structures on its sidewalls. The channel walls are subjected to a time-harmonic excitation produced by a piezoelectric transducer placed on one side of the channel. (b) Typical micro streaming patterns produced in the fluid occupying the channel as a response to piezoelectric excitation. (c) Typical geometric dimensions of the corrugated channel.

and sharp-edge structure can be modified accordingly.

Note that the location of the piezoelectric transducer should not have significant effects, since the size of the piezoelectric transducer is much larger than that of the PDMS channel. To ensure the consistency and reproducibility of experimental results when conducting experiments, after peeling off from silicon molds, the PDMS channels are always cut and trimmed by aligning the four markers as shown in Fig. 2.2, which allows us fabricate devices with exactly identical size, and then the piezoelectric transducer is attached to PDMS wall as close as possible. In other words, by doing so we are able to minimize device-to-device variations.

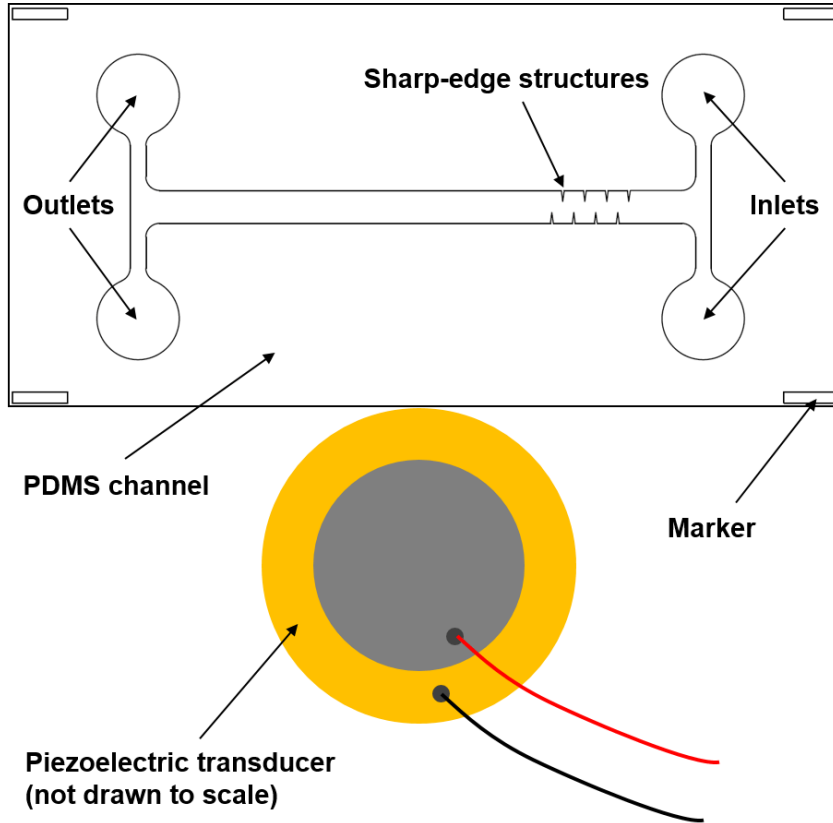


Figure 2.2. Arrangement of the PDMS channel and piezoelectric transducer.

2.1.1 Acoustic streaming effect under no background flow

To visualize acoustic streaming patterns generated inside the channel, DI water mixed with dragon-green fluorescent beads of $1.9 \mu\text{m}$ in diameter was injected into the channel. Figure 2.3 shows when there was no background flow, the flow pattern of fluorescent beads inside the channel under different driving voltages of the piezoelectric transducer. When the piezoelectric transducer was inactivated (*i.e.*, switched OFF), the fluorescent beads remained stationary inside the channel, as shown in Fig. 2.3(a). Once the piezoelectric transducer was activated (*i.e.*, switched ON) under a driving voltage of $10 V_{PP}$, a pair of symmetric counter-rotating vortices, namely, acoustic streaming effect, was developed around the tip of each sharp-edge structure, as shown in Fig. 2.3(b), and as the driving voltage was further increased from 10 to $50 V_{PP}$, the strength of acoustic streaming effect was enhanced accordingly, and the symmetric vortices spanned gradually the entire channel (Fig. 2.3(c)-(d)). These results suggest that the strength of acoustic

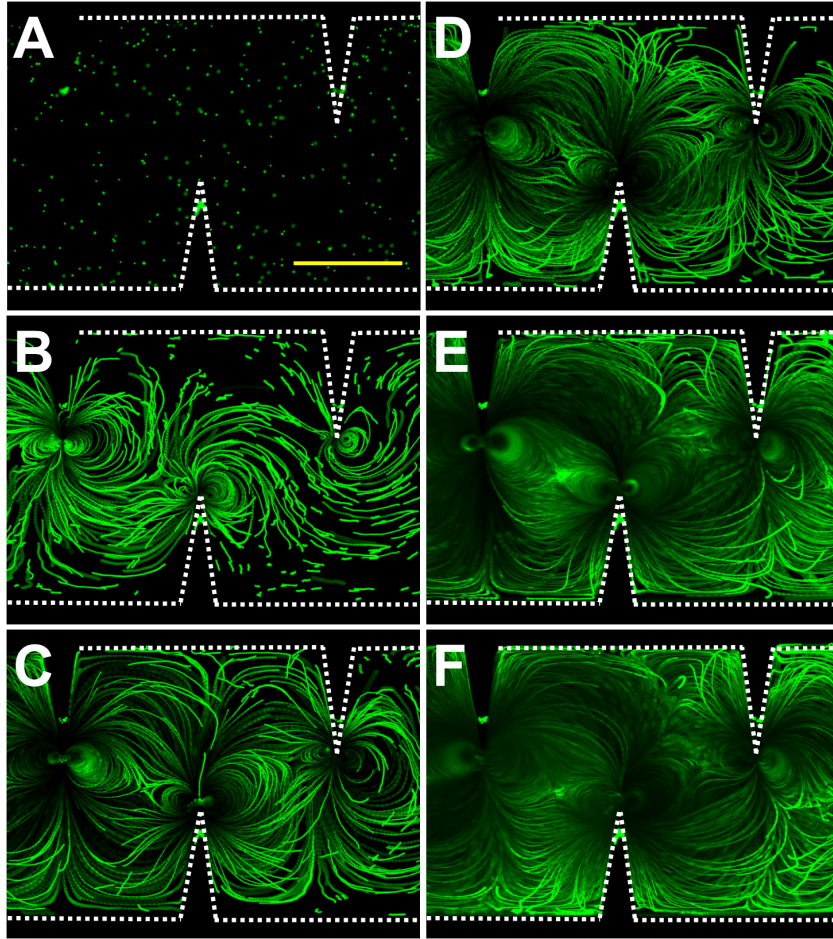


Figure 2.3. Fluorescent images showing flow patterns visualized using dragon-green fluorescent beads seeded randomly inside the channel under no background flow at different voltages: (a) $0 V_{PP}$, *i.e.*, switched-OFF, (b) $10 V_{PP}$, (c) $20 V_{PP}$, (d) $30 V_{PP}$, (e) $40 V_{PP}$, and (f) $50 V_{PP}$. When the piezoelectric transducer was inactivated (*i.e.*, switched OFF), the fluorescent beads remained stationary inside the channel. Once the piezoelectric transducer was activated under a driving voltage of $10 V_{PP}$, acoustic streaming effect was developed around the tip of each sharp-edge structure and as the driving voltage was further increased, the strength of acoustic streaming effect was enhanced accordingly. Scale bar: $250 \mu\text{m}$.

streaming effect can be adjusted/controlled by controlling the driving voltage of the piezoelectric transducer. In other words, we can control over the strength of acoustic streaming effect for different applications.

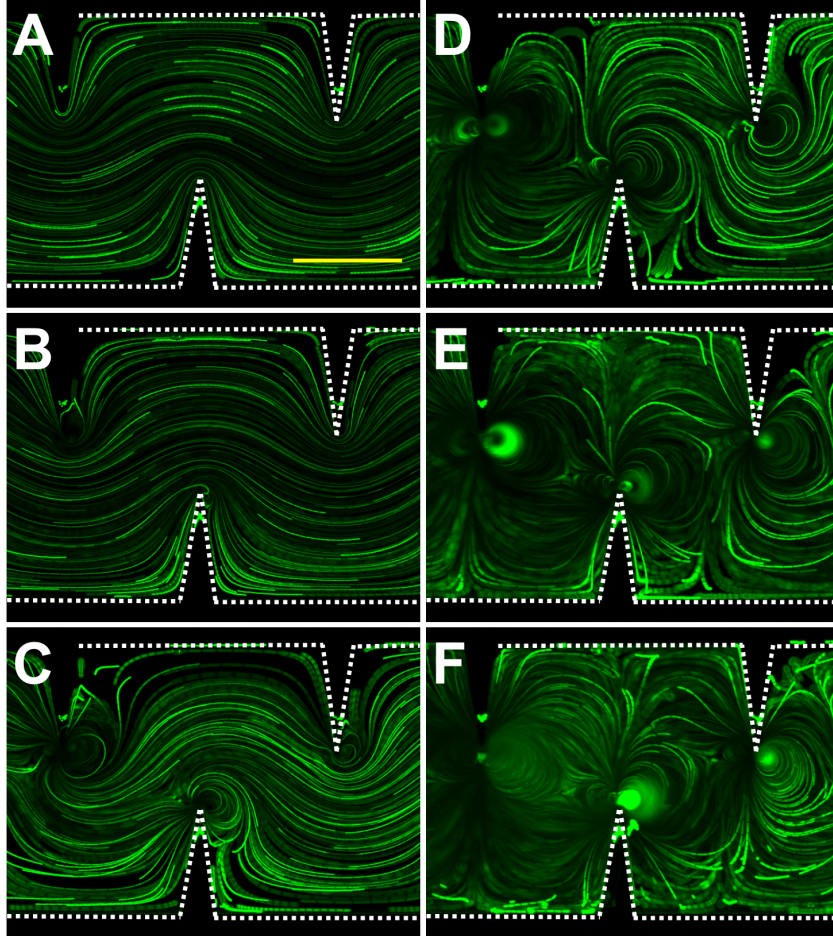


Figure 2.4. Fluorescent images showing flow patterns visualized using dragon-green fluorescent beads seeded randomly inside the channel under a background flow at different voltages: (a) $0 V_{PP}$, *i.e.*, switched-OFF, (b) $10 V_{PP}$, (c) $20 V_{PP}$, (d) $30 V_{PP}$, (e) $40 V_{PP}$, and (f) $50 V_{PP}$. Upon the introduction of a background flow (from left to right), a laminar flow pattern was observed when the piezoelectric transducer was switched-OFF. Though the piezoelectric transducer was switched-ON with a driving voltage of $10 V_{PP}$, the acoustic streaming effect could be hardly developed around the tip of each sharp-edge structure. Once the voltage was further increased from $10 V_{PP}$ to $50 V_{PP}$, the asymmetric acoustic streaming patterns were generated and visibly observed around the tips of sharp-edge structures. Scale bar: $250 \mu\text{m}$.

2.1.2 Acoustic streaming effect under a background flow

As presented in Section 2.1.1, the acoustic streaming effect was developed to be a pair of symmetric counter-rotating vortices around the tip of sharp-edge structure. To investigate the effect of background flow on the generation of acoustic streaming effect in the presence of acoustic field, we also conducted experiments where a

background flow was introduced into the channel at a flow rate of $2 \mu\text{L}/\text{min}$, which corresponds to a flow velocity of $2.2 \text{ mm}/\text{sec}$. Upon the introduction of a background flow (from left to right), a laminar flow pattern, as shown in Fig. 2.4(a), was first observed when the piezoelectric transducer was switched-OFF. Though the piezoelectric transducer was switched-ON with a driving voltage of 10 V_{PP} , the acoustic streaming effect could be hardly developed around the tip of each sharp-edge structure, as shown in Fig. 2.4(b). Once the voltage was gradually increased with a 10 V_{PP} increment (*i.e.*, from 20 to 50 V_{PP}), the acoustic streaming effect could be induced and visibly observed (Fig. 2.4); however, instead of symmetric counter-rotating vortices, asymmetric counter-rotating vortices were generated around the tip of sharp-edge structure. More specifically, the left-side counter-clockwise rotating vortice, which is against the direction of the background flow, was weakened by the background flow. That is to say, the background flow significantly suppressed the ability to oscillate sharp-edge structures to induce acoustic streaming effect, while raising the driving voltage indeed strengthened the ability to induce acoustic streaming effect. Nevertheless, the results also suggest that we can manipulate acoustic streaming patterns by controlling the velocity of background flow, in conjunction with the control over the driving voltage of piezoelectric transducer.

2.2 Numerics of acoustic streaming effect induced by oscillating sharp-edge structure

This dissertation work emphasizes on the experimental generation of acoustic streaming effect utilizing acoustically oscillating sharp-edge structures and its microfluidic applications. Nevertheless, we also develop a numerical model to simulate the generation of acoustic streaming to predict as well as optimize the sharp-edge-based device. In this section, we present the governing equations and boundary conditions that are adopted to develop the numeric model.

2.2.1 Governing equations

The mass and momentum balance laws that govern the motion of a linear viscous compressible fluid are expressed as [33, 34]

$$\frac{\partial \rho}{\partial t} + \nabla \cdot (\rho \mathbf{v}) = 0, \quad (2.1)$$

and

$$\rho \frac{\partial \mathbf{v}}{\partial t} + \rho (\mathbf{v} \cdot \nabla) \mathbf{v} = -\nabla p + \mu \nabla^2 \mathbf{v} + (\mu_b + \frac{1}{3}\mu) \nabla (\nabla \cdot \mathbf{v}), \quad (2.2)$$

where ρ , \mathbf{v} , p , μ , and μ_b are, respectively, the mass density, fluid velocity, fluid pressure, shear viscosity, and bulk viscosity. To further describe the fluid motion, we need an equation of state to link the density (ρ) and pressure (p), and a linear relation between the density and pressure can be assumed by [35]

$$p = c_0^2 \rho, \quad (2.3)$$

where c_0 is the speed of sound in the fluid at rest. These equations, with suitable boundary conditions, can be used to study the motion of the fluid inside sharp-edge based devices. The nonlinear system of equations presented above, however, is numerically challenging to solve *via* a direct numerical simulation due to the widely separated time scales (characteristic oscillation periods vs. characteristic times dictated by the streaming speed) and in some cases, widely separated length scales (characteristic length of the device vs. wavelength) [36]. SAW devices, for example, operate typically at the frequency range of 1 – 100 MHz, while the streaming fields are characterized by time scales of the order of tenth of seconds to several minutes. Because of viscous dissipation, the response of the fluid to a harmonic forcing, however, is not harmonic in general. The fluid response can be understood to be comprised of two components: (*i*) a periodic component that has a period equal to the forcing period, and (*ii*) a mean component that can be viewed as being steady. The second component is generally referred to as the *streaming motion* [37]. Following the model we recently proposed [38], we employ Nyborg’s perturbation approach [5] where the fluid velocity, density, and pressure are assumed to have the following form

$$\mathbf{v} = \mathbf{v}_0 + \varepsilon \tilde{\mathbf{v}}_1 + \varepsilon^2 \tilde{\mathbf{v}}_2 + O(\varepsilon^3) + \dots, \quad (2.4a)$$

$$p = p_0 + \varepsilon \tilde{p}_1 + \varepsilon^2 \tilde{p}_2 + O(\varepsilon^3) + \dots, \quad (2.4b)$$

$$\rho = \rho_0 + \varepsilon \tilde{\rho}_1 + \varepsilon^2 \tilde{\rho}_2 + O(\varepsilon^3) + \dots, \quad (2.4c)$$

where ε is a non-dimensional small parameter. Following Köster [39], ε is defined as the ratio between the amplitude of the displacement of the boundary in contact with the piezo-electrically driven substrate (*i.e.*, the amplitude of the boundary excitation) and a characteristic length, usually taken to be as the length of the device. The zeroth order velocity field \mathbf{v}_0 is considered equal to zero, indicating the absence of an underlying net flow along the microchannel. Letting

$$\begin{aligned} \mathbf{v}_1 &= \varepsilon \tilde{\mathbf{v}}_1, & p_1 &= \varepsilon \tilde{p}_1, & \rho_1 &= \varepsilon \tilde{\rho}_1, \\ \mathbf{v}_2 &= \varepsilon^2 \tilde{\mathbf{v}}_2, & p_2 &= \varepsilon^2 \tilde{p}_2, & \rho_2 &= \varepsilon^2 \tilde{\rho}_2, \end{aligned} \quad (2.5)$$

substituting Eqs. (2.4) into Eqs. (2.1) and (2.2), and setting the sum of all the terms of order one in ε to zero, we can obtain the first-order problem as the following

$$\frac{\partial \rho_1}{\partial t} + \rho_0 (\nabla \cdot \mathbf{v}_1) = 0, \quad (2.6)$$

$$\rho_0 \frac{\partial \mathbf{v}_1}{\partial t} = -\nabla p_1 + \mu \nabla^2 \mathbf{v}_1 + (\mu_b + \frac{1}{3}\mu) \nabla (\nabla \cdot \mathbf{v}_1). \quad (2.7)$$

Repeating the above procedure for the terms of order two in ε , and averaging the resulting equations over a period of oscillation, we can obtain the second-order problem as the following set of equations

$$\left\langle \frac{\partial \rho_2}{\partial t} \right\rangle + \rho_0 \nabla \cdot \langle \mathbf{v}_2 \rangle = -\nabla \cdot \langle \rho_1 \mathbf{v}_1 \rangle, \quad (2.8)$$

$$\begin{aligned} \rho_0 \left\langle \frac{\partial \mathbf{v}_2}{\partial t} \right\rangle + \left\langle \rho_1 \frac{\partial \mathbf{v}_1}{\partial t} \right\rangle + \rho_0 \langle \mathbf{v}_1 \cdot \nabla \mathbf{v}_1 \rangle \\ = -\nabla \langle p_2 \rangle + \mu \nabla^2 \langle \mathbf{v}_2 \rangle + (\mu_b + \frac{1}{3}\mu) \nabla (\nabla \cdot \langle \mathbf{v}_2 \rangle), \end{aligned} \quad (2.9)$$

where $\langle A \rangle$ denotes the time average of the quantity A over a full oscillation time period. The inertial terms in Eq. (2.9), as Stuart [40] pointed out, can be significant and must be retained in the formulation for a general case. In addition, the last term in Eq. (2.9) associated with the bulk viscosity must also be retained in order to fully elucidate the viscous attenuation of the acoustic wave, both within and without the boundary layer.

2.2.2 Boundary Conditions

We presented in Section 2.2.1 the governing equations that are needed to develop a numeric model for our sharp-edge-based system. In this section, appropriate boundary conditions are identified to complement the governing equations. As the precise boundary conditions are problem-specific, in this section we discuss the boundary conditions that are commonly employed for various case scenarios considered in this dissertation, and the boundary conditions typically used for the first-order problem are first discussed.

2.2.2.1 Actuation for sharp-edge devices

As described in Section 2.1, these sharp-edge-based devices are bonded onto thin glass slides and usually activated by circular piezoelectric transducers. As a result, the diameter of the piezoelectric transducer, as can be seen in Fig. 2.1(a), is usually much larger than the transverse width of the channel, so that the channel can be assumed to be subject to a plane wave parallel to the x direction and traveling in the y direction. Hence, we assume that the boundary portions Γ_t and Γ_b (the solid lines in Fig. 2.5(b)) are subject to a displacement field $\mathbf{w}(\mathbf{x}, t)$ of the following form

$$\begin{aligned}\mathbf{w}(\mathbf{x}_t, t) &= \mathbf{w}_c^t \cos(2\pi ft) + \mathbf{w}_s^t \sin(2\pi ft), \\ \mathbf{w}(\mathbf{x}_b, t) &= \mathbf{w}_c^b \cos(2\pi ft) + \mathbf{w}_s^b \sin(2\pi ft),\end{aligned}\tag{2.10}$$

where \mathbf{w}_c^t , \mathbf{w}_c^b , \mathbf{w}_s^t , and \mathbf{w}_s^b are the vector-valued constants, while f is the transducer oscillation frequency. Thus, the boundary conditions on Γ_t and Γ_b for the first-order problem are $\mathbf{v}_1(\mathbf{x}_{t,b}, t) = \partial\mathbf{w}(\mathbf{x}_{t,b}, t)/\partial t$, which gives

$$\mathbf{v}_1(\mathbf{x}_{t,b}, t) = -2\pi f[\mathbf{w}_c^{t,b} \sin(2\pi ft) - \mathbf{w}_s^{t,b} \cos(2\pi ft)],\tag{2.11}$$

where the subscripts and superscripts t and b stand for ‘on Γ_t ’ and ‘on Γ_b ’, respectively.

Having mentioned the two specific cases of actuation, we remark that the modes of actuation for microacoustofluidic devices are very diverse. The exact actuation conditions are usually difficult to identify experimentally and the usual approach in acoustofluidics is to try different physically meaningful boundary conditions numerically and validate those with the experimentally observed fluid patterns.

Noting this, we now describe the usually employed boundary conditions on the first-order problem for the remaining channel boundaries.

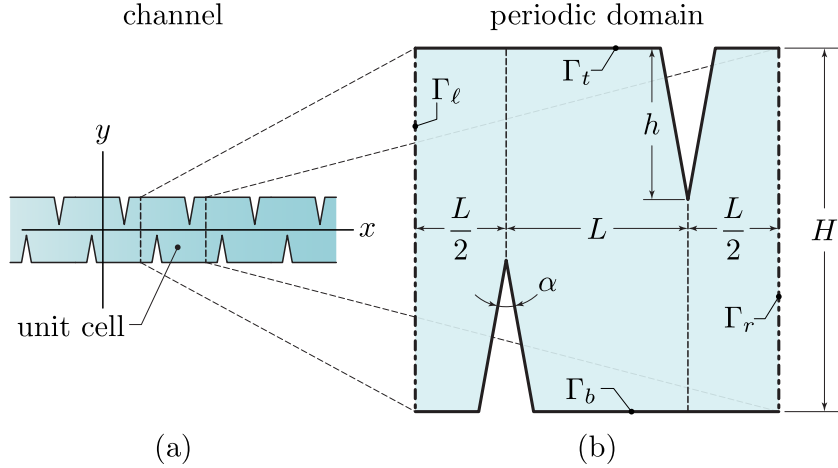


Figure 2.5. (a) A portion of the microfluidics device. (b) Definition of a periodic cell forming the device.

2.2.2.2 Periodic Boundary Conditions

Referring to Figs. 2.1 and 2.5, we note that sharp-edge-based devices usually consist of an assemblage of identical cells, thereby allowing one to use a much smaller computational domain consisting of just one periodic cell, as depicted in Fig. 2.5. Hence, for both the first- and second-order problems, we enforce periodic boundary conditions along the x direction, that is on Γ_ℓ and Γ_r . Specifically, for all pairs of homologous points \mathbf{x}_ℓ and \mathbf{x}_r on Γ_ℓ and Γ_r , respectively, we enforce that

$$\mathbf{v}_1(\mathbf{x}_\ell, t) = \mathbf{v}_1(\mathbf{x}_r, t) \quad \text{and} \quad \mathbf{v}_2(\mathbf{x}_\ell, t) = \mathbf{v}_2(\mathbf{x}_r, t). \quad (2.12)$$

2.2.2.3 Boundary conditions on second-order problem

For the boundary conditions on the second-order problem, we follow the approach by Bradley [41]. The boundary condition at the bounding surface of the microfluidic channel is the no-slip condition. Bradley noted that in case of rigid boundaries, this simply refers to the velocity being zero at the boundary but in case of moving boundaries, the no-slip condition needs to be satisfied at the displaced position of the surface and not at the initial (or rest) position. Thus, for a surface that has

moved from $\mathbf{r} = \mathbf{r}_0$ to $\mathbf{r} = \mathbf{r}_0 + \mathbf{u}(\mathbf{r}_0, t)$, the no-slip boundary condition (relative to the solid surface) can be expressed as

$$\mathbf{v}(\mathbf{r}, t)|_{\mathbf{r}=\mathbf{r}_0+\mathbf{u}(\mathbf{r}_0,t)} = \frac{\partial}{\partial t}\mathbf{u}(\mathbf{r}_0, t). \quad (2.13)$$

A Taylor series expansion of this boundary condition about the rest surface of the solid boundary yields

$$\mathbf{v}(\mathbf{r}, t)|_{\mathbf{r}=\mathbf{r}_0+\mathbf{u}(\mathbf{r}_0,t)} = \mathbf{v}(\mathbf{r}, t)|_{\mathbf{r}=\mathbf{r}_0} + \mathbf{u}(\mathbf{r}_0, t) \cdot \nabla \mathbf{v}(\mathbf{r}, t)|_{\mathbf{r}=\mathbf{r}_0} + \mathcal{O}(\epsilon^3) = \frac{\partial}{\partial t}\mathbf{u}(\mathbf{r}_0, t). \quad (2.14)$$

Thus the boundary condition to be satisfied by the second-order streaming flow field should be the time-averaged, $\mathcal{O}(\epsilon^2)$ component of the above expression, which gives

$$\mathbf{v}_2(\mathbf{r}, t) = -\langle (\mathbf{u}(\mathbf{r}_0, t) \cdot \nabla) \mathbf{v}_1(\mathbf{r}, t) \rangle. \quad (2.15)$$

We note, however, that in many microacoustofluidic devices, the displacement of the surface is usually in sub-nanometer range, thus it is possible to neglect the minute difference between the initial and the deformed positions in some cases. Noting this, sometimes a zero-velocity boundary condition (as employed by Muller *et al.* [42]) is employed for the second-order problem on the boundaries.

2.2.3 Mean trajectories

The most common method for flow visualization in acoustofluidic devices is the tracking of fluorescent polystyrene spherical beads placed in the fluid. To compare our numerical predictions against the experimental observations, we include a particle tracking strategy in our numerical formulation. By modeling the bead as a wave scatterer, Settnes and Bruus [43] calculated the acoustic radiation force acting on a bead of radius a , mass density ρ_p , and compressibility κ_p under the influence of a wave in the flow as

$$\mathbf{F}^{\text{rad}} = -\pi a^3 \left[\frac{2\kappa_0}{3} \text{Re}[f_1^* p_1^* \nabla p_1] - \rho_0 \text{Re}[f_2^* \mathbf{v}_1^* \cdot \nabla \mathbf{v}_1] \right], \quad (2.16)$$

where $\kappa_0 = 1/(\rho_0 c_0^2)$ is the compressibility of the fluid, $\text{Re}(A)$ denotes the real part of quantity A , the asterisk denotes the conjugate of the quantity and f_1 and f_2 are

given by:

$$f_1 = 1 - \frac{\kappa_p}{\kappa_0} \quad \text{and} \quad f_2 = \frac{2(1 - \gamma)(\rho_p - \rho_0)}{2\rho_p + \rho_0(1 - 3\gamma)}, \quad (2.17)$$

with

$$\gamma = -\frac{3}{2}[1 + \imath(1 + \tilde{\delta})]\tilde{\delta}, \quad \tilde{\delta} = \frac{\delta}{a}, \quad \delta = \sqrt{\frac{\mu}{\pi f \rho_0}}. \quad (2.18)$$

It must be noted that since we do not know *a priori* the type of waves setup in our systems, we use the general form of the radiation force, as mentioned in Eq. (2.16), without making any assumptions about the nature of the wave. In addition to the radiation force, a bead is assumed to be subject to a drag force proportional to $\mathbf{v}_p - \langle \mathbf{v}_2 \rangle$, which is the velocity of the bead relative to the streaming velocity. When wall effects are negligible, the drag force is estimated *via* the simple formula $\mathbf{F}^{\text{drag}} = 6\pi\mu a(\langle \mathbf{v}_2 \rangle - \mathbf{v}_p)$. The motion of the bead can then be predicted *via* the application of Newton's second law

$$m_p \frac{d\mathbf{v}_p}{dt} = \mathbf{F}^{\text{rad}} + \mathbf{F}^{\text{drag}}, \quad (2.19)$$

where m_p is the mass of the bead. In many microacoustofluidic problems the inertia of the bead can be neglected since the characteristic time of acceleration is small in comparison to the time scale of the motion of the particles [44]. Doing so, Eq. (2.19) can be solved for \mathbf{v}_p

$$\mathbf{v}_p = \langle \mathbf{v}_2 \rangle + \frac{\mathbf{F}^{\text{rad}}}{6\pi\mu a}. \quad (2.20)$$

For an “ideal tracer”, a bead with the same density and compressibility as the surrounding fluid, $\mathbf{F}^{\text{rad}} = \mathbf{0}$ and the bead's velocity coincides with the streaming velocity. However, the trajectories of the streaming velocity field are not fully representative of the mean trajectories of the fluid's particles as the latter are subject to a drift effect known as Stokes drift [45]. The theory around the Stokes drift is developed without reference to the motion of a bead in the fluid and therefore it can be viewed as a theory for the identification of mean trajectories of fluid particles. We adopt the theory of Lagrangian mean flow described by Bühler [46], and employed by Vanneste and Bühler [47], in which mean particle paths are the trajectories of a velocity field referred to as the Lagrangian velocity, denoted by

\mathbf{v}^L , and given by

$$\mathbf{v}^L = \langle \mathbf{v}_2 \rangle + \langle (\boldsymbol{\xi}_1 \cdot \nabla) \mathbf{v}_1 \rangle, \quad (2.21)$$

where the field $\boldsymbol{\xi}_1(\mathbf{x}, t)$ is the first-order approximation of the lift field $\boldsymbol{\xi}(\mathbf{x}, t)$. The latter is defined such that $\mathbf{x} + \boldsymbol{\xi}$ represents the true position at time t of a particle with mean position at \mathbf{x} (also at time t). By asymptotic expansion, $\boldsymbol{\xi}_1$ is such that

$$\frac{\partial \boldsymbol{\xi}_1}{\partial t} = \mathbf{v}_1. \quad (2.22)$$

For a steady problem, the trajectories of the fluid particles are then the streamlines of \mathbf{v}^L , which can be calculated by combining the second-order solution with the calculation of the lift field, which in turn is obtained from the first-order solution.

2.2.4 Numerical Implementation

2.2.5 Overview of algorithm

Having described the governing equations and the common boundary conditions, we present the general solution approach employed to calculate the solutions.

1. Given a computational domain and the appropriate problem-specific boundary conditions, we seek time-harmonic solutions for \mathbf{v}_1 and p_1 in the first-order problem governed by Eqs. (2.6) and (2.7).
2. Having obtained the first-order solution, the forcing terms and boundary conditions for the second-order problem are calculated and employed with Eqs. (2.8) and (2.9) to solve for $\langle \mathbf{v}_2 \rangle$ and $\langle p_2 \rangle$ in the second-order problem.
3. Combining information from the first- and second-order solution, the acoustic radiation force, the hydrodynamic drag as well as the Stokes drift terms are calculated in accordance with the theory described in the Sec. 2.2.3. Lastly, using these forces and correction terms, the mean trajectories of the particles are calculated.

The numerical solution was obtained via an in-house finite element code based on the `deal.II` finite element library [48, 49] (<http://www.dealii.org>). While our numerical implementation is dimension independent, most of the solutions dis-

cussed later are for two-dimensional problems. The simulations for each application considered in this dissertation are presented in the corresponding chapters.

2.3 Summary

In this chapter, we first introduce the concept of the generation of acoustic streaming by acoustically oscillating sharp-edge structures, typical configuration of sharp-edge-based devices, their experimental setup and design parameter of sharp-edge structure, and then we present preliminary results on the generation of acoustic streaming using oscillating sharp-edge structures. By engineering acoustic streaming patterns through the alteration of design of sharp-edge structure, we can achieve various microfluidic applications as presented in the following chapters. Furthermore, we propose a numeric model to simulate the acoustic streaming induced by oscillating sharp-edge structures. With the proposed numeric model, we are able to predict the performance of sharp-edge-based devices; in other words, we can numerically optimize the design of sharp-edge-based devices prior to their fabrication.

Sharp-edge-based acoustofluidic micromixer

In Chapter 2, we have presented preliminary experimental results showing the generation of acoustic streaming by acoustically oscillating sharp-edge structures. In this chapter, we demonstrate rapid and homogeneous mixing of fluid inside a microfluidic channel *via* the acoustic streaming effect induced by the oscillation of sidewall sharp-edges. By optimizing the design of the sharp-edges, excellent mixing performance and fast mixing speed can be achieved in a simple device, making our sharp-edge-based acoustofluidic micromixer a promising candidate for a wide variety of applications. The work presented in this chapter has been reported on The 17th International Conference on Miniaturized Systems for Chemistry and Life Sciences (MicroTAS 2013), published in Journal of *Lab on a Chip* [50] and selected as a *Lab on a Chip HOT Article* of 2013.

3.1 Motivation

The ability to achieve rapid and homogeneous mixing of chemical/biological species enables a wide variety of applications, such as chemical kinetic studies [51, 52] and nanomaterial synthesis [53, 54]. While microfluidic devices seem to be an excellent platform for carrying out these studies due to their short reaction times, high throughput, and reduced reagent consumption, effectively mixing fluids at the microscale is not a trivial process [55–57]. Due to inherently small channel dimen-

sions, the flow of fluid in microfluidic devices is usually laminar; under laminar flow conditions, viscous forces dominate over inertial forces and fluids are not easily mixed. To enable microfluidic applications where uniform mixing of fluids is required, a number of micromixing methods have been reported. These methods include, but are not limited to, chaotic advection [58–60], hydrodynamic focusing [61,62], electrokinetically driven mixing [63–65], 3D combinatorial mixing [66,67], meandering channels as well as magnetically [68,69], thermally [70], and optically [71] induced mixing.

Recently, acoustic-based micromixers have attracted significant attention due to their non-invasive nature [72–74] and simple mixing mechanism. In acoustic-based mixers, acoustic waves propagate into fluid media and induce pressure fluctuations, resulting in the disturbance of the laminar-flow pattern to facilitate mixing [75–81]. The mixing performance of acoustic-based mixers can be further improved through the use of microbubbles in the microfluidic channel. When microbubbles are coupled with an acoustic wave, the acoustic streaming phenomenon [25] is developed. This phenomenon results in a more prominent perturbation of the surrounding fluids, greatly facilitating the mass transport of fluids. Thus far, microbubble-based acoustic mixers [9–12] have been used for characterizing enzyme reactions [52], enhancing DNA hybridization [9,82], generating chemical gradients [83], and developing advanced optofluidic devices [26]. Although acoustically driven, bubble-based micromixers have shown tremendous potential in a wide variety of applications, there are many concerns regarding bubble instability [11,26], heat generation [80], and inconvenient bubble-trapping processes. To take advantage of acoustic streaming without the drawbacks of microbubbles [20,84], we should explore alternative methods that can effectively and conveniently generate acoustic streaming. In this chapter, we demonstrate rapid and homogeneous micromixing through the acoustic streaming induced by the oscillation of the sidewall microstructures known as “sharp-edge structure”. This sharp-edge-based acoustofluidic micromixer can achieve rapid, homogeneous mixing with minimum hardware. In addition, the operation of the devices is extremely simple, and the mixing can be conveniently toggled on and off.

3.2 Working mechanism

Figure 3.1(a) shows the experimental setup of the sharp-edge-based acoustofluidic micromixer. A single-layer polydimethylsiloxane (PDMS) channel with eight sharp-edge structures on its sidewall (four on each side) was fabricated and bonded onto a glass slide. A piezoelectric transducer (model no. 273-073, RadioShack Corp.) was then attached adjacent to the PDMS channel using a thin layer of epoxy (PermaPoxy™ 5 Minute General Purpose, Permatex). Upon the actuation of the piezoelectric transducer, the sharp-edge structures were acoustically oscillated to generate a pair of counter-rotating vortices (double-ring recirculating flows) in the fluid around the tip of each sharp-edge structure, as shown in Fig. 3.1(b). The double-ring recirculating flows will drastically enhance the mass transport across the channel width by breaking the interface of laminar fluids. Figure 3.1(c) shows the design of the microchannel with sidewall sharp-edge structures. The length, width and depth of the microchannel were 1 cm, 600 μm , and 50 μm , respectively; each sharp-edge structure was designed to have a constant height of 250 μm and variable tip angle (α). Four different tip angles, 15°, 30°, 45° and 60°, were chosen to investigate the resulting acoustic streaming effect and then to determine the optimal tip angle for best mixing performance.

To demonstrate and characterize the fluid flow pattern inside the channel due to the acoustic streaming, a solution containing 1.9 μm -diameter dragon green fluorescent beads (Bangs Laboratory) was first infused into the channel. Figure 3.2(a) shows the flow pattern of fluorescent beads in the absence of acoustic activation (with the piezoelectric transducer OFF). In the presence of acoustic activation (with the piezoelectric transducer ON), oscillating sharp-edge structure induced a strong acoustic streaming effect (Fig. 3.2(b)). The resulting acoustic streaming greatly enhanced the mass transport of the two fluids by perturbing the bulk flow and breaking the interface of laminar flow, thereby enabling fast and homogeneous mixing.

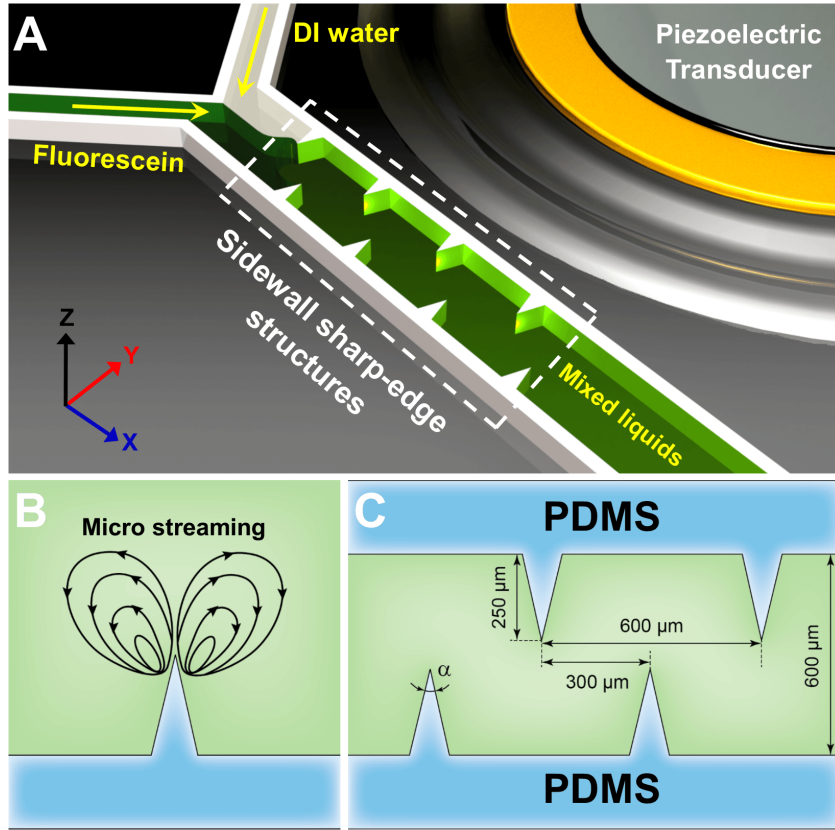


Figure 3.1. (a) Schematic of the sharp-edge-based acoustofluidic mixing device. This device includes a PDMS microfluidic channel and a piezoelectric transducer. (b) Schematic showing the acoustic streaming phenomenon developed around the tip of an acoustically oscillated sharp-edge structure. (c) Schematic showing the detailed dimensions of the channel and sharp-edge structure.

3.3 Results and Discussions

3.3.1 Determination of driving frequency

The mixing performance of our sharp-edge-based micromixer was characterized by co-injecting DI water and fluorescent dye (fluorescein) into the channel through two separate inlets. The sharp-edge structures were acoustically oscillated by the piezoelectric transducer, which was driven by an amplified sine-wave signal from a function generator (AFG3011C, Tektronix) and an amplifier (25A250A, Amplifier Research).

To determine the driving frequency of the piezoelectric transducer at which the

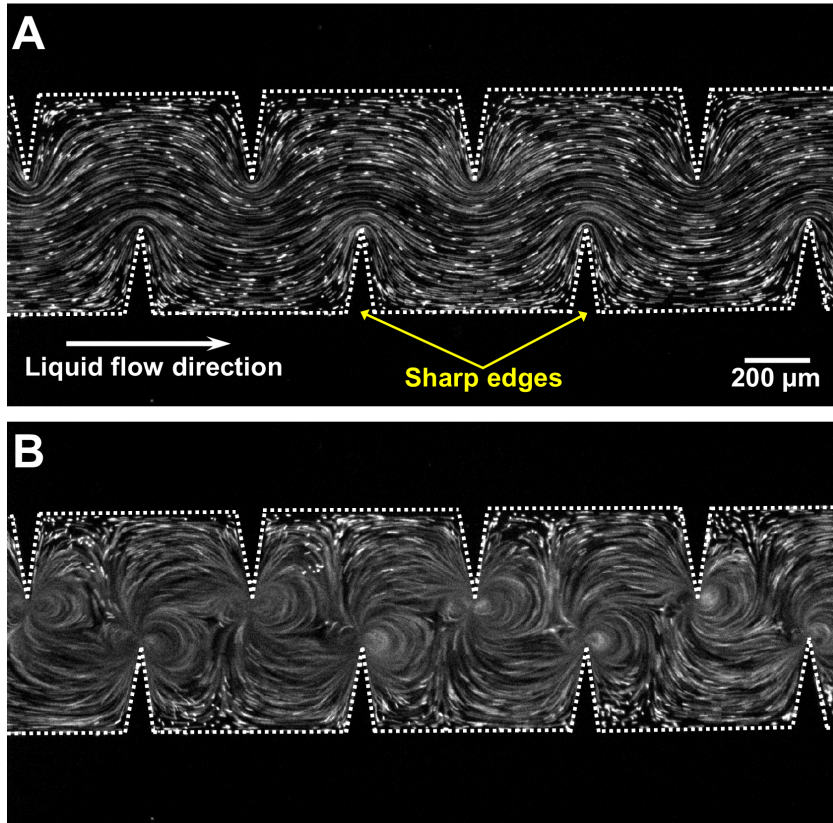


Figure 3.2. Characterization of the flow pattern with/without acoustic streaming. (a) In the absence of acoustic waves, a laminar flow pattern was observed in a solution containing fluorescent beads. (b) In the presence of acoustic waves, acoustic streaming was developed in the liquid around the tips of sharp-edge structures.

oscillating sharp-edge structures generate the strongest acoustic streaming effect, we first tested the device with 15° sharp-edge structures, and swept the frequency with a 50 Hz increment from 1 kHz to 100 kHz. Our experimental results indicated that the strongest acoustic streaming effect was generated when the sharp-edge structures were excited at the frequency of 4.50 kHz. Figure 3.3(a) shows the unmixed laminar flow profile at a flow rate of $1 \mu\text{L}/\text{min}$ with the piezoelectric transducer OFF, in which a clear fluid interface was observed. Figures 3.3(b) - (d) show the mixing results due to the presence of acoustic waves at frequencies of 4.25 kHz, 4.50 kHz, and 4.75 kHz, respectively. Homogeneous mixing of DI water and fluorescein was achieved when the sharp-edge structures were excited at the frequencies of 4.50 kHz and 4.75 kHz, while incomplete mixing was observed at the frequency of 4.25 kHz. To further verify the mixing performance and identify the

optimized driving frequency of the piezoelectric transducer, the cross-sectional dye concentration profiles (the dashed lines in Fig. 3.3) were plotted by measuring the gray-scale values of the experimental images. Figure 3.3(e) shows the normalized dye concentration profile across the channel width under the three driving frequencies. The concentration profiles show that a uniform gray-scale value distribution across the channel width was observed at the frequency of 4.50 kHz, suggesting that 4.50 kHz is the proper driving frequency to develop the strongest acoustic streaming phenomenon and thus, achieve optimized mixing performance.

In our experiments, in fact, we also tested the devices with three different tip angles (30°, 45° and 60°), and swept the frequency with a 50 Hz increment from 1 kHz to 100 kHz. From the experimental results, we found that the amplitude of motion was dependent on the resonant frequency of the piezoelectric transducer, which is about 4.50 kHz, instead of the resonance frequency of sharp-edge structure. In other words, 4.50 kHz was the optimized frequency for all the devices with different angles, explaining why we compared mixing performance with different tip angles at the frequency of 4.50 kHz. To be more specific, we were unable to identify any optimum driving frequencies for the devices with 30°, 45° and 60°, since no acceptable mixing was even observed for the three cases. Therefore, we were unable to give any discussion about what are the optimum driving frequency for the devices with 30°, 45° and 60°. As a result, the frequency of 4.50 kHz was used in all the following experiments.

3.3.2 Mixing performances of various tip angles

Once the driving frequency was determined, we investigated the effect of the tip angle of sharp-edge structure on the mixing performance. To quantitatively characterize the mixing performance along the entire length of the channel, we measured the mixing index (M) of fluids at five different positions (indicated as 1, 2, 3, 4, and 5 in Fig. 3.4) along the channel. The mixing index was defined as the standard deviation of normalized gray-scale value, which were extracted from the experimental images obtained, and was calculated based on the following equation [85]:

$$M = \sqrt{\frac{1}{n} \sum_{i=1}^n \left(\frac{I_i - I_m}{I_m} \right)^2} \quad (3.1)$$

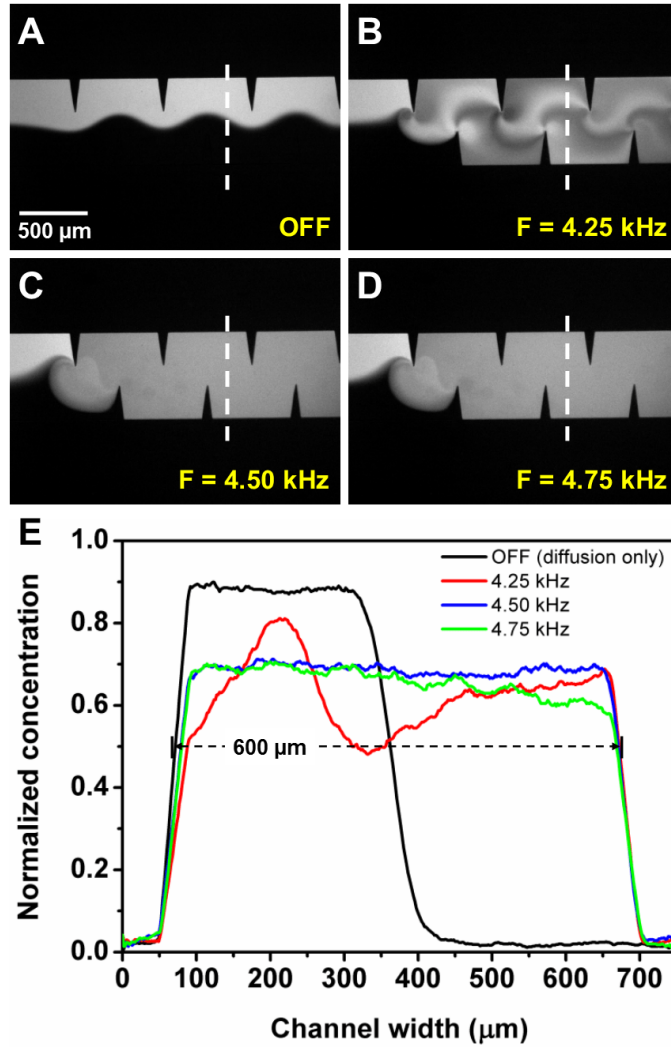


Figure 3.3. Characterization of the mixing performance under different driving frequencies of the piezoelectric transducer for our sharp-edge-based acoustofluidic micromixer. (a) A laminar flow pattern was observed when the piezoelectric transducer was off. (b) 4.25 kHz: Incomplete mixing. (c) 4.50 kHz and (d) 4.75 kHz: Excellent mixing was achieved. (e) Plots of normalized fluorescent concentration across the width of channel.

where I_i is the gray-scale value at a given point, I_m is the average gray-scale value, and n is the total number of sampled points along the width of the channel. By using this equation, we can know that the mixing index is actually the standard deviation of gray-scale values along the width of the channel. Therefore, evaluating the mixing performance by calculating the mixing index should have the least uncertainties.

A mixing index of 0.5 indicates completely unmixed fluids, while a mixing in-



Figure 3.4. Schematic of the microchannel with sidewall sharp-edge structures. The mixing index was characterized at five different positions (positions 1 – 5, indicated by the dashed white lines in the figure).

dex of 0.0 indicates completely mixed fluids. A mixing index of 0.1 was chosen as the upper-level threshold for acceptable mixing. Figure 3.5 shows the mixing efficiencies of the four different tip angles of sharp-edge structures at a flow rate of $2 \mu\text{L}/\text{min}$ ($4 \mu\text{L}/\text{min}$ for the total flow rate of the two co-injected fluids), the driving frequency of 4.50 kHz, and a driving voltage of 31 V_{PP} (peak to peak). With a tip angle of 15° , a mixing index of 0.065 was achieved at position 2 (Fig. 3.5(a)), suggesting excellent mixing of DI water and fluorescein. For sharp-edge structure with a tip angle of 30° , acceptable mixing was observed only at position 5 (Fig. 3.5(b)), suggesting that a longer mixing distance was required. Incomplete mixing was observed for sharp-edge structures with a tip angle of 45° (Fig. 3.5(c)). With a tip angle of 60° , a side-by-side laminar flow was observed due to the unmixed fluids (even in the presence of acoustic wave), and only negligible mixing, which was caused by diffusion, was observed at downstream positions (Fig. 3.5(d)). The results showed that as the tip angle of sharp-edge structure was decreased, the mixing performance significantly improved. The results can be explained by approximating the oscillation of sharp-edge structure as the vibration of cantilever. As shown in Fig. 3.6, the sharp-edge structure is connected to the top (*i.e.*, the bulk PDMS) wall and bottom wall (*i.e.*, the glass slide) of the channel, which suggests that the tip vibration is restricted in the vertical direction (side view). At the tip region, however, the sharp-edge structure is infirmly bonded to the bottom wall of the channel, because the surface area is too small to provide sufficient bonding force for the sharp-edge structure to be firmly bonded to the the bottom wall. As a result, once an external force is applied (acoustic energy in this case), the infirm connection of tip to the bottom wall of the channel would induce the tip vibration in the horizontal direction as shown in Fig. 3.6 (top view). For the vibration of

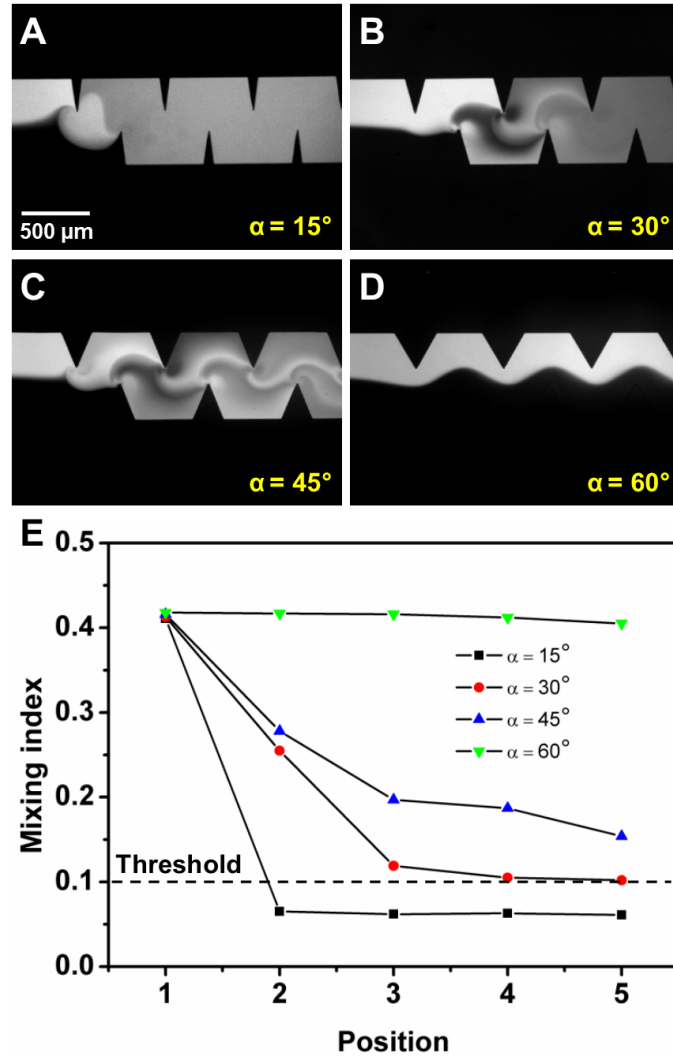


Figure 3.5. Characterization of the mixing performance with different tip angles of sharp-edge structures. (a) 15° : Excellent mixing was quickly achieved after position 2. (b) 30° : Acceptable mixing was achieved after position 4. (c) 45° : Incomplete mixing. (d) 60° : A laminar flow pattern was observed even if the piezoelectric transducer was ON. (e) Plots of mixing indices at different positions along the microchannel with different tip angles of sharp-edge structures.

cantilever, one can use the following equation,

$$k = \frac{F}{\delta} = \frac{Ewt^3}{4L^3} \quad (3.2)$$

where k is the spring constant, E is the Young's modulus of material, w is the width of cantilever, t is the thickness of the cantilever, and L is the length of the cantilever.

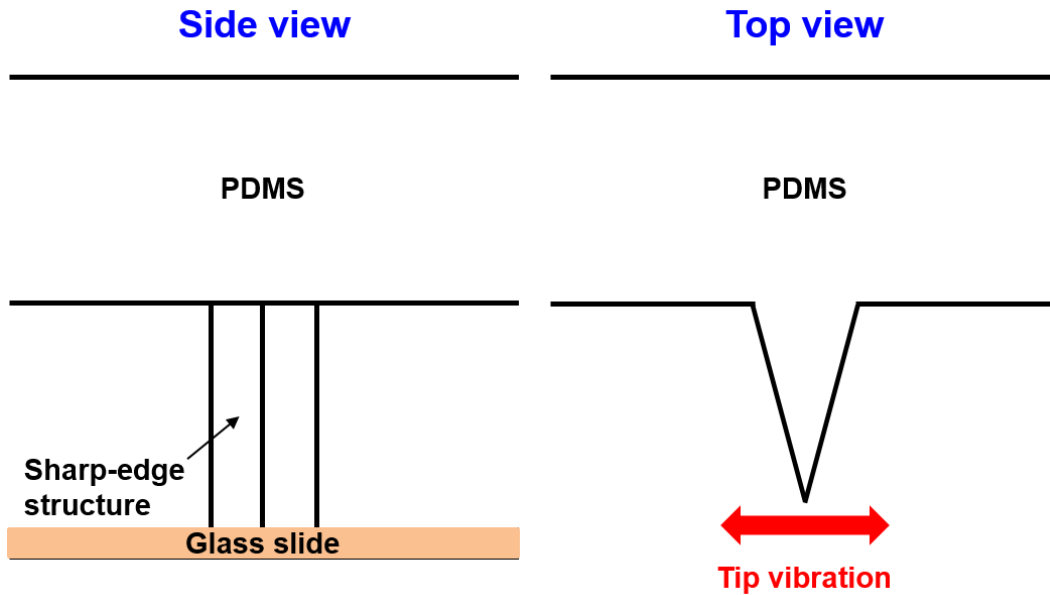


Figure 3.6. Schematic of the sharp-edge structure in the microfluidic channel.

Sharp-edge structures with different tip angles in this study all have the same values for Young’s modulus, equivalent widths ($50\ \mu\text{m}$), and equivalent lengths ($250\ \mu\text{m}$). The only variable that changes with varying tip angles is the thickness, which increases as the angle increases. Thus the sharp-edge structure with a smaller tip angle should have a lower spring constant. If the input power is constant, a lower spring constant of the cantilever will cause a larger amplitude of vibration at the free end of the cantilever. Treating each single sharp-edge structure as one cantilever, similarly, the sharp-edge structures with a tip angle of 15° should have the largest vibration amplitude because of its smallest spring constant. This explains why the sharp-edge structures with the tip angle of 15° induced stronger acoustic streaming effect than those with tip angles of 30° , 45° , or 60° .

3.3.3 Mixing performances under different driving voltages

Mixing performance was further characterized by applying different driving voltages to the piezoelectric transducer. Figure 3.7 shows the mixing performance with different driving voltages at a flow rate of $2\ \mu\text{L}/\text{min}$ and the driving frequency of $4.50\ \text{kHz}$. The results show that as the driving voltage of the piezoelectric trans-

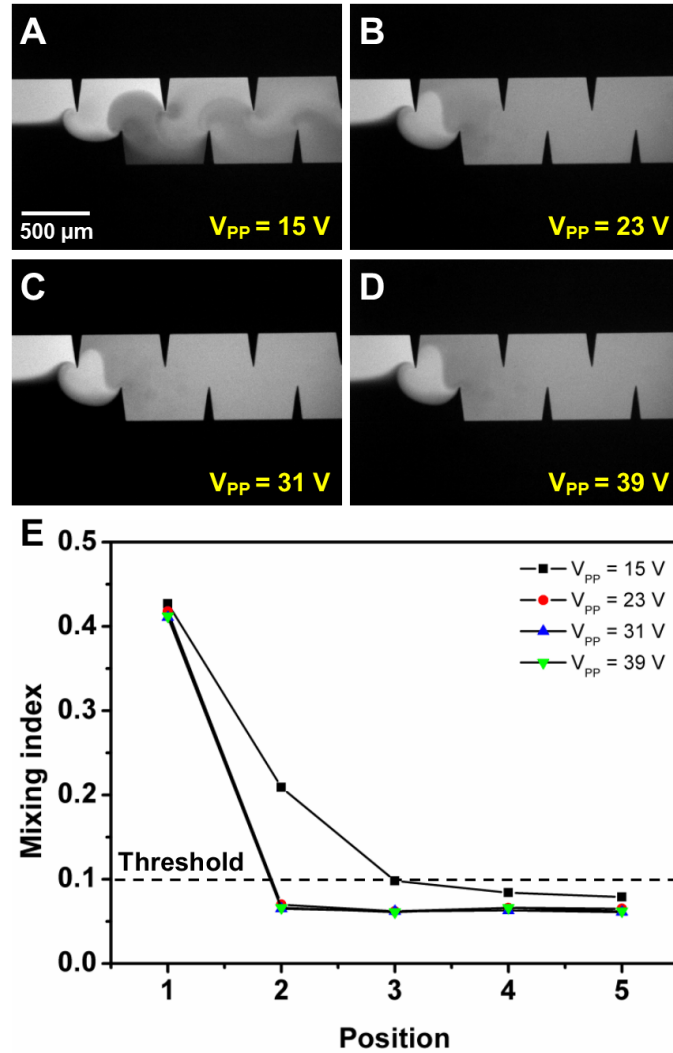


Figure 3.7. Characterization of the mixing performance under different driving voltages. (a) 15 V_{PP} : Acceptable mixing was achieved after position 3. (b) 23 V_{PP} , (c) 31 V_{PP} , and (d) 39 V_{PP} : Acceptable mixing was quickly achieved after position 2. (e) Plots of mixing indices at different positions along the microchannel under different driving voltages.

ducer was increased, the mixing efficiency was improved, and acceptable mixing was observed starting from position 2 with driving voltages of 23 V_{PP} , 31 V_{PP} , and 39 V_{PP} . With a driving voltage of 15 V_{PP} , the acceptable mixing index was achieved at position 3, suggesting that a lower driving voltage induced weaker acoustic streaming effect; therefore a longer mixing distance was needed.

3.3.4 Mixing performances under different flow rates

Figure 3.8 shows the mixing efficiency at different flow rates (1, 2, 3, 4, and 5 $\mu\text{L}/\text{min}$) with the driving frequency of 4.50 kHz and the driving voltage of 31 V_{PP} . At lower flow rates (*i.e.*, 1 and 2 $\mu\text{L}/\text{min}$), acceptable mixing was achieved at position 2, which suggests excellent mixing of the two fluids and shorter mixing distances were needed for lower flow rates (Figs. 3.8(a) and (b)). For higher flow rates (*i.e.*, 3, 4, and 5 $\mu\text{L}/\text{min}$), the mixing index at position 2 was increased with an increase in flow rate, and acceptable mixing was only observed after passing position 3. The results suggest that the mixing index increases as flow rate increases, since the ability to oscillate sharp-edge structures to induce acoustic streaming might be suppressed by high flow rates.

The upper limit of flow rate, by which we achieved a mixing index less than 0.1 after passing position 2 (after the first pair of sharp-edges), was 2 $\mu\text{L}/\text{min}$ (4 $\mu\text{L}/\text{min}$ for the total flow rate of two coinjected fluids), as shown in Fig. 3.8(e). Although mixing indices less than 0.1 were achieved with the flow rates higher than 2 $\mu\text{L}/\text{min}$, they were only observed after passing position 3, suggesting a longer mixing distance. Finally we characterized the mixing time of the sharp-edge-based micromixer. The average mixing time (τ_s) was estimated using the following equation,

$$\tau_s = \frac{L_{mix}}{V_{avg}} \quad (3.3)$$

where τ_s is the mixing time, L_{mix} is the distance from unmixed to completely mixed regions, and V_{avg} is the average fluid velocity. The mixing distance was measured to be approximately 400 μm from Fig. 3.8(b), and the average fluid velocity was calculated to be 2.2 mm/s by dividing the combined flow rate by the cross-sectional area of the channel (600 μm by 50 μm). The mixing time was thus calculated to be around 180 ms which is comparable to those of existing microfluidic mixers [9, 11, 74–77]. We believe that the mixing time can be further shortened through the optimization of design parameters, such as the distance between consecutive single sharp-edge structure or the height of sharp-edge structure.

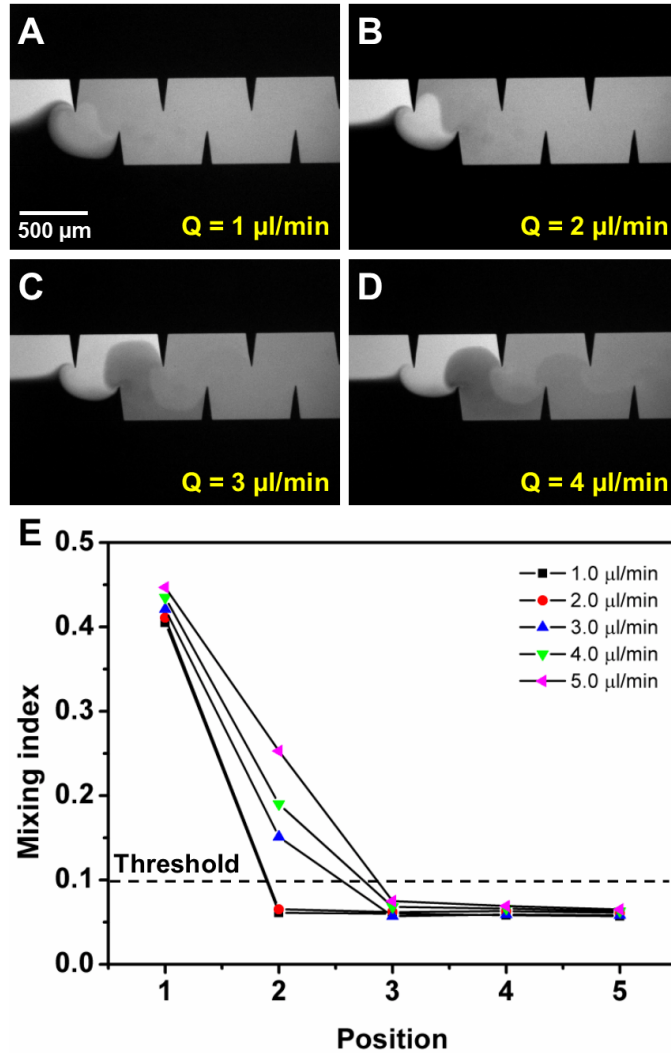


Figure 3.8. Characterization of the mixing performance under different flow rates. (a) $1 \mu\text{L/min}$: Excellent mixing due to low flow rate. (b) $2 \mu\text{L/min}$: Acceptable mixing was achieved. (c) $3 \mu\text{L/min}$ and (d) $4 \mu\text{L/min}$: Acceptable mixing was achieved only after position 3. (e) Plots of mixing indices at different positions along the microchannel under different flow rates..

3.4 Summary

In conclusion, we present an acoustofluidic micromixer based on the acoustic streaming effects induced by oscillating sharp-edge structures. The recirculating flows induced by the oscillation of sharp-edge structures allow two fluids to interchange and thus enhances the mass transport across the channel, greatly improving the mixing efficiency. We have demonstrated that homogeneous mixing across the

channel width can be achieved and the mixing time was calculated to be ~ 180 ms. The effects of the geometry of sharp-edge structure, the driving frequency and driving voltage of the piezoelectric transducer, and the flow rate on mixing performance were thoroughly investigated. Our sharp-edge-based acoustofluidic micromixer has many desirable characteristics, such as its excellent mixing performance, simplicity, convenient and stable operation, fast mixing speed, and ability to be toggled on-and-off. These characteristics make it promising for a wide variety of lab-on-a-chip applications.

Sharp-edge-based acoustofluidic sputum liquefier

In Chapter 3, we have demonstrated rapid and homogeneous fluid mixing by using our sharp-edge-based acoustofluidic micromixer for rapid and homogeneous fluid mixing. Extending the capability of our micromixer, in this chapter, we demonstrate the first microfluidic-based on-chip liquefaction device for human sputum samples. Our device is based on an acoustofluidic micromixer using oscillating sharp-edge structures. This acoustofluidic sputum liquefier can effectively and uniformly liquefy sputum samples at a throughput of $30 \mu\text{L}/\text{min}$. Cell viability and integrity of the sputum samples are maintained during the sputum liquefaction process. Our acoustofluidic sputum liquefier can be conveniently integrated with other microfluidic units to enable automated on-chip sputum processing and analysis. The work presented in this chapter has been reported on the international conference of 2015 Annual Meeting of Biomedical Engineering Society (BMES), published and featured as the **Front Cover Article** in *Journal of Lab on a Chip* [86].

4.1 Motivation

Effective processing and analysis of sputum samples are critical to the development of diagnostic platforms and personalized treatment approaches for pulmonary diseases, ranging from asthma [87, 88] to tuberculosis (TB) [89, 90]. The current

sputum processing and analysis techniques involve labor-intensive procedures that are typically performed only at specialized research and clinical centers. Given the complexity of sputum processing and analysis protocols, appropriate training and quality control are required of the staff that perform the tests. The need for highly trained personnel, however, limits the widespread utilization of the current sputum processing and analysis approaches for the care of patients with pulmonary diseases. Furthermore, since the processing and analysis of induced sputum samples is operator-dependent, the possibility of error or inter-operator variability can potentially confound the results. Moreover, all human specimens, even from healthy individuals, may be infectious. Conventional sputum processing and analysis assays also have biosafety concerns because in these approaches, sputum samples need to be handled manually by the operator and run through several instruments. Therefore, there is a pressing need for a new approach that can liquefy and analyze sputum in a closed liquid environment within a single device in an automated manner. This type of approach will not only enable biohazard containment but will also promote standardization and reproducibility of liquefaction relative to the traditional, operator-dependent method.

Microfluidics is ideally suited to the development of a next-generation sputum liquefaction and analysis platform. Microfluidic-based approaches are advantageous for this application due to their automation, biohazard containment, fast reactions, reduced reagent consumption, and low cost of manufacture. Thus far, microfluidic-based approaches for sputum analysis have been developed [91–95]; however, microfluidic based sputum liquefaction has not yet been reported. Developing a microfluidic-based sputum liquefier is challenging because human sputum samples are highly viscous and the Reynolds number in a microfluidic sputum liquefier is extremely low.

In this chapter, we demonstrate for the first time, to the best of our knowledge, the microfluidic liquefaction of human sputum samples. Our approach is built upon an acoustofluidic (*i.e.*, the fusion of acoustics and microfluidics) micromixer that we developed in Chapter 3 [38, 50]. This sharp-edge-based acoustofluidic micromixer realizes rapid, homogeneous mixing of two fluids by exploiting the acoustic streaming effects induced by oscillating sharp-edge structures inside a microfluidic channel [50, 96]. Using this approach, we are able to consistently liquefy human sputum samples without compromising cell viability or sample integrity. Further-

more, as the viscosity of clinical sputum samples can vary between patients with different levels of disease activity, the ability of our device to liquefy sputum samples with a wide range of viscosities is valuable. The controllability and tunability of our acoustofluidic sputum liquefier enables us to liquefy sputum samples of a wide range of viscosities by adjusting the voltage applied to a piezoelectric transducer (PZT). Our acoustofluidic device features advantages such as simplicity of use, automation, low cost and flexibility; these advantages are ideal for the future development of an automated, all-in-one, on-chip sputum processing and analysis device.

4.1.1 Standard liquefaction procedure

The standard procedure for the liquefaction of sputum [97] is comprised of two steps. First, the sputum sample is uniformly mixed with an equal volume of 0.1% dithiothreitol (DTT) (Sputolysin reagent, Cat no. 560000, EMD Millipore, Billerica, MA, USA) using a vortex mixer for 30 seconds and incubated at room temperature for 15 minutes. Next, the sample is filtered through a sterile cell strainer with a 100 μm mesh size (Cat no. 22363549, Fisher Scientific Inc., USA) to isolate a uniform single-cell suspension. Lastly, the liquefied sputum sample is then centrifuged at 1500 rpm for 5 minutes, and the pelleted cells are re-suspended in PBS (Cat no. 10010-049, Life Technologies, NY, USA) or medium such as RPMI 1640 (Cat no. 11875-093, Life Technologies, NY, USA), for further analysis.

4.2 Working concept

Figure 4.1 illustrates the working concept of our acoustofluidic sputum liquefier. Samples of sputum and an equal volume of DTT solution were co-injected into the acoustofluidic device where they mixed uniformly in the presence of an acoustic field. The yield is equivalent to a standard sputum-liquefaction procedure using a vortex mixer. In the standard procedure for sputum liquefaction, a sputum sample is mixed with DTT solution using a vortex mixer for 30 seconds. By comparison, our acoustofluidic liquefaction device is composed of serpentine microchannels with sharp-edge structures, called the "liquefaction region" as diagrammed in Fig. 4.2. By doing so, we repeatedly, uniformly mixed the sputum sample and the sputolysin

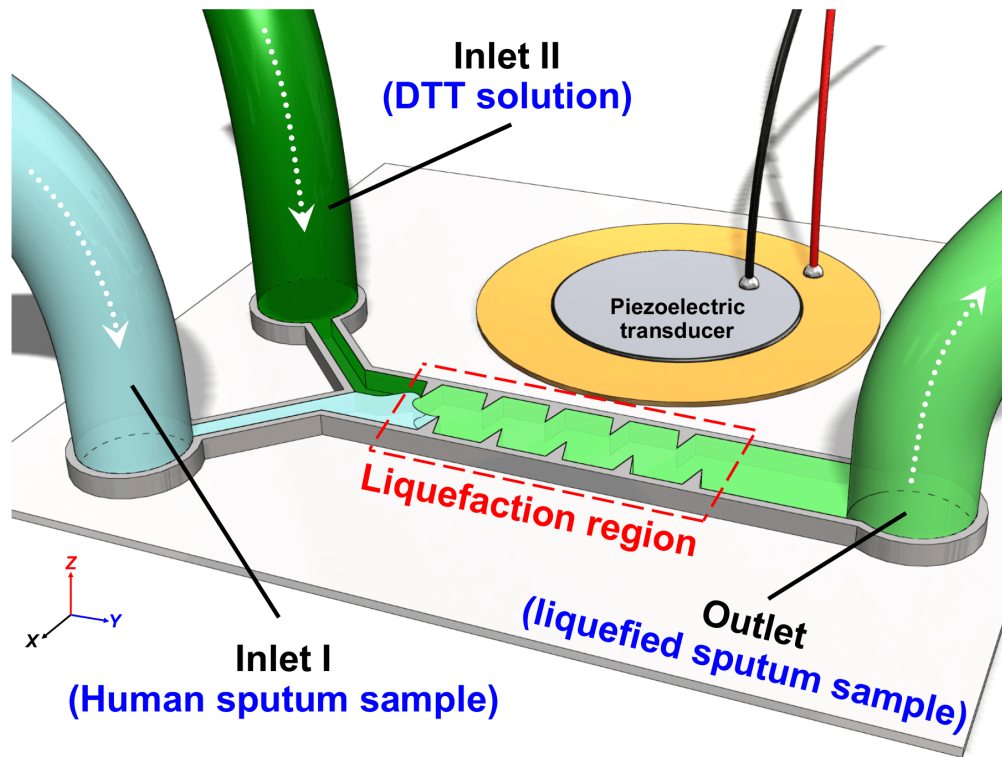


Figure 4.1. (a) Schematic of the acoustofluidic sputum liquefier. Experimental images showing the mixing of fluorescein and DI water when (b) PZT was off: a laminar flow pattern was observed; (c) PZT was on: excellent mixing of two fluids was achieved. (d) Photograph of our acoustofluidic sputum liquefier. (e) Drawing showing the detailed design of our acoustofluidic sputum liquefier. Simulated results showing the Lagrangian mean flow velocity when the fluid is (f) water and (g) a high viscosity fluid (such as sputum) with a viscosity ten times that of the water. Circular streamlines are observed in both cases indicating excellent mixing in both cases.

for as long as 30 seconds.

We were concerned that microchannels might be easily clogged by viscous sputum samples. Therefore, we designed our acoustofluidic device with two parallel sputum-liquefying channels on a single device to prevent the channels from clogging. As a result, even if one of the channels is blocked with sputum, the other will still function. In the standard sputum liquefaction process, sterile cell strainers with a $100\ \mu\text{m}$ mesh size are used to isolate cells from liquefied sputum samples and obtain a uniform single-cell suspension. To perform this filtration step on-chip, instead, a series of parallel, narrow $100\ \mu\text{m}$ wide channels were designed and constructed at a downstream region, named the "filtration region" as diagrammed

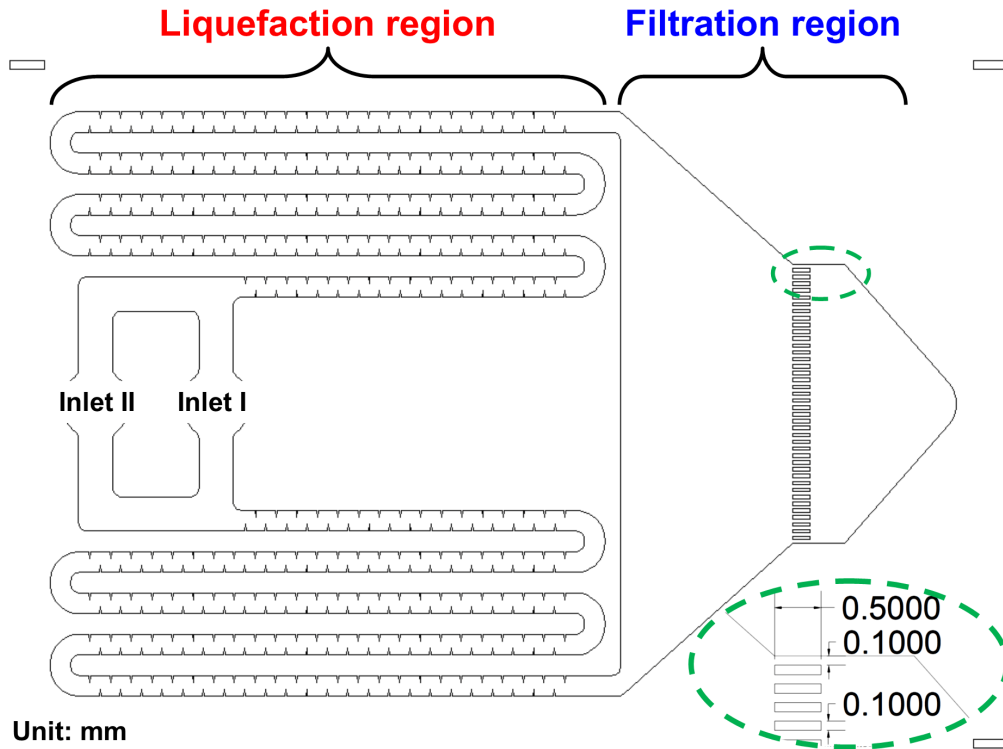


Figure 4.2. Drawing showing the detailed design of our acoustofluidic sputum liquefier.

in Fig. 4.2. These narrow channels not only isolate cells in the liquefied sputum sample, but also prevent the particularly viscous portions of the sputum sample from collecting at the outlet. Additionally, they filter debris from the sputum.

Numerical simulation was also conducted to prove the concept of liquefying high viscous fluids using our acoustofluidic sputum liquefier. Figure 4.3 shows the comparison of mean Lagrangian flow velocity for fluids of different viscosities, simulated with COMSOL (Multiphysics 5.0, COMSOL Inc.) by a numerical method that we reported in Section 2.2.3 [38]. Figure 4.3(a) shows the mean Lagrangian flow velocity for water, while Fig. 4.3(b) shows the velocity for a fluid of viscosity 10 times that of water. Circular streamlines spanning the width of the channel were observed in both cases, indicating good mixing capability. However, the magnitude of mean Lagrangian velocity is found to decrease with increasing viscosity for the same amplitude of vibration, necessitating greater input power for mixing fluids with high viscosity. A similar trend has been reported for bulk acoustic wave devices by Muller *et al.* [42]. Thus, the numerical results shown in Figs. 4.3(a) - (b) confirm the capability of our acoustofluidic device to mix high

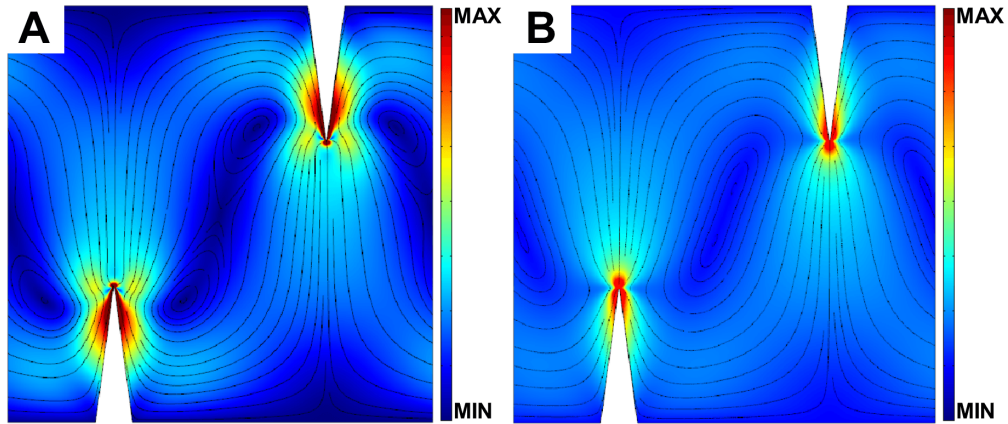


Figure 4.3. Simulated results showing the Lagrangian mean flow velocity when the fluid is (a) water and (b) a high viscosity fluid (*e.g.*, sputum) with a viscosity ten times that of the water. Circular streamlines are observed in both cases, thereby indicating excellent mixing in both cases.

viscosity fluid. High velocities near sharp-edge structures result from the large values of Stokes drift near the sharp-edge structure (Figs. 4.3(a) - (b)); the acoustic streaming speeds in the bulk of the channel are much lower.

4.3 Materials and methods

4.3.1 Device fabrication and operation

Fig. 4.4(a) represents a photograph of our acoustofluidic device for sputum liquefaction. A single-layer PDMS device was bonded to a 150 μm thick glass slide (Cat no. 48404-454, VWR, USA). A piezoelectric transducer (Part no. 81-7BB-27-4L0, Murata Electronics, Japan) was bonded adjacent to the PDMS device on the same glass slide using a thin layer of epoxy (Part no. G14250, DEVCON, MA, USA). The activation of the piezoelectric transducer was controlled by amplified square-wave signals from a function generator (AFG3011C, Tektronix, OR, USA) and an amplifier (25A250A, Amplifier Research, WA, USA). The PDMS device was 100 μm in channel depth, and 600 μm in channel width for those channels in liquefaction region.

The sputum sample and the DTT solution were infused into our acoustofluidic sputum liquefaction device by two separate inlets through two separate 1 mL syringes (McKesson, CA, USA), which were controlled by one automated syringe

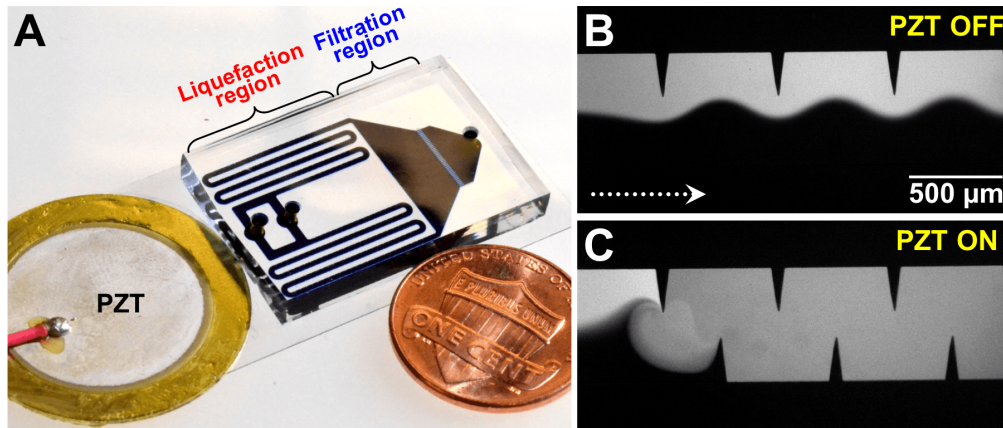


Figure 4.4. (d) Photograph of our acoustofluidic sputum liquefier. Experimental images showing the mixing of fluorescein and DI water when (b) PZT was off: a laminar flow pattern was observed; (c) PZT was on: excellent mixing of two fluids was achieved.

pump (neMESYS, Germany). The liquefied sputum sample was then collected through the outlet to a 1.5 mL centrifuge tube. Every 15 minutes, a 1.5 mL centrifuge tube filled with approximately 500 μL of liquefied sputum sample was replaced by an empty 1.5 mL centrifuge tube, to continue the collection of liquefied samples for further sample characterization and analysis. Before conducting liquefaction experiments with sputum samples, all of our acoustofluidic devices were experimentally tested with DI water and fluorescein to determine the optimized working frequencies of piezoelectric transducer to achieve uniform mixing of these two solutions. Based on these tests, 5.50 kHz was determined to be the working frequency for all our liquefaction devices; all the liquefaction experiments were conducted at this frequency. Detailed procedures to determine the optimized working frequency for the piezoelectric transducer are described in Section 4.3.2. And as an example of mixing two different solutions, Fig. 4.4(b) shows an unmixed laminar flow of two different solutions (DI water and fluorescein) when a piezoelectric transducer was inactivated, whereas Fig. 4.4(c) shows uniform mixing of the two solutions when the piezoelectric transducer was activated. Mixing performance of the two solutions at different regions in the channel is characterized and discussed in Section 4.3.3.

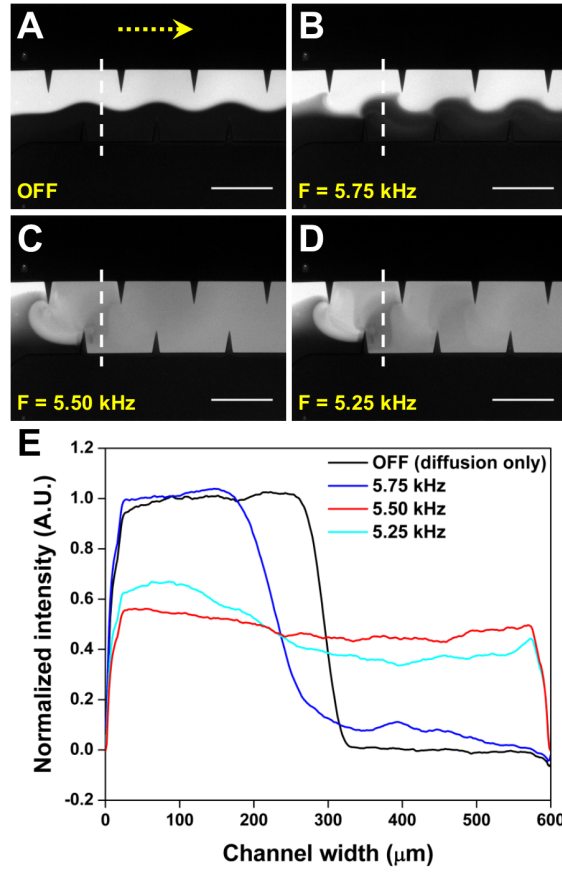


Figure 4.5. Characterization of the mixing performance at the beginning of the channel under different driving frequencies of the PZT. (a) A side-by-side laminar flow pattern was observed when the piezoelectric transducer was switched off. (b) 5.75 kHz: Incomplete mixing due to weaker acoustic streaming effect. (c) 5.50 kHz: Uniform mixing was observed. (d) 5.25 kHz: Excellent mixing was achieved, but not as complete as that obtained using 5.50 kHz. (e) Plots of normalized fluorescent intensity across the width of channel. The normalized intensity profiles were characterized along the dashed white lines in the figure. Scale bar: $500 \mu\text{m}$

4.3.2 Determination of device working frequency

To determine the optimized the working frequency for the piezoelectric transducer before conducting liquefaction experiments, we swept the frequency with a 50 Hz increment from 1 kHz to 100 kHz to monitor and characterize the mixing performance at different frequencies. From the experimental results, we found that there were some frequencies at which mixing (incomplete or complete) of the two solutions were observed. Figure 4.5 shows the mixing performance at the beginning of the channel when our device was tested with different input frequencies.

The results suggest that when tested with the frequency of 5.50 kHz, our device achieved complete mixing with a uniform intensity profile, suggesting that 5.50 kHz may be the optimum working frequency for our sputum liquefier. To be more accurate, we further verify the mixing performance by calculating mixing index for each case. The mixing index was calculated using Equation 3.1. A mixing index of 0.5 represents completely unmixed fluids (*i.e.*, distinct laminar flow), while a mixing index of 0.0 stands for completely mixed fluids. In this work, we chose a mixing index below 0.1 as acceptable mixing. The mixing indices were calculated to be 0.433, 0.047, and 0.118 for mixing performance obtained, respectively, using the frequency of 5.75 kHz, 5.50 kHz, and 5.25 kHz. The results, once again, suggest that 5.50 kHz is the optimized working frequency for our acoustofluidic micromixer to uniformly mix two solutions.

4.3.3 Mixing performance inside the channel

Two different solutions, undoubtedly, can be mixed well enough solely based on diffusion (*i.e.*, passive mixing) over the long winding channel, which, however, takes place only if a relatively low flow rate is adopted. In this work, to actively liquefy the sputum samples, while maintaining a reasonable throughput, a flow rate of 15 $\mu\text{L}/\text{min}$ was used for both the sputum samples and DTT solution, resulting in a total flow rate of 30 $\mu\text{L}/\text{min}$ in the channel. Using DI water and fluorescein (DI water containing FITC-dextran) as a demonstration of mixing performance, we were able to examine under a flow rate of 30 $\mu\text{L}/\text{min}$, whether such a long channel can result in a complete, uniform mixing of the two solutions solely based on diffusion. As shown in Fig. 4.6, the mixing performance at different regions, including the beginning, middle, and end of the channel, was characterized in terms of fluorescence intensity. It is clear that when the piezoelectric transducer was switched OFF, only an incomplete, partial mixing of the solutions due to diffusion was observed under the flow rate condition. By contrast, once the piezoelectric transducer was switched ON, a complete, uniform mixing of the solutions was achieved throughout the channel, demonstrating the advantage of the active mixing of our acoustofluidic micromixer. Given the flow rate condition and the solution (DI water) we used, the Reynold's number was estimated to be roughly 800. Although it is higher than that in a typical microfluidic device, it still falls into the laminar

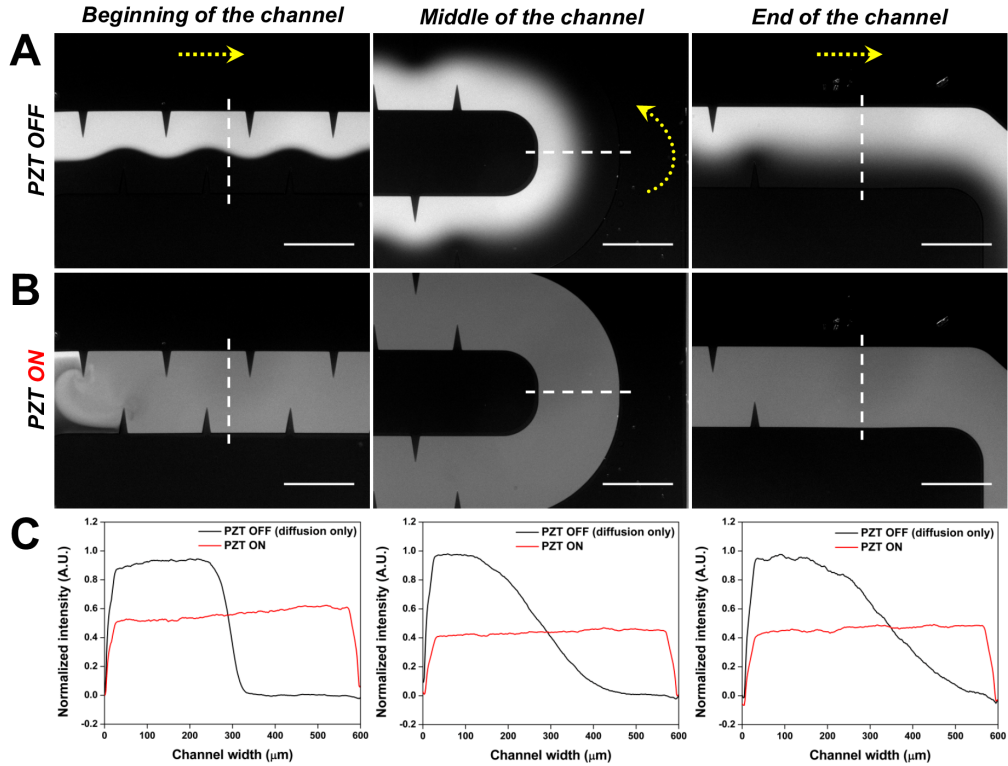


Figure 4.6. Characterization of the mixing performance at different regions under a total flow rate of $30 \mu\text{L}/\text{min}$. (a) When the PZT was switched off: A side-by-side laminar flow pattern was first observed in the beginning of the long channel; partial, incomplete mixing due to diffusion was then observed at the middle and the end of the channel. (b) When the PZT was switched ON: Uniform, complete mixing was observed throughout the channel. (c) Plots of corresponding normalized fluorescent intensity across the width of channel at different regions. The normalized intensity profiles were characterized along the dashed white lines in the figure. Scale bar: $500 \mu\text{m}$

flow regime. For the case of human clinical sputum samples, the precise calculation of Reynold's number is more challenging because the viscosity of sputum varies across a wide range ($10^3 - 10^6$ times the viscosity of water) [98], depending on the patient status. Besides, no data is provided on the density of the sputum in the literature. Considering the extremely high viscosity of clinical human sputum samples, a longer mixing channel incorporating with active acoustic mixing mechanism is believed to be beneficial for processing human sputum samples.

4.3.4 Human sputum samples

To establish reproducibility in this initial work, we analyzed four separate sputum samples from a single asthmatic patient using our acoustofluidic device. The sputum samples were collected at the National Institute of Health (NIH) once a week from a patient who had provided informed consent to participate in protocol 99-H-0076. After collection, sputum samples were placed on ice and immediately transported from NIH to our lab at The Pennsylvania State University, for liquefaction experiments performed on the same day. Due to the time for transportation and experimental set-up, the sputum samples were typically processed after an interval of approximately 8 hours. Upon arrival at our lab, each sample was divided into two portions of roughly equal volume. One portion was liquefied using our acoustofluidic device, and the other was liquefied using a vortex mixer. Both liquefied portions were further divided into three aliquots for characterization, which included cell viability, modified Wright-Giemsa staining, and flow cytometry analysis.

4.3.5 Cell Viability

Cell viability was assessed to evaluate the biocompatibility of our liquefaction device for processing clinical human samples. Cells from sputum samples liquefied using our acoustofluidic micromixer (experimental group) were stained with the cell-permeant dye, Calcein-AM (Life Technologies, NY, USA), to determine the number of live cells, and propidium iodide (Sigma-Aldrich, MO, USA), to identify dead cells. As a control group, cell viability was also assessed for sputum samples that were liquefied using a vortex mixer. For both the experimental and control groups, four independent experiments were performed.

4.3.6 Modified Wright-Giemsa staining

A thin layer of sputum cells was prepared by centrifugation using a CytospinTM 3 cytocentrifuge (Thermo Scientific, USA) at 600 rpm for 10 minutes and then allowed to air-dry before modified Wright-Giemsa staining. The slides were stained with a commercial staining kit (ShandonTM Kwik-DiffTM, Thermo Scientific, USA) as follows: (1) 25 seconds in fixative solution (green); (2) 30 seconds in solution I

(red); (3) 30 seconds in solution II (blue); (4) rinse the slides with DI water. After staining, the cytospin slides were examined under an inverted microscope (Eclipse Ti, Nikon, Japan) with a $100\times$ objective lens, and images were captured using a digital camera (D3s, Nikon, Japan).

4.3.7 Statistical analysis

Data were presented as group mean \pm standard deviation (SD), and were analyzed by student's t -test using Prism 6.0 (GraphPad Software Inc., CA, USA). A p -value of less than 0.05 was considered statistically significant.

4.4 Results and discussion

4.4.1 Visual comparison

In Section 4.3.2, the raw sputum sample and the DTT solution were each injected into the channel at a flow rate of $15\ \mu\text{L}/\text{min}$, yielding a liquefaction throughput of $30\ \mu\text{L}/\text{min}$. Upon the activation of a piezoelectric transducer with an input voltage of $40\ V_{PP}$, the sputum samples and the DTT solution were repeatedly and uniformly mixed for a sufficient amount of time (30 seconds). The uniform, liquefied mixture of sputum and DTT solution was collected over a 15 minutes interval to a 1.5 mL centrifuge tube through the outlet. Concurrently, we manually liquefied the same sputum sample using a vortex mixer (MINI 230 V, VWR, USA) followed by 15 minutes of incubation. Next, we visually compared the difference in appearance between non-liquefied samples (*i.e.*, the raw sputum sample), and liquefied sputum samples. In Fig. 4.2, R, V and A denote, respectively, the non-liquefied sputum sample, the sputum sample liquefied using a vortex mixer, and the sputum sample liquefied using our acoustofluidic device. As shown in Fig. 4.7, the non-liquefied sputum sample was cloudy and contained visible clumps of mucus. The liquefied sputum samples, however, were translucent, presenting as a uniform mixture with a negligible amount of viscous mucus sputum.

It is encouraging that the sputum sample liquefied using our acoustofluidic device appeared similar to those liquefied using a vortex mixer, as they demonstrate that on-chip liquefaction may be achieved with our acoustofluidic approach.

Though the four sputum samples used in this work were all provided by the same asthmatic patient, the viscosity varied among the samples, which were collected on different days. In four independent liquefaction experiments, all samples were uniformly liquefied, appearing similar to those shown in Fig. 4.7. These results demonstrate that our acoustofluidic liquefaction device can liquefy sputum samples over a range of viscosities. We observed that when a volume of sputum was mixed with a greater volume of DTT solution, liquefaction was more uniform; however, this higher volume of DTT solution may affect the cell viability and further cellular analysis [99,100]. As a result, the volume of DTT solution must be considered when liquefying the sputum samples for downstream analyses.

In this work, in fact, we also conducted some preliminary experiments in which we attempted to use cell strainers (100 μm mesh size) to filter un-liquefied, raw sputum samples. However, the extremely high viscosity of the sputum prevented any portion of the sample from passing through the cell strainer. Instead, the sputum samples were all clogged inside the cell strainers. When injected along with DTT solution into the channel with the PZT switched off, similarly, the raw sputum samples could not pass through the on-chip filtration region (100 μm in channel width). Therefore, we were not able to collect anything but the DTT solution at the outlet. Moreover, after the clogging of the sputum samples in the filtration region, our device would soon start leaking because of an accumulating high-pressure resistance inside the channel. As a result, we cannot provide an image showing sputum samples that were run through our device with the PZT switched off, because experimentally we were unable to carry it out.

4.4.2 Viability of cells in liquefied sputum samples

As shown in Fig. 4.8(a) - (d), both dead and live cells were observed in sputum samples liquefied using both the vortex mixer and our acoustofluidic device. After counting the number of live and dead cells, we were able to statistically compare the viability obtained after each approach. There were over 1500 cells considered for both of the groups. As shown in Fig. 4.8(e), the viabilities were calculated to be $41.5 \pm 17.7\%$ and $36.7 \pm 8.9\%$ for the sputum samples liquefied, respectively, using the vortex mixer and our micromixer. The results are statistically similar, with a p -value of 0.692 ($p > 0.05$). In other words, our acoustofluidic device preserves cell

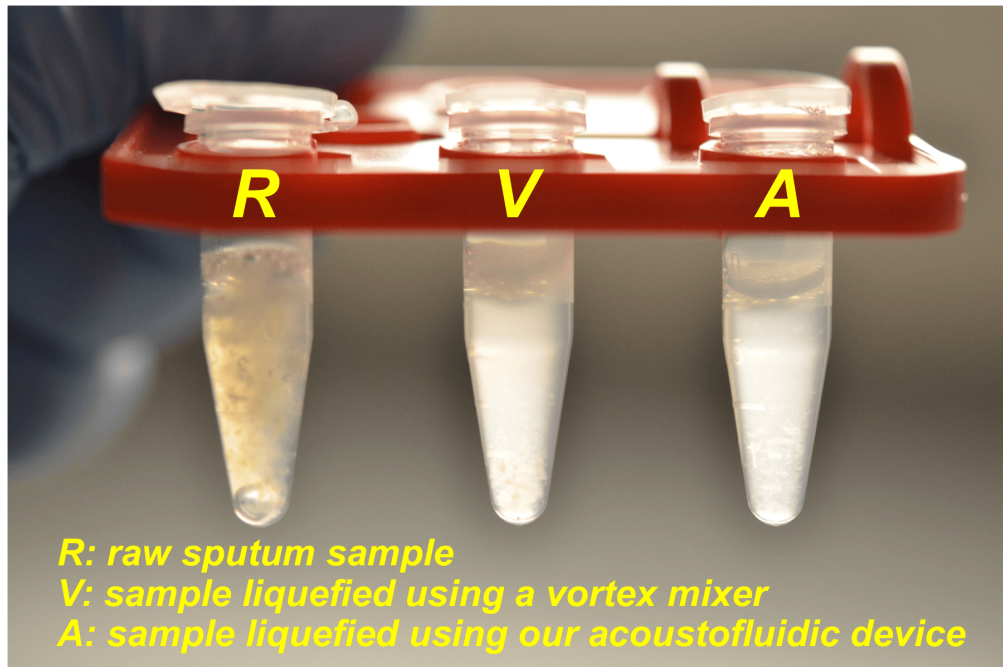


Figure 4.7. Photograph showing the visual comparison of human sputum samples: (R) an un-liquefied raw sputum sample; (V) a sputum sample liquefied using a vortex mixer; (A) a sputum sample liquefied using our acoustofluidic device.

viability similar to a vortex mixer, demonstrating that our acoustofluidic device is biocompatible with clinical samples. The relatively low cell viability in these two samples may stem from the sample transportation and storage. In this work, the human sputum samples were transported from NIH (Bethesda, Maryland, USA) to our lab at The Pennsylvania State University (State College, Pennsylvania, USA) on the same day they were liquefied. Each sputum sample prior to experimentation was stored on ice for at least 8 hours during transportation & setup. A cell viability in the 60% range is typically observed when sputum samples are processed right after collection without transportation. As such, cell viability will likely be improved when samples are analyzed at a single site.

4.4.3 Cells morphology and identification of immune cells

To verify if immune cells present in liquefied sputum samples can be preserved and recovered, modified Wright-Giemsa staining was used to inspect cellular morphology and identify inflammatory cell types. Figures 4.9(a) - (c) and Figs. 4.9(d) - (f) are stained cells from the sputum samples liquefied, respectively, using the vortex

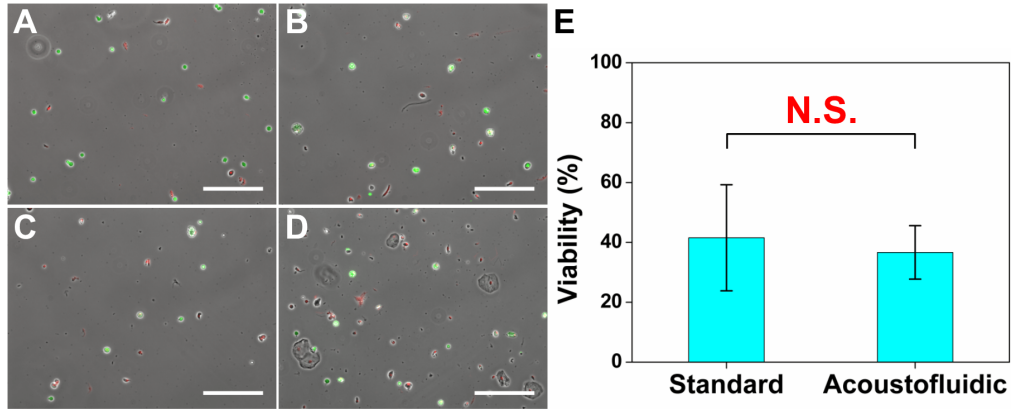


Figure 4.8. Cell viability of sputum samples liquefied using: (a) - (b) a standard sputum-liquefaction procedure; (c) - (d) our acoustofluidic sputum liquefier. (e) Statistical analysis showing the comparison of cell viability of two liquefaction procedures. Data represent an average of $n = 3$ to 4 independent experiments per group. In each independent experiment, over 500 cells were counted to assess cell viability. N.S. represents groups that are not statistically different ($p > 0.05$). Data are presented as group means \pm standard deviation (SD). Scale bar: 200 μm .

mixer and the acoustofluidic sputum liquefier. In Fig. 4.9(a) - (c), inflammatory cells, such as eosinophils (yellow arrows) and neutrophils (red arrows), which are commonly present in sputum samples from asthmatic patients, were recovered intact after liquefaction using the vortex mixer. As shown in Fig. 4.9(d) - (f), intact eosinophils and neutrophils were also seen in sputum samples liquefied using our acoustofluidic device. In addition to eosinophils and neutrophils, macrophages and lymphocytes were also present in samples liquefied using either the vortex mixer or our acoustofluidic device. The modified Wright–Giemsa staining results demonstrate that our device uniformly liquefies clinical sputum samples, without sacrificing cellular integrity. We further quantified the cell content of induced sputum samples liquefied using a standard vortex mixer and our sputum liquefier (*i.e.*, acoustofluidic micromixer). As shown in Fig. 4.10, the percentage of each common type of cells, including eosinophils, neutrophils, macrophages and lymphocytes, between two approaches appear similar and are comparable. This result, once again, suggests that our acoustofluidic sputum liquefier could uniformly liquefy sputum samples to recover those inflammatory cells of interest.

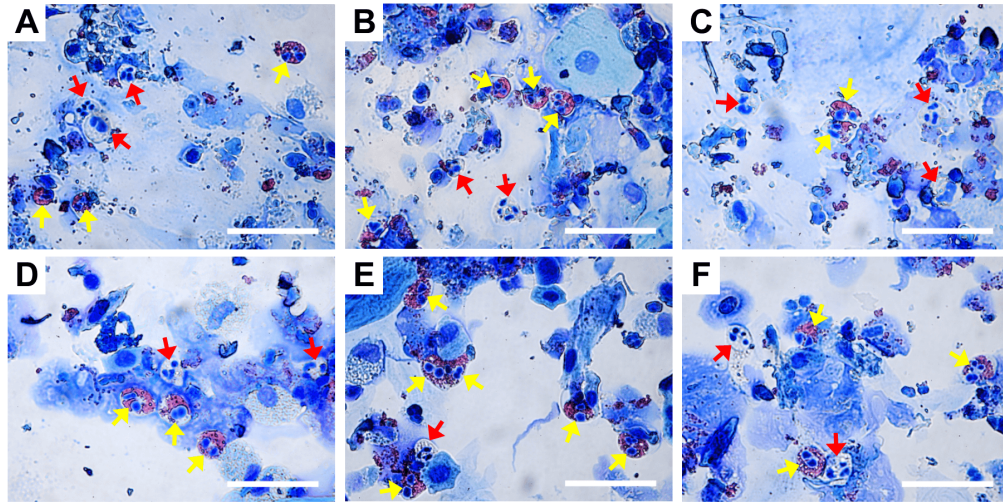


Figure 4.9. Representative of optical images (100 \times) showing modified Wright–Giemsa staining results of cell samples obtained from sputum samples liquefied using (a) - (c) a vortex mixer or (d) - (f) our acoustofluidic sputum liquefier. Inflammatory cells, such as eosinophils (yellow) and neutrophils (red), are indicated by colored arrows. Scale bar: 50 μm .

4.4.4 Flow cytometry analysis

Flow cytometry was next performed to quantitatively characterize the liquefied sputum samples and evaluate the performance of our acoustofluidic sputum liquefier. A commercial bench-top flow cytometer (FC 500, Beckman Coulter, USA) was used to conduct the flow cytometry analysis. Cells in liquefied sputum samples were stained with Alexa Fluor 488-labelled anti-human CD45 antibody (Biolegend, CA, USA) to identify leukocytes, and PE-labelled CD15 antibody (Biolegend, CA, USA) to identify both eosinophils and neutrophils, which are common inflammatory cells present in sputum from asthmatic subjects (Fig. 4.11). The percentage of CD45+/CD15+ eosinophils and neutrophils were 20.4% and 24.9%, respectively, for samples that were liquefied using the vortex mixer and our acoustofluidic device. These results show that key inflammatory cells in sputum may be recovered and identified, which thereby demonstrates that our acoustofluidic device is an effective tool for the clinical liquefaction of human sputum.

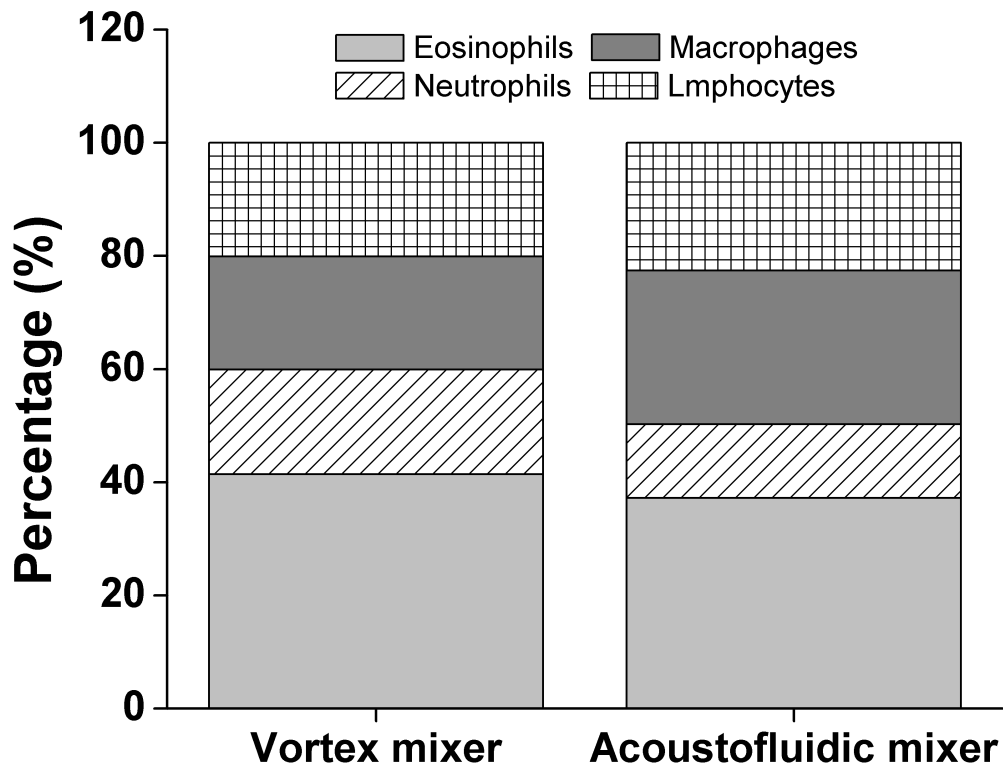


Figure 4.10. Quantification of cell content of induced sputum samples liquefied using a standard vortex mixer and our sputum liquefier (*i.e.*, acoustofluidic micromixer).

4.5 Summary

Using a sharp-edge-based acoustofluidic micromixer, we have demonstrated the first microfluidic-based sputum liquefaction of human sputum. Furthermore, we show that sputum samples liquefied using our acoustofluidic device were comparable to samples that were liquefied using a vortex mixer based on analyses of cell viability, modified Wright-Giesma staining and flow cytometry. Our results reveal the potential of our acoustofluidic device for liquefying clinical sputum samples on-chip. Our device can liquefy sputum samples at a throughput of $30 \mu\text{L}/\text{min}$, a value that will be improved with further design optimization. When integrated with our sharp-edge-based acoustofluidic micropump [96], our acoustofluidic sputum liquefier will be able to liquefy sputum samples in an automated fashion. Compared to the standard approach for sputum liquefaction, the acoustofluidic approach is advantageous not only in cost, simplicity, and automation, but also in

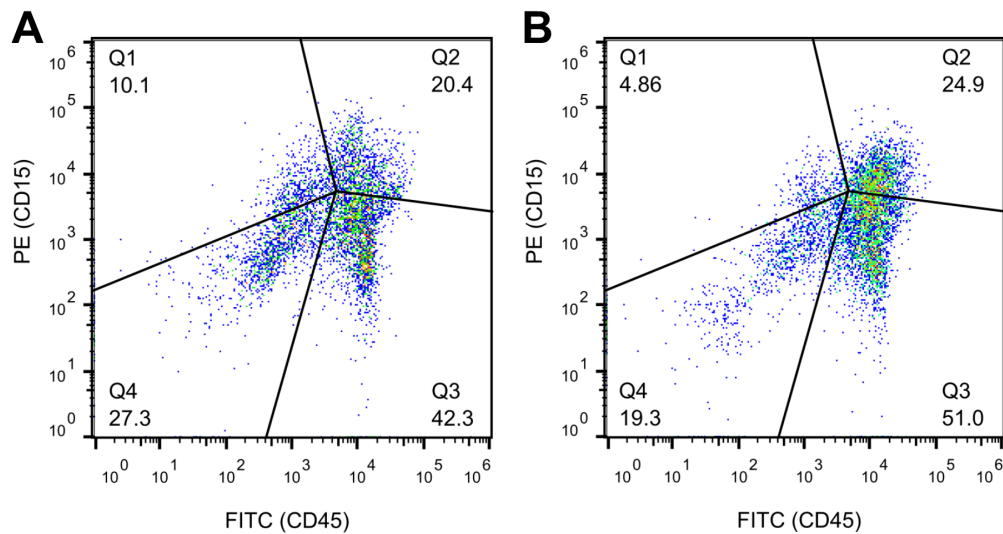


Figure 4.11. Fluorescence (CD45) vs. fluorescence (CD15) plot of the cell samples obtained from the sputum samples liquefied by (a) a standard sputum-liquefaction procedure and by (b) our acoustofluidic sputum liquefier. The percentage of co-population of eosinophils and neutrophils are 20.4% and 24.9% for (a) and (b), respectively.

flexibility and integrability.

Together, our findings suggest that our sharp-edge-based acoustofluidic sputum liquefier is a promising candidate for incorporation with other on-chip components that will enable the development of a fully integrated, self-contained sputum processing and analysis platform. Moreover, our demonstration of liquefying sputum samples opens the gate for applications that require the processing of highly viscous fluids.

Sharp-edge-based acoustofluidic chemical gradient generator

In Chapter 3, we have demonstrated the capability of our acoustofluidic micromixer for rapid and homogeneous fluid mixing, and by extending its capability, we have demonstrated the mixing of highly-viscous fluid samples (*i.e.*, clinical human sputum samples in this dissertation work) in Chapter 4. By further engineering the acoustic streaming patterns, in this chapter we demonstrate an acoustofluidic gradient generator based on acoustically oscillating sharp-edge structures, which facilitates in a step-wise fashion the rapid mixing of fluids to generate tunable, dynamic chemical gradients. The ability to generate stable, spatiotemporally controllable concentration gradients is critical for resolving the dynamics of cellular response to a chemical microenvironment. In this work, by controlling the driving voltage of a piezoelectric transducer, we demonstrated that the chemical gradient profiles can be conveniently altered (spatially controllable). By adjusting the actuation time of the piezoelectric transducer, moreover, we generated pulsatile chemical gradients (temporally controllable). With these two characteristics combined, we have developed a spatiotemporally controllable gradient generator. The applicability and biocompatibility of our acoustofluidic gradient generator are validated by demonstrating the migration of human dermal microvascular endothelial cells (HMVEC-d) in response to a generated vascular endothelial growth factor (VEGF) gradient, and by preserving the viability of HMVEC-d cells after long-term exposure to an acoustic field. Our device features advantages such as simple fabrication

and operation, compact and biocompatible device, and generation of spatiotemporally tunable gradients. The work presented in this chapter has been reported in The 17th International Conference on Miniaturized Systems for Chemistry and Life Sciences (MicroTAS 2013), published in *Journal of Lab on a Chip* [101] and selected as a ***Lab on a Chip HOT Article*** of 2015.

5.1 Motivation

The spatial and temporal dynamics of biomolecule gradients are essential in many biological processes [102–106]. It has been reported that cells respond differently to spatial and temporal characteristics of chemical stimuli, which in turn influences cell signalling [107, 108], migration [109–113], differentiation [114–116], and metastasis [117, 118]. Conventional gradient-generation platforms such as the Boyden chamber and derivatives [119–121] as well as micropipette [122, 123] have been adopted because of their simplicity of fabrication and ease of use. These platforms, however, are limited to generating only static, monotonic gradients without tunable spatiotemporal characteristics (*e.g.*, magnitude, frequency, slope, and temporal and spatial resolution).

To explore the effect of the time and space dynamics of gradients on cellular responses, microfluidic platforms have been advanced to generate chemical gradients with spatiotemporal control, including Christmas-tree-like channel networks [124, 125], microjet arrays [126, 127], and source-sink configuration [128, 129]. Most of these microfluidic-based gradient generators still employ passive means, either passive mixing [130, 131] or free-diffusion [132–134], making these approaches difficult to generate gradients with high spatiotemporal resolution. In contrast to passive generation of concentration gradients, actively generating concentration gradients offers compelling controllability and flexibility. One can envision a microfluidic-based device that can — by active and controllable means, “active mixing” — generate concentration gradients of biomolecules of interest with highly controllable specific spatiotemporal characteristics.

Recently, active generation of gradients has been demonstrated using acoustofluidic platforms; two of the most intriguing examples are focused travelling surface acoustic waves (F-TSAW) [135] and acoustically oscillating microbubbles [83]. Though the F-TSAW based platform generated gradients that can be rapidly

switched on and off and the resulting gradient profiles can be easily adjusted, it is limited to generating only monotonic (mono-directional) gradients, and its applicability and biocompatibility are yet unproven for biological studies. The oscillating microbubbles-based platform, likewise, can generate spatiotemporally tunable gradients. However, the instability of microbubbles over time [14, 26] and the size-/temperature-dependent operation of the platform make it unsuitable for biological applications where long-term cell culture is often needed, thereby limiting the versatility of this approach.

In this chapter, we demonstrate an active, spatiotemporally controllable chemical gradient generator via an acoustofluidic [3, 37, 42, 136, 137] (*i.e.*, the fusion of acoustics and microfluidics) strategy. This work is built primarily upon our previously reported acoustic streaming effect induced by oscillating sharp-edge structures [38, 50, 86, 96]. We have shown that the sidewall sharp-edge-based micromixer [50] is capable of rapidly mixing fluids in microscale on-demand. In spite of these features, the sidewall sharp-edge-based micromixer we demonstrated previously [50] can only yield mixtures of constant concentrations. In order to achieve the generation of concentration gradients, in this work we employ multiple sharp-edge structures to form multiple mixing sites at once. In addition, instead of attaching the sharp-edge structures to the sidewall of the channel, as we demonstrated previously [38, 50, 86, 96], we arrange the sharp-edge structures in the middle of the channel in a ladder-like arrangement.

By taking advantage of these newly designed device features, we can mix two different solutions in a step-wise fashion and thus, obtain different mixtures of serially diluted concentrations simultaneously in the channel; in other words, we can serially dilute the mixture of two different solutions to establish a concentration gradient. Furthermore, once various flow rate combinations of two solutions are introduced to the device, we can, accordingly, mix two solutions in various ratios, resulting in various gradient profiles. Using this sharp-edge-based acoustofluidic gradient generator, one can generate a concentration gradient that is not only spatiotemporally stable, but also spatiotemporally controllable. Spatiotemporal control over gradient profiles can be easily achieved by adjusting the input signal of a piezoelectric transducer (frequency, voltages, and actuation time). Compared to existing microfluidic-based gradient generators [83, 135], our sharp-edge-based acoustofluidic gradient generator features distinct characteristics such

as stability, controllability, flexibility, reliability, simplicity, and temporal response. Our platform is a promising candidate for a wide variety of biological studies where the spatiotemporal dynamics of gradients is highly relevant.

5.2 Concept and device design

Fig. 5.1(a) illustrates the design and concept of our acoustofluidic device for the generation of chemical gradients. The device is simple: a single-layer polydimethylsiloxane (PDMS) channel accommodating multiple sharp-edge structures inside the channel and a piezoelectric transducer. Fluids of different compositions or concentrations — for this example, phosphate buffered saline (PBS) and PBS containing fluorescein isothiocyanate-dextran (FITC-dextran) — are simultaneously injected into the channel through two separate inlets. Before the piezoelectric transducer was activated, a side-by-side laminar flow of PBS and FITC-dextran was observed. Once the piezoelectric transducer was activated, the sharp-edge structures were acoustically oscillated and thereby generated acoustic streaming effect around the tip of each sharp-edge structure (Fig. 5.1(b)). The induced acoustic streaming effect in turn mixed PBS and FITC-dextran in a step-wise fashion because of the ladder-like arrangement of sharp-edge structures. The step-wise mixing established a concentration gradient of FITC-dextran which was perpendicular to the direction of fluid flow, *i.e.*, along the direction of channel width (dotted line in Fig. 5.1(a)).

Fig. 5.1(b) illustrates an acoustic streaming pattern around the tip of a sharp-edge structure, as well as the mixing of different solutions due to the resulting acoustic streaming effect. Each sharp-edge structure constructed inside the channel was of identical dimension to ensure that all sharp-edge structures would be acoustically excited at a single driving frequency from the piezoelectric transducer; in other words, it was to ensure that the acoustic streaming effect induced by each oscillating sharp-edge structure was identical in terms of strength. In order to eliminate undesired acoustic streaming effect, the sharp-edge structure was designed to be teardrop-like, based upon a triangular structure of $100\ \mu\text{m}$ in width and $400\ \mu\text{m}$ in length. Once it was acoustically oscillated by the actuation of the piezoelectric transducer, the oscillating sharp-edge structure generated an acoustic streaming effect around its tip: mass transport across the channel width was enhanced (*i.e.*,

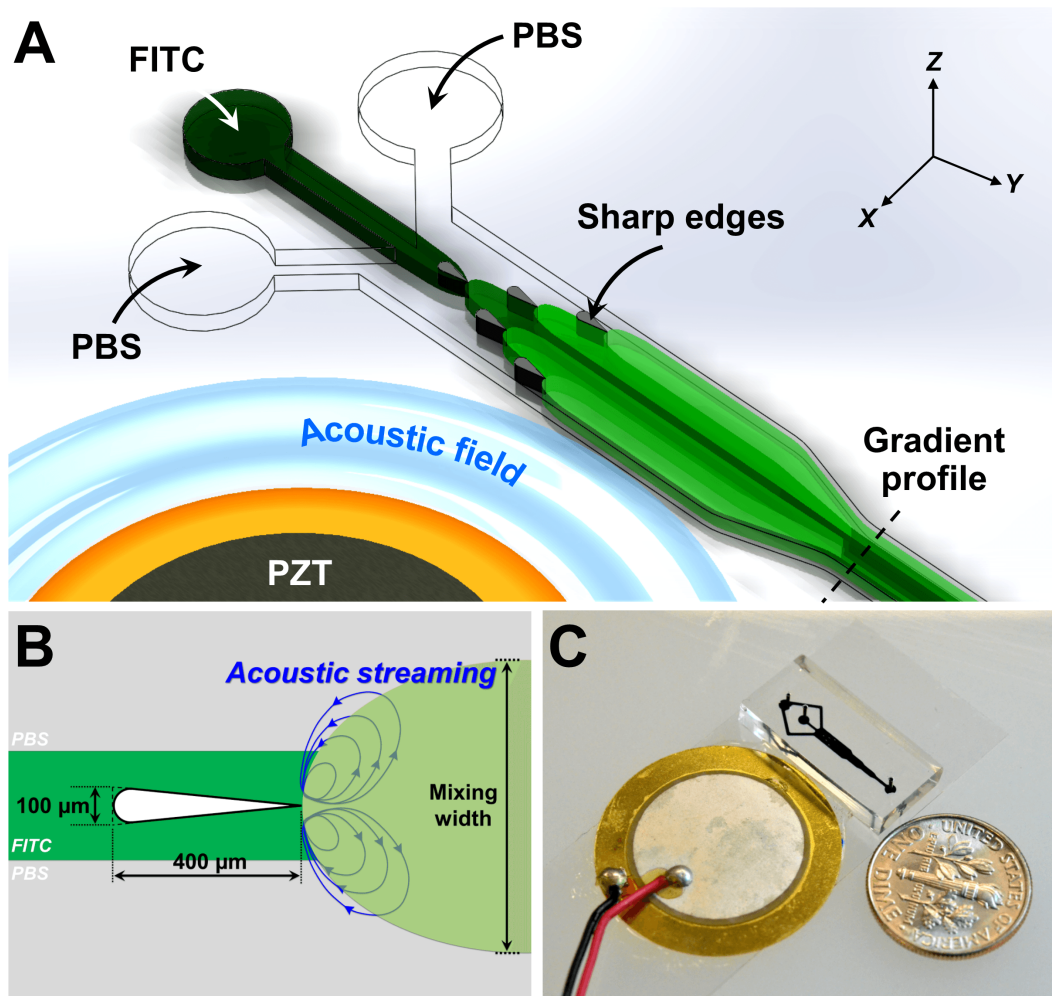


Figure 5.1. (a) Schematic of the sharp-edge-based acoustofluidic chemical gradient generator. (b) Schematic of the sharp-edge structure within our device. (c) Optical image of the sharp-edge-based acoustofluidic chemical gradient generator.

different fluids were mixed by breaking the interface of laminar fluids). The mixing width was defined as the width over which the generated acoustic streaming effect spanned across the channel; in other words, the mixing width can be an index of the strength of generated acoustic streaming effect. A lesser "mixing width" allowed the FITC-dextran to mix with a small amount of PBS, gently diluting the FITC-dextran. A greater mixing width, by contrast, allowed the FITC-dextran to mix with a significant amount of PBS, greatly diluting the FITC-dextran. Given that the mixing width was proportional to the strength of the acoustic streaming effect and the strength was controllable by varying the driving voltage of the

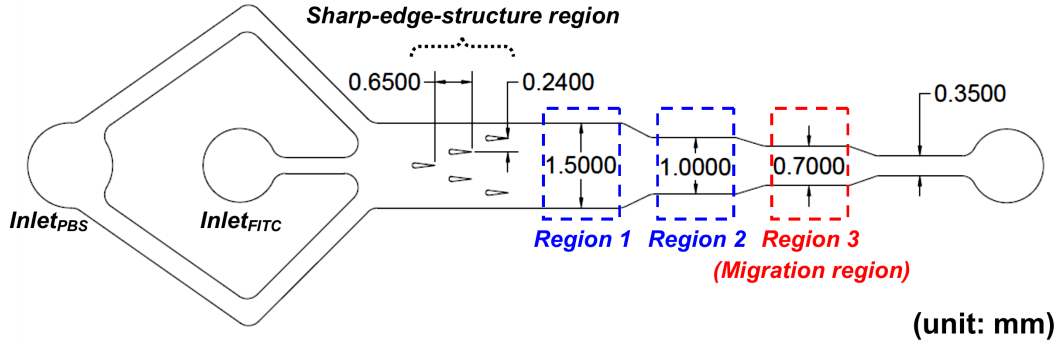


Figure 5.2. Design of the sharp-edge-based acoustofluidic gradient generator. To demonstrate controllable spatial resolution of generated chemical gradients, the downstream region of the device is divided into three regions: region 1, region 2, and region 3.

piezoelectric transducer, we adjusted the mixing width by controlling the driving voltage. We were able to alter the concentration of the resulting mixture by changing the driving voltage of the piezoelectric transducer.

It is also worth mentioning that when compared to F-TSAW-based devices and oscillating bubble-based devices, our sharp-edge-based gradient generator does need slightly higher input power to work, which in large part, is because the sharp-edge structure is of harder material when compared to soft bubble membrane, and as such, more power (energy) is required to oscillate the solid sharp-edge structure. Nevertheless, we are confident that the required input power can be further lowered by optimizing the device material, device design, and coupling efficiency between the piezoelectric transducer and the device, and this optimization work is ongoing. Regardless of input power, our sharp-edge-based gradient generation possesses advantages such as simplicity, stability, controllability, and flexibility. Simplicity, for example, can allow us to prepare devices without sophisticated fabrication process for electrodes, when compared to SAW-based devices. Our device has remarkable stability and reliability. Collectively, though our proposed devices may require slightly higher input power, which very likely can be further reduced by optimizing the devices, our devices can be simply fabricated and operated with performance comparable to already reported devices (*e.g.*, F-TSAW-based and oscillating-bubble-based gradient generators).

5.3 Materials and methods

5.3.1 Experiment setup and operation

Fig. 5.1(c) is a photograph showing our acoustofluidic device for generating concentration gradients. The preparation of our device is simple and of one-layer fabrication. In short, a single-layer PDMS device was first prepared using soft lithography and the mold-replica technique. Afterward, the single-layer PDMS channel was bonded onto a glass slide of $150\ \mu\text{m}$ thickness (Cat. no. 48404-454, VWR, USA) after a plasma surface-treatment for 60 seconds (BD-10AS, Electro-Technic Products, IL, USA), followed by bonding a piezoelectric transducer (Model no. 273-073, RadioShack, USA) adjacent to the PDMS device on the same glass slide with a thin layer of epoxy (Part no. 84101, Permatex, CT, USA). The actuation of the piezoelectric transducer, including ON/OFF switching, driving frequency and voltage, and actuation time, was controlled by a function generator (AFG3011C, Tektronix, USA) and an amplifier (25A250A, Amplifier Research, USA).

Fig. 5.2 shows the detailed channel design of our device. The channel depth was $100\ \mu\text{m}$ throughout the channel. To show the spatial distribution of concentration gradient, the channel downstream from the sharp-edge-structure region was designed to accommodate multiple regions of various channel widths: region 1 ($1500\ \mu\text{m}$), region 2 ($1000\ \mu\text{m}$), and region 3 ($700\ \mu\text{m}$). Region 3, here called the "migration region", was particularly designed to be $700\ \mu\text{m}$ wide for the demonstration of cell migration experiment with our device. On one hand, the widths of regions 1, 2 and 3 were chosen primarily based on the size of viewable region of the CCD on our microscope when using different objective lenses. For example, when a 10X objective is used, the width of region 3 ($0.7\ \text{mm}$) fits right in the viewable region of the CCD. On the other hand, designing the downstream regions with various widths would also enable us to demonstrate that the spatial resolution of concentration gradients generated using our device can also be altered by simply adjusting the channel width. In other words, the width of the channel can also define the width of the gradient profiles generated. The sharp-edge structures were $650\ \mu\text{m}$ and $240\ \mu\text{m}$ apart, respectively, along the direction of channel width (x -direction) and length (y -direction). The arrangement of sharp-edge structures, as shown in Fig. 5.1(d), is optimized primarily based on the mixing width (*i.e.*, the

width of one paired streaming-pattern) that one sharp-edge structure can generate when acoustically oscillated. Nevertheless, it is worth mentioning that by changing the arrangement of sharp-edge structures, the concentration gradient profiles might be altered accordingly.

To characterize the generated concentration gradients, phosphate buffered saline ($1\times$ PBS, Life Technology, CA, USA) and PBS containing FITC-dextran (1 mg/mL; MW = 10 kDa, Sigma-Aldrich, MO, USA) were pumped into the channel through two distinct inlets. The injection of these two solutions was performed using two separate 1 mL syringes (BD Bioscience, NJ, USA), which were independently controlled by an automated syringe pump (neMESYS, Germany).

All of the experiments were conducted on the stage of an inverted microscope (TE2000-U, Nikon, Japan) that was equipped with a cell incubation system (Chamlide TC, Live Cell Instrument, South Korea). The cell incubation system provides a humidified environment at 37 °C with a CO₂ level of 5% for on-chip cell culture. All the experimental images and videos were captured using Nikon NIS-Elements Advanced Research (AR) software, and the image and video processing were conducted using ImageJ (NIH, MD, USA).

5.3.2 Determination of device working frequency

As our acoustofluidic gradient generator works by driving the piezoelectric transducer, the working frequency of the piezoelectric transducer was experimentally determined by sweeping frequency with a 50 Hz increment from 1 kHz to 100 kHz. We observed that when the piezoelectric transducer was activated at 14.0 kHz, the sharp-edge structures generated strongest acoustic streaming effect. When operated at this frequency, our device maximized the mixing distance as shown in Fig. 5.1(c), indicating that more solutions could be mixed when other experimental conditions such as input voltages and flow rates remained unchanged. The frequency of 14.0 kHz was thus used in following experiments.

It is worth pointing out that, through our experiences and previous work, the working frequency of the device would be closer to the resonance frequency of the piezoelectric transducer we employed (3 ± 0.5 kHz was the resonance frequency of the piezoelectric transducer employed in this work). The identification of the optimum frequency is complicated by a number of factors. For example, the

bonding of piezoelectric transducer onto the glass slide and the amount of epoxy coated for bonding would result in a shift of the working frequency. However, since the working frequency of our sharp-edge-based gradient generator is significantly larger than the resonance frequency of the piezoelectric transducer, we believe that the optimum frequency, namely, the frequency at which most pronounced acoustic streaming are generated), might be governed by the vibration profile of the glass slide. A more detailed study to understand the vibration profiles of the glass slide and its influence on the streaming patterns inside the microfluidic channel is underway. In this work, however, we chose to experimentally determine the working frequency. Therefore, in this work, to make all the gradient-generation devices as identical as possible, we managed to make PDMS devices with identical dimensions (thickness, width and length) using pre-designed marks and bond each piezoelectric transducer onto each glass slide at exact same locations with equal amount of epoxy. By doing so, we experimentally observed that all of our gradient-generation devices could work at their best performance when driven by the working frequency of 14.0 ± 0.5 kHz.

5.3.3 Cell preparation

Human dermal microvascular endothelial cells (HMVEC-d, ATCC, VA, USA) were grown in EndoGRO-LS complete media (Millipore, MA, USA) in a CO₂ incubator (Nu-4750, NuAire, MN, USA), which maintained a temperature of 37 °C and a CO₂ level of 5%. Cells grown to 80 - 90% confluency were trypsinized (Trypsin-EDTA-0.05%, Gibco, Life Technologies, NY, USA), washed with PBS, re-suspended in a new culture medium at desired cell concentrations, and seeded into the channel for experimentation.

5.3.4 Cell migration

In order to verify if the concentration gradients generated by our acoustofluidic gradient generator can be applicable for cell studies, cell migration experiments using HMVEC-d cells were conducted with our gradient generator. To do so, HMVEC-d cells were cultured on-chip inside the channel of our device. The channels were first coated with fibronectin (100 μ g/mL; Cat. no. 356008, BD Biosciences, NJ, USA) for 1 hour. After coating, the channels were flushed with PBS several times

to remove residual fibronectin. Suspended HMVEC-d cells (1×10^6 cells per mL) were then injected into the channel through the PBS inlet (InletPBS), and as such they were dispersed mostly near both sidewalls of the channel. The cells were allowed for 30 minutes to adhere to the bottom surface of the device coated with fibronectin. Once they adhered to the substrate, pure EndoGro-LS media and EndoGro-LS media mixed with Human VEGF 165 (50 ng/mL; Cat. no. 293-VE-010, R&D systems, MN, USA; here called "VEGF") were injected into the channel, respectively, through the PBS inlet and the FITC inlet (InletFITC) at a flow rate ratio of 5 ($R_{FLOW} = 5$; $Q_{EndoGro} = 2.5 \mu\text{L}/\text{min}$ to $Q_{VEGF} = 0.5 \mu\text{L}/\text{min}$). Prior to the onset of establishing a VEGF gradient, we took an image to record the initial positions of the HMVEC-d cells ($t = 0$ hours). Once the VEGF gradient was established, images were taken every 5 minutes to record cell movement. After 6 hours, the VEGF gradient was shut off, and the cell migration region was divided into three zones (two side zones and one center zone). We tracked the movement of those cells seeded initially in two side zones, while those seeded in the center zone were excluded because they barely moved in response to a high-concentration VEGF after 6 hours (Fig. 5.3).

We determined the number of cells for different types of movement. For comparison, cell migration experiments in which cells were exposed to only EndoGro medium were conducted as a negative control (N-control). In addition, as a positive control (P-control), cell migration experiments were conducted with media of the same conditions as the experimental group, but the VEGF gradient was OFF-state (in the absence of acoustic field). Three independent experiments were carried out for each of the three groups.

5.3.5 Cell viability

To evaluate the biocompatibility of our acoustofluidic gradient generator for cell study, cell viability in our device was assessed after lasting exposure to an acoustic field. The assessment of cell viability was carried out by staining the HMVEC-d cells with live-stain Calcein-AM (CaAM) (Life Technologies, NY, USA) and propidium iodide (PI) (Sigma-Aldrich, MO, USA) after exposure to the acoustic field for 6 hours in our device. To do so, 1 *mathrmmL* PBS containing 1 μL Calcein-AM as well as 1 μL PI was infused into the channel at a flow rate of

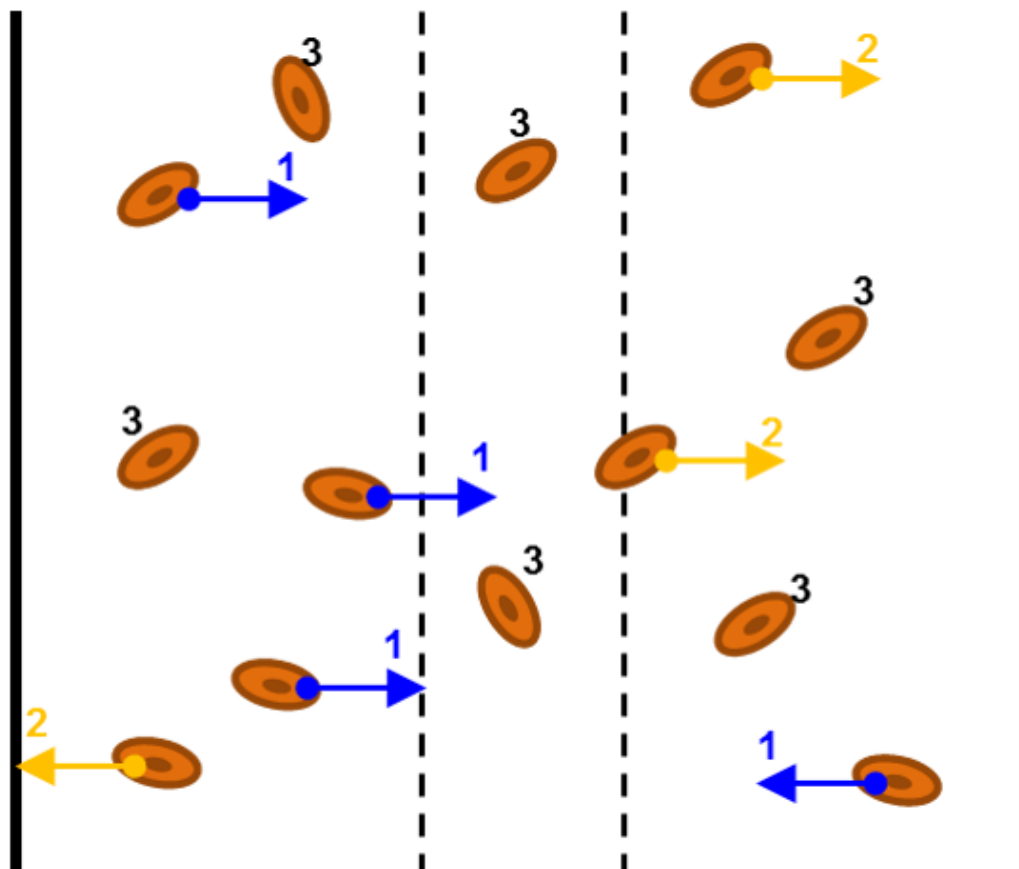


Figure 5.3. Schematic showing our approach to characterize cell movement. 1, 2, and 3 mark, respectively, those cells which moved toward the center (high VEGF concentration), away from the center (low VEGF concentration), and barely moved, after 6 hours. Tracking the position of each cell, we determined the type of movement for each cell. By doing so, we were able to determine the number of cells for different types of movement.

2 $\mu\text{L}/\text{min}$ for 15 minutes. Afterward, pure PBS was injected at a flow rate of 2 $\mu\text{L}/\text{min}$ for 15 minutes to wash out residual viability dyes. As a control group, we assessed the cell viability of those HMVEC-d cells which were cultured in the channel for 6 hours with no exposure to the acoustic field. Three independent experiments were performed for both the control and experimental groups.

5.3.6 Statistical analysis

Data were presented as group means \pm standard deviation (SD), and were analyzed by one-way ANOVA test using Prism 6.0 (GraphPad Software Inc., CA, USA). Differences among treatment groups were determined by Tukey's Multiple

Comparison test. A p -value of less than 0.05 was considered statistically significant.

5.4 Results and discussion

5.4.1 Characterization of flow patterns in the gradient generator

The shape and arrangement of the sharp-edge structures were redesigned in this work, differing greatly from structures designed in our previous work [38, 50, 86, 96]. We first conducted experiments to verify if the sharp-edge structures, once acoustically oscillated by the piezoelectric transducer, can induce acoustic streaming effect in the channel. Therefore, we first visualized and characterized the flow patterns and the acoustic streaming patterns generated inside the channel of our acoustofluidic device, by injecting into the channel DI water containing dragon green fluorescent beads of $1.9 \mu\text{m}$ diameter (Bangs Laboratories, IN, USA). Figure 5.4 shows the experimentally observed and numerically simulated flow patterns and acoustic streaming effect at the sharp-edge-structure region. Without a background flow, the fluorescent beads remained stationary in the absence of an acoustic field (*i.e.*, the piezoelectric transducer was inactivated), as shown in Fig. 5.4(a). In the presence of an acoustic field (*i.e.*, the piezoelectric transducer was activated), acoustic streaming effects developed around the tip of each sharp-edge structure as a result of acoustically oscillating sharp-edge structures, as shown in Fig. 5.4(b). Upon the introduction of a background flow (from left to right), a laminar flow profile was observed when the piezoelectric transducer was inactivated (Fig. 5.4(d)); once the piezoelectric transducer was activated, the acoustic streaming effect could develop around the tip of each sharp-edge structure. It is worth noting that the background flow significantly suppressed the acoustic streaming pattern to narrow rolls, as shown in Fig. 5.4(e).

To understand the complex flow patterns developed inside the microfluidic channel with sharp-edge structures, we conducted numerical simulations of the bead trajectories. The acoustic streaming flow was calculated using the perturbation approach [37]. The details of this approach and the particle tracking methodology can be found in Section 2.2.3 [38]. The numerical simulations of particle trajectories both without and with the background flow are shown in Fig. 5.4(c) and

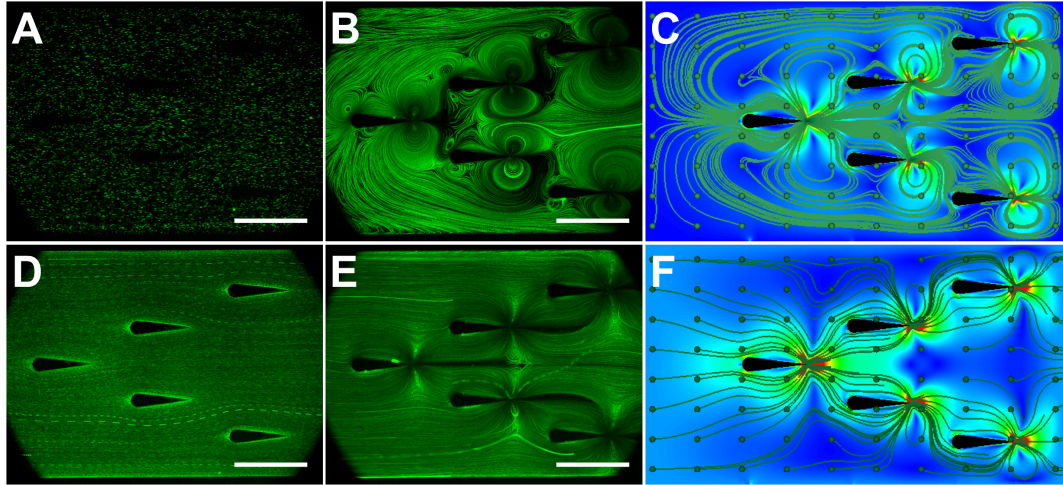


Figure 5.4. (a) Fluorescent polystyrene beads seeded randomly inside the microchannel for visualization of flow profiles. (b) Experimentally observed streaming profile around the sharp-edge structure on acoustic actuation visualized via trajectories of $1.9 \mu\text{m}$ diameter fluorescent beads. (c) Numerically simulated trajectories of 80 beads seeded uniformly inside the channel showing good qualitative agreement with the experimental results in (b). (d) Flow profile around sharp-edge structures due to a background laminar flow in the absence of acoustic actuation. (e) Experimentally observed trajectories of $1.9 \mu\text{m}$ diameter fluorescent beads. These resulted from the combination of acoustically generated streaming and the background laminar flow. (f) Numerically simulated trajectories of 80 beads seeded uniformly inside the channel about the structures shown in (e). Scale bar: $500 \mu\text{m}$.

(f), respectively. The numerical results are in good qualitative agreement with the experimentally observed trajectories. It was observed in simulations that the background flow velocity can be tuned in conjunction with the input power of acoustic actuation to control the suppression of the acoustic streaming. The correspondence between flow patterns both experimentally observed and numerically simulated implies that the operation of our device can be predicted and controlled.

5.4.2 Generation of concentration gradients

In this section, we validated the generation of concentration gradient using PBS and FITC-dextran solutions. The two solutions were independently pumped into the channel at different flow rates ($Q_{PBS} = 2.5 \mu\text{L}/\text{min}$ & $Q_{FITC} = 0.5 \mu\text{L}/\text{min}$). Unless otherwise specified, in this work the flow rate ratio ($R_{FLOW} = Q_{PBS}/Q_{FITC} = 5$) of PBS and FITC-dextran remained constant for all experiments. To quanti-

tatively characterize the concentration gradients generated using our device, fluorescent images were captured from different regions: sharp-edge-structure region, region 1, region 2, and the migration region (region 3), followed by normalizing their fluorescence intensity to that of 100% FITC-dextran (1 mg/mL) measured at the region upstream the sharp-edge-structure region. Fig. 5.5(a) - (c) show the fluorescent images of FITC-dextran concentration gradients at different regions and under different input voltages. When the piezoelectric transducer was off, a side-by-side laminar flow was observed due to low Reynolds number in the microfluidic channel (Fig. 5.5(a)). Once the piezoelectric transducer was turned on with a voltage of $10 V_{PP}$, the acoustic streaming induced mixing in a step-wise fashion, thereby generating concentration gradients of FITC-dextran (Fig. 5.5(b)). As the input voltage was increased to $15 V_{PP}$, the mixing width increased owing to the increase in the strength of acoustic streaming; as a result, FITC-dextran (bright portion) was mixed with more PBS (dark portion), generating a shallower FITC-dextran gradient than that generated by $10 V_{PP}$.

Figures. 5.5(d) - (f) show the corresponding normalized gradient profiles under different input voltages at the three regions (with different channel widths) downstream the channel. When the piezoelectric transducer was OFF, steeper gradient profiles were formed solely from the free diffusion of PBS and FITC-dextran. As the input voltage was increased, the increased mixing width enabled the mixing of FITC-dextran with more PBS buffer, forming shallower gradient profiles. Once a driving voltage of $25 V_{PP}$ was applied, a nearly flat gradient profile was established because the mixing spanned the entire channel due to stronger acoustic streaming. The results demonstrate that by adjusting the input voltage (*i.e.*, adjusting the mixing distance), the gradient profiles are modulated, proving our sharp-edge-based acoustofluidic gradient generator spatially controllable. Additionally, the plots also illustrate that the width of gradient profiles could be tuned over a range, in this work from $1500 \mu\text{m}$ to $700 \mu\text{m}$, by changing the width of the channel downstream. We expect that the width of gradient profile can be further widened to several millimeters, or narrowed down to $50 \mu\text{m}$ [131]. By alternating the piezoelectric transducer, the gradient could be actively formed and removed in real time, and even in downstream regions the gradient could still be established and shut off within just a few seconds. This not only shows the temporal controllability of our device, but also reveals that we can expose cells from one gradient to another

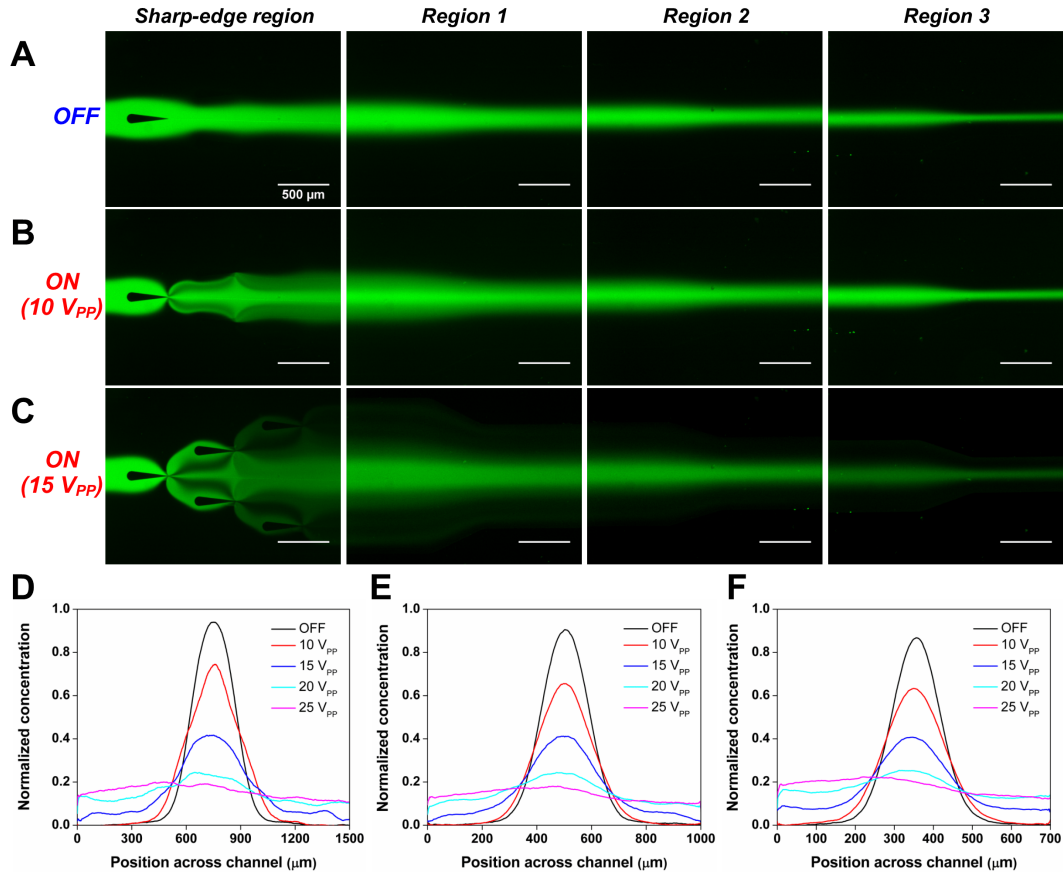


Figure 5.5. Fluorescent images of generated FITC-dextran gradients at different regions (from left to right: sharp-edge-structure region, region 1, region 2, and region 3) when (a) the piezoelectric transducer is inactive, and the piezoelectric transducer is on at (b) 10 V_{PP} and (c) 15 V_{PP}. The plots show the corresponding gradient profiles under different voltages at three regions downstream the channel: (d) region 1: 1500 μm wide, (e) region 2: 1000 μm wide, and (f) region 3: 700 μm wide. The results show that spatially controlled gradients may be generated by adjusting the input voltage of the piezoelectric transducer and the channel width downstream the channel.

(*e.g.*, from gradient-OFF to gradient-ON) within a few seconds.

To demonstrate the flexibility of our sharp-edge-based acoustofluidic gradient generator, furthermore, we constructed the sharp-edge structures in an arrangement which established another gradient profile. As shown in Fig. 5.6, we reconfigured the arrangements of the sharp-edge structures to establish another type of gradient profile. With this specific arrangement of sharp-edge structures, a mono-directional, linear gradient was generated. By adjusting the driving voltage of the piezoelectric transducer, the gradient profile was adjusted accordingly.

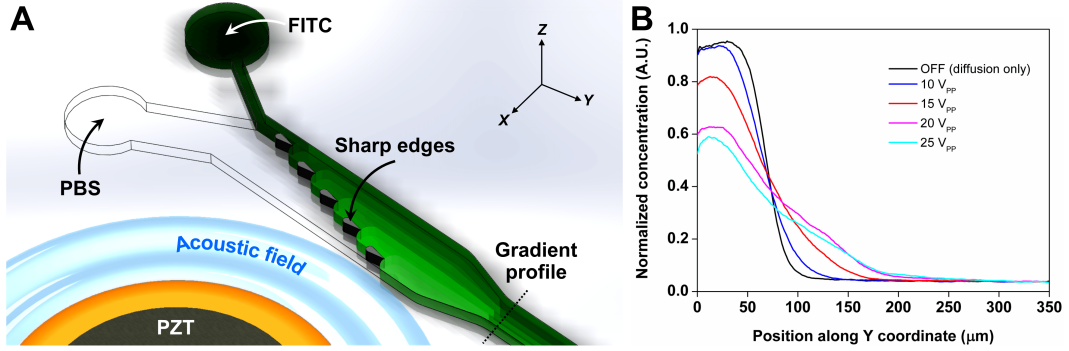


Figure 5.6. (a) Schematic showing the alternative design (*i.e.*, to differently arrange sharp-edge structures inside the channel) of our sharp-edge-based acoustofluidic gradient generator to generate different gradient profiles. (b) Plot showing the corresponding gradient profiles at region of interest (dashed line) under different input voltages of the PZT. The results prove that by differently arranging the sharp-edge structures, various gradient profiles could be generated.

Additionally, the temporal controllability of this type of gradient was also tested by alternating the piezoelectric transducer). The results show the flexibility of our sharp-edge-based acoustofluidic gradient generator. In other words, we can, in conjunction with the simulation approach we reported [38], arrange the sharp-edge structures differently to establish concentration gradients with prescribed characteristics.

5.4.3 The effect of flow rate on the gradient generation

Our acoustofluidic gradient generator mixes two fluids using acoustic streaming effect caused by the oscillating of sharp-edge structures. This effect can be suppressed by introducing higher flow rates into the channel [38, 50]. In this work we also investigated the effect of flow rate, including the total flow rate ($Q_{TOTAL} = Q_{PBS} + Q_{FITC}$) and the flow rate ratio inside the channel, on the formation of a FITC-dextran concentration gradient under a constant driving voltage. When studying the effect of total flow rate, we kept the flow rate ratio constant ($R_{FLOW} = 5$), while gradually increasing the flow rates of PBS and FITC-dextran. Fig. 5.7(a) shows the fluorescent images captured at the sharp-edge-structure region when various total flow rates were applied with a driving voltage of 25 V_{PP}. At a lower total flow rate ($Q_{TOTAL} = 3 \mu\text{L}/\text{min}$; $Q_{PBS} = 2.5 \mu\text{L}/\text{min}$; $Q_{FITC} = 0.5 \mu\text{L}/\text{min}$), a nearly-complete mixing of FITC and PBS in the channel was observed (Fig. 5.7(a)),

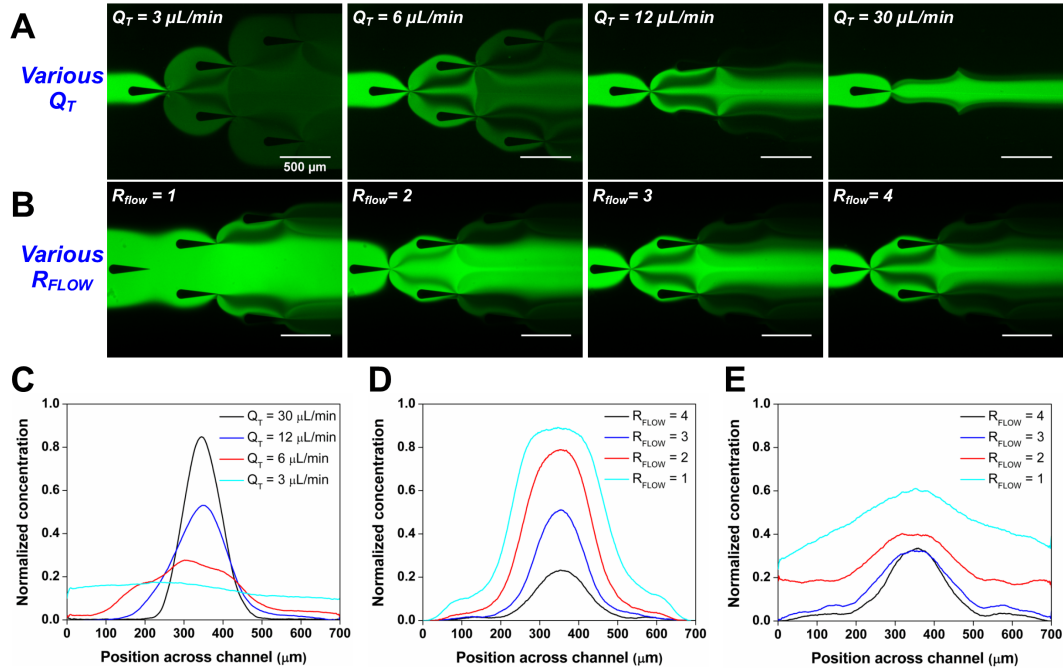


Figure 5.7. Fluorescent images of mixing behavior of FITC-dextran and DI water at the sharp-edge-structure region by varying (a) the total flow rates of the fluids inside the channel (the flow ratio remained constant), and (b) the flow rate ratio of the two fluids (the total flow rate remained constant). The plots show the corresponding gradient profiles at region 3 downstream the channel by changing (c) the total flow rates of the fluids inside the channel (the flow ratio remains constant, *i.e.*, $R_{FLOW} = 5$), (d) the flow rate ratio of the two fluids (the total flow rate remains constant), and (e) the flow rate ratio of the two fluids (the total flow rate is varied). These results demonstrate that by adjusting the total flow rate and the flow rate ratio, various gradient profiles may be generated using our acoustofluidic device.

yielding a flat concentration profile (Fig. 5.7(c)). Along with the increase in total flow rate, the mixing width was reduced (Fig. 5.7(a)), forming steeper gradient profiles (Fig. 5.7(c)). The results suggest that under a fixed input voltage, the ability to oscillate sharp-edge structures to induce acoustic streaming could be suppressed by high flow rates, which is in accordance with our previous finding [38, 50]. In other words, we could alternate the total flow rate to adjust the gradient profiles. Under two different flow rates, mixing behavior at the sharp-edge-structure region was compared in response to the change in driving voltage (Fig. 5.8).

When changing the flow rate ratio without changing the total flow rate ($Q_{TOTAL} = 6 \mu\text{L}/\text{min}$) and the driving voltage ($25 V_{PP}$), we could shift the position of the interface of two solutions. As such we established various concentration gradient

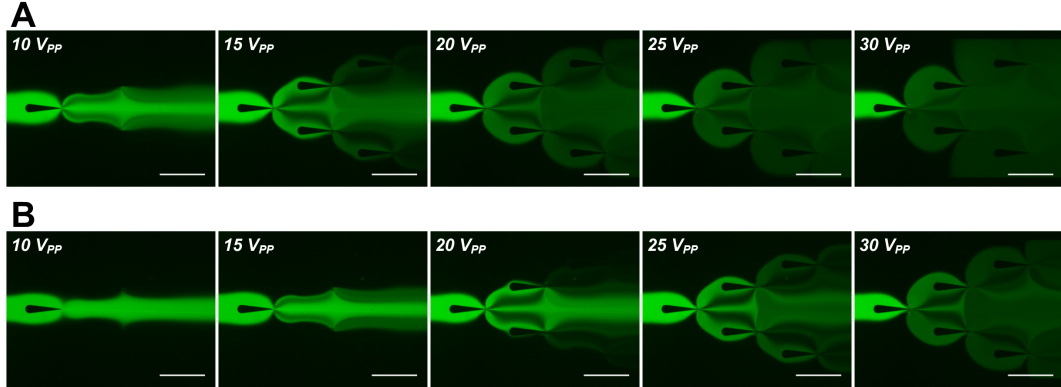


Figure 5.8. Fluorescence images of mixing behavior of FITC-dextran and DI water at sharp-edge-structure region under different working voltages when the total flow rates of the fluids inside the channel is (a) $3 \mu\text{L}/\text{min}$ and (b) $6 \mu\text{L}/\text{min}$. The flow rate ratio remains constant, *i.e.*, $R_{FLOW} = 5$. These results clearly reveal that increasing the total flow rate inside the channel would significantly suppress the acoustic streaming and therefore, leads to different mixing behavior. On the other hand, however, various gradient profiles can be established by adjusting the total flow rates and the driving voltage. Scale bar: $500 \mu\text{m}$.

profiles (Fig. 5.7(b) & (d)). Moreover, as shown in Fig. 5.7(e), once the total flow rate was changed along with the flow rate ratio ($Q_{FITC} = 1 \mu\text{L}/\text{min} = \text{constant}$), we generated gradient profiles (Fig. 5.7(e)) different from those in Fig. 5.7(d). The results once again show that with our device, the widths and heights of gradient profiles (or a related measure such as the slope of a gradient profile) are easily controlled by adjusting the flow rates of two solutions.

5.4.4 Temporal control of gradient generation

In contrast to existing passive gradient generators [130,131], our acoustofluidic gradient generator generates concentration gradients in an active fashion — a feature of particular importance for time-dependent cell studies. Aside from the ability to generate static concentration gradients of various profiles by adjusting the flow rate and the input voltage, our acoustofluidic device generates temporally controllable gradients by modulation of the input signal of the piezoelectric transducer. Figure 5.9(a) shows the fluorescent images of a complete cycle of gradient generation by alternately triggering the piezoelectric transducer with a period ($T_{Trigger}$) of 4 seconds (*i.e.*, 2-sec ON and 2-sec OFF). Alternating the piezoelectric transducer, we generated an alternating gradient profile at an alternating frequency of

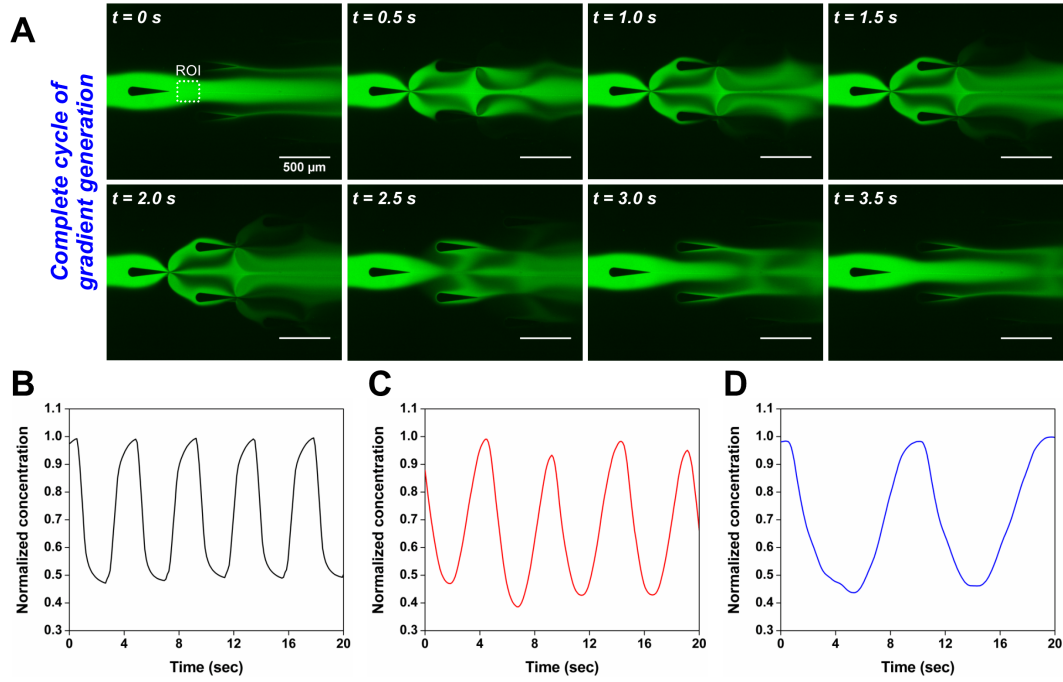


Figure 5.9. (a) Fluorescent images showing a complete cycle of gradient generation at an ON/OFF frequency of 0.25 Hz ($T = 4$ seconds). The plots show the corresponding fluorescence intensity profiles at regions of interest (ROI) in (a), when the gradient generator was operated at (b) an ON/OFF frequency of 0.25 Hz, (c) by sweeping the working frequency of the piezoelectric transducer from 13 kHz to 14 kHz within 4 seconds, and (d) within 8 seconds. The results demonstrate the spatiotemporal control of the chemical gradient generation using our sharp-edge-based acoustofluidic device.

0.25 Hz (Fig. 5.9(b)), which is comparable to other existing acoustic-based gradient generators [83, 135]. By adjusting the triggering period, we will be able to generate gradient profiles of various alternating frequencies. The results demonstrate that our sharp-edge-based acoustofluidic device generates not only spatial concentration gradients, but also temporal concentration gradients. The temporal resolution of our sharp-edge-based acoustofluidic gradient generator, namely the alternating frequency, can be further improved by increasing the flow rate, or even changing the arrangement of the sharp-edge structures; however, there are a few things that need to be taken into consideration. Increasing flow rate, for example, may also generate high flow shear stresses that may result in undesirable cellular behavior; additionally, when introducing high flow rates, higher driving voltages would be required to generate gradient profiles similar to those generated under low flow rates.

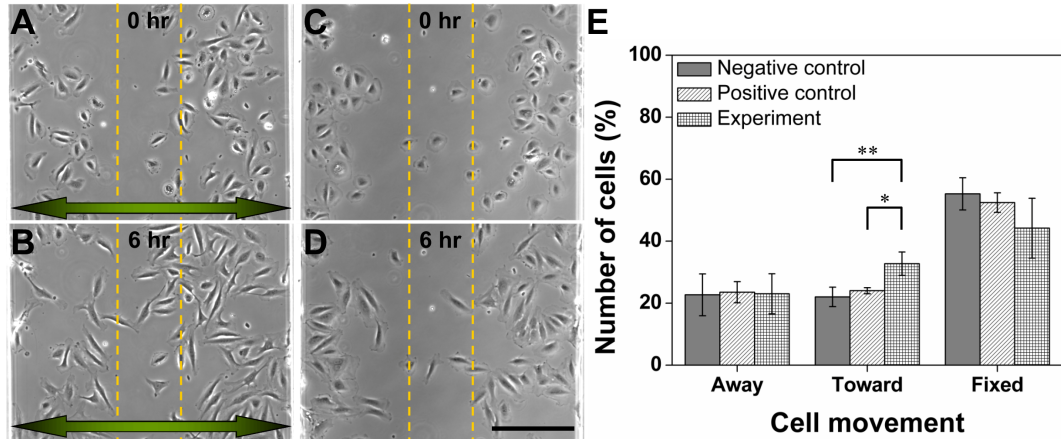


Figure 5.10. HMVEC-d chemotaxis in the cell culture chamber. (a, b) Representative phase contrast image of cell positions at time = 0, 6 hours during chemotaxis. (c, d) Representative phase contrast images of cell positions at time = 0, 6 hours when only pure medium was present. The arrow points toward lower VEGF concentrations. (e) The percentage of cell movement in the cell culture chamber under various VEGF concentration conditions. Data represent averages of $n = 3$ independent experiments \pm standard deviation ($*p < 0.05$, $**p < 0.01$). Scale bar: $200 \mu\text{m}$.

To further demonstrate the spatiotemporal controllability of our acoustofluidic gradient generator, we alternated the piezoelectric transducer by sweeping the driving frequency for different time intervals. Figs. 5.9(c) and (d) show the corresponding concentration profiles at the region of interest (ROI) by sweeping the driving frequency from 13.0 to 14.0 kHz, respectively, with sweeping times (T_{Sweep}) of 4 and 8 seconds. We generated spatiotemporally controllable gradient profiles, and this capability can be useful to elucidate time-resolving cellular signaling dynamics.

5.4.5 Cell migration in our acoustofluidic device

Thus far, we have demonstrated the capability and spatiotemporal controllability of our sharp-edge-based acoustofluidic gradient generator via the aforementioned experiments and characterizations. To further validate our device for cell studies (*i.e.*, applicability and biocompatibility), we conducted HMVEC-d cell migration experiments within our sharp-edge-based acoustofluidic gradient generator.

To demonstrate HMVEC-d cell migration in response to a VEGF concentration gradient generated by our device, the channels were injected with pure EndoGro-LS

media and EndoGro-LS containing VEGF, respectively, at $Q_{EndoGro} = 2.5 \mu\text{L}/\text{min}$ and $Q_{VEGF} = 0.5 \mu\text{L}/\text{min}$. Under an input voltage of $15 V_{PP}$, a VEGF gradient profile as shown in Fig. 5.5(f) ($15 V_{PP}$) was generated with a maximum concentration of $\sim 25 \text{ ng}/\text{mL}$ in the center of the channel, and a minimum concentration of $\sim 10 \text{ ng}/\text{mL}$ near both the sidewalls. The position of each HMVEC-d cell was recorded by taking images every 5 minutes, from $t = 0$ to 6 hours. Figures 5.10(a) and (b) show the relative position of HMVEC-d cells, respectively, before and after 6 hours' exposure to the VEGF gradient (experimental group). As shown in Fig. 5.6(e), when exposed to the VEGF gradient for 6 hours, 33% of the cells seeded initially in the two sidewall zones had migrated toward the center of the channel (higher VEGF concentration), 23% of the cells migrated toward the sidewall (lower VEGF concentration), and 44% barely moved. In the absence of a VEGF gradient (negative-control group: pure medium only), by contrast, a striking decrease of nearly 11% (from 33% to 22%) in the number of cells migrating toward the center was observed, along with changes in the number of cells moving toward the sidewall ($\sim 23\%$) and barely moving ($\sim 55\%$). Additionally, in the presence of a VEGF gradient which was formed solely from diffusion (positive control group; Figure 5.5(f)), the number of cells moving toward the center increased by only about 2% (from 22% to 24%), with insignificant changes in the number of cells moving toward the sidewall ($\sim 24\%$) and barely moving ($\sim 52\%$). Collectively, the number of cells moving toward the center when exposed to a VEGF gradient was statistically greater than those which were exposed to the pure medium and the diffusion-based VEGF gradient. The results demonstrate that our acoustofluidic device generates VEGF gradients which in turn initiate HMVEC-d chemotaxis, demonstrating the capability of our device for cell chemotaxis studies.

5.4.6 Cell viability in the presence of lasting acoustic field

Our sharp-edge-based acoustofluidic device operates based upon acoustic streaming effect induced by the activation of a piezoelectric transducer. We assessed cell viability upon acoustic streaming induced by sharp-edge structures as well as an applied acoustic field, by subjecting cells to the acoustic field for 6 hours (driving voltage = $20 V_{PP}$). Figure 5.11 illustrates cell viability within the channel of our gradient generation device. As the representative bright-field images

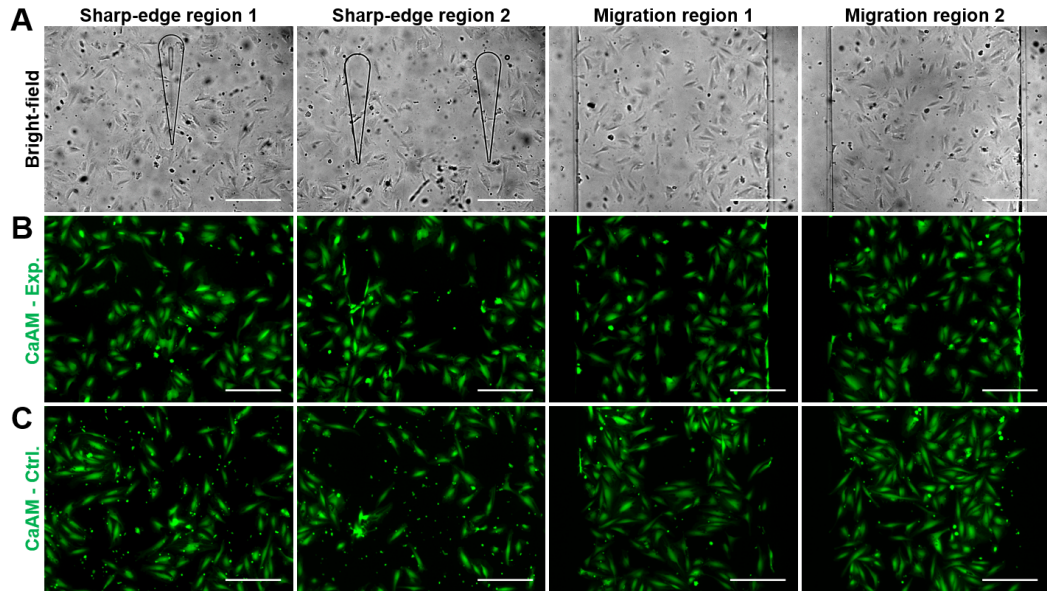


Figure 5.11. (a) Representative bright field (BF) images showing the cell morphology at sharp-edge-structure regions and cell migration regions. Corresponding fluorescent images showing the cell viability after 6 hours (b) in the absence of an acoustic field (control group) and (c) in the presence of an acoustic field (experimental group). Scale bar: 200 μm .

show, we monitored the cell viability for cells which were seeded in the sharp-edge-structure region and the migration region (region 3) (Fig. 5.11(a)). After 6 hours' exposure to the acoustic field, HMVEC-d cells still adhered to the substrate without any irregular morphology. Further, the HMVEC-d cells seeded in both the sharp-edge-structure region and the migration region remained viable; no dead cells were observed (Fig. 5.11(b)). The results are comparable to those obtained in control-group experiments (absence of an acoustic field) (Fig. 5.11(c)). These results illustrate that our sharp-edge-based acoustofluidic gradient-generation device is biocompatible.

Extending the assessment of cell viability, we found that after 16 hours' exposure to an acoustic field (driving voltage = 20 V_{PP}), the HMVEC-d cells were still viable and present with normal morphology at different regions inside the channel (Fig. 5.12). These results again prove our device biocompatible, as well as viable for cell studies where long-term cell culture is required.

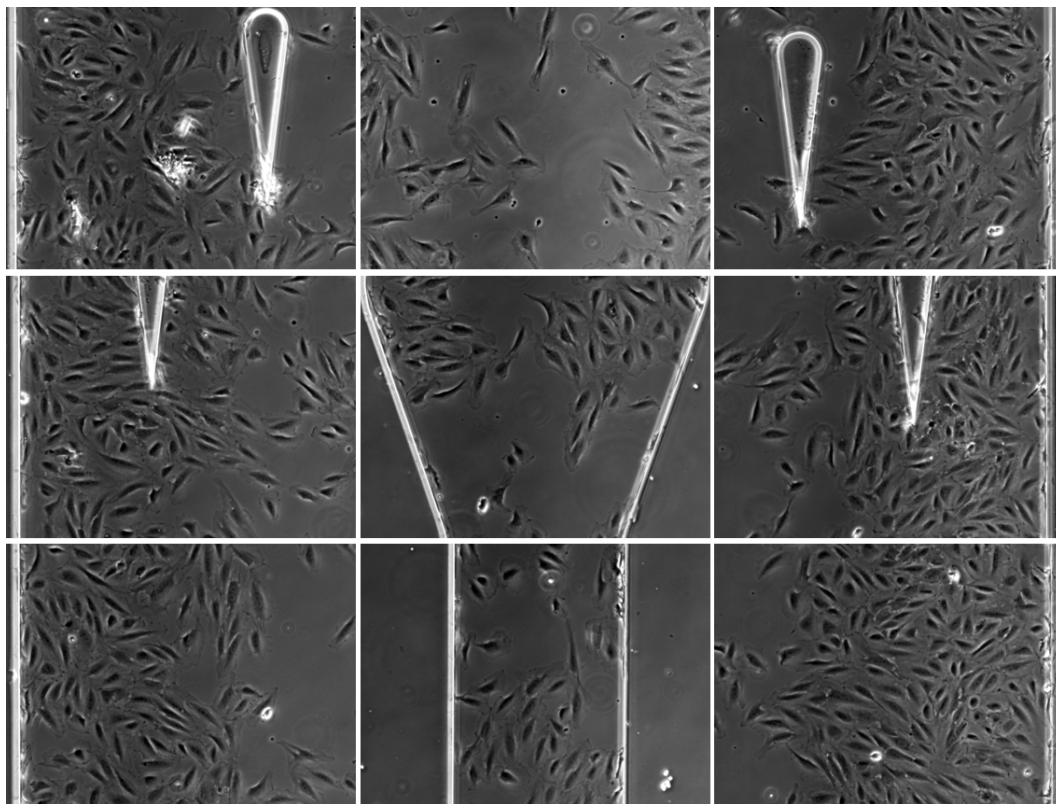


Figure 5.12. Representative bright field images taken at different regions in the channel showing the HMVEC-d cells morphology after 16 hours of the presence of acoustic field. The cells still appeared viable and active, demonstrating the biocompatibility of our acoustofluidic gradient generator for biological studies where long-term cell culture is needed. Scale bar: 200 μm .

5.5 Summary

In this chapter, we demonstrate that chemical gradient which are spatiotemporally stable and of tunable concentration can be generated using our sharp-edge-based acoustofluidic gradient generator. In contrast to existing microfluidic gradient generators, in which the gradients are formed solely based on passive mechanisms, our device forms gradients in an active, controllable manner. Using our device, it is possible to generate gradients with complex profiles by changing the flow rate ratio of co-flowing fluids (stimulant and buffer), the driving voltage of the piezoelectric transducer, and the arrangement of sharp-edge structures (spacing). Moreover, temporally changing gradients can be easily generated by varying the driving voltage and the actuation time of the piezoelectric transducer. Our device

is well-suited for many chemical/biological studies and applications, such as investigating cell chemotaxis, differentiation, migration, and drug discovery in dynamic chemical environments. The effect of pulsatile chemical gradient upon cellular dynamics can be unveiled and much temporal information about cell signaling will be extracted upon development of our platform.

Chapter 6

Sharp-edge-based acoustofluidic micropump

In Chapter 3 – 5, various applications have been demonstrated from simple fluid mixing to the generation of chemical gradients, primarily based on the mixing mechanism enabled by the acoustic streaming. Expanding the potential of the acoustic streaming induced by oscillating sharp-edge structure, in this chapter, we present a programmable acoustofluidic pump that utilizes the acoustic streaming effect generated by the oscillation of tilted sharp-edge structures. This sharp-edge-based acoustofluidic micropump is capable of generating stable flow rates as high as $8 \mu\text{L}/\text{min}$ (76 Pa of pumping pressure), and it can tune flow rates across a wide range (nanoliters to microliters per minute). Along with its ability to reliably produce stable and tunable flow rates, the sharp-edge-based acoustofluidic micropump is easy to operate and requires minimum hardware, showing great potential for a variety of applications. The work presented in this chapter has been reported in The 18th International Conference on Miniaturized Systems for Chemistry and Life Sciences (MicroTAS 2014), published and featured as the **Front Cover Article** in Journal of *Lab on a Chip* [96], and selected as a **Lab on a Chip HOT Article** of 2014.

6.1 Motivation

In the past two decades, significant efforts have been made towards developing reliable and robust microfluidic pumps [138, 139]. These microfluidic pumps can be generally divided into two categories based on their driving mechanisms: passive pumps [140–142] and active pumps [143–145]. Passive pumps, particularly the surface-tension-based microfluidic pumps [145, 146], allow the manipulation of fluids without the need of peripheral equipment or moving parts, making them suitable to many portable analytical devices. Nevertheless, they are incapable of performing complex fluid manipulations as the flow direction and flow rate cannot be adjusted in real time and on demand, preventing their use in applications where multiple steps of fluid operations (*e.g.*, immunoassay) are required. In contrast, active pumps, which use mechanical or electrical actuations, or other external forces to initiate fluid pumping, offer much more flexibility in terms of fluid manipulations and can potentially provide solutions to the challenges faced by passive pumps.

Many active microfluidic pumps have been reported, including optically driven pumps [147, 148], electroosmotic pumps [18, 149], electrokinetic pumps [150, 151], dielectric pumps [152, 153], magnetic pumps [154, 155], laser-driven pumps [156], pneumatic membrane pumps [157, 158], bio-hybrid pumps [115, 159], and diffuser pumps [160]. Despite these advances, the existing active micropumps suffer from drawbacks such as complicated device fabrication, involvement of moving structures, and/or unstable and unreliable performance. Recently, implementation of acoustic streaming effects [161] in microfluidics has attracted great interest and enabled numerous applications, including mixing [11, 50, 135], particle manipulation [16, 162, 163], and flow control [84, 164]. Microfluidic pumps powered by acoustically oscillating microbubbles have also been demonstrated [10, 14]. These microbubble-based micropumps are simple to fabricate and operate; however, the performance of these pumps suffers from bubble instability, temperature dependence, and inconvenience of the bubble-trapping process.

In this chapter we establish a simple and reliable microfluidic pumping mechanism using acoustically driven solid sidewall microstructures known as “sharp-edge structures”. This work is built upon our previous finding that acoustic streaming effect can be induced by acoustically oscillating sharp-edge structures [38, 50]. With the acoustically induced acoustic streaming effect, we previously demon-

strated rapid and homogeneous fluid mixing inside a microfluidic channel [50]. In this work, we redesign the geometry and orientation of the sharp-edge structures and demonstrate that the sharp-edge-induced acoustic streaming can lead to applications beyond mixing. In particular, we demonstrate a highly effective, reliable, and programmable microfluidic pump with minimum hardware. Our sharp-edge-based acoustofluidic micropump can generate a flow rate of approximately $8 \mu\text{L}/\text{min}$, which corresponds to a pumping pressure of 76 Pa. Moreover, it is capable of generating flow rates ranging from nanoliters to microliters per minute — a capability that most existing microfluidic pumps do not possess. Our acoustofluidic pump can be operated on demand and features advantages, such as simple fabrication and operation, high reliability, compactness, and tunable flow rates without complicated moving parts.

6.1.1 Device design and concept

Fig. 6.1 schematically shows the design and working mechanism of our sharp-edge-based acoustofluidic micropump. Briefly, the acoustofluidic pump was made by bonding a single-layer polydimethylsiloxane (PDMS) channel onto a single glass slide and attaching a piezoelectric transducer (part no. 81-7BB-27-4L0, Murata Electronics) adjacent to it using a thin layer of epoxy (PermaPoxyTM 5 Minute General Purpose, Permatex). To demonstrate the pumping behavior, the PDMS channel was designed to be a rectangular recirculating (in a counter-clockwise direction) channel composed of four portions: left channel, right channel, upper channel, and lower channel. The lower channel, referred to as the pumping region, was designed with 20 tilted sharp-edge structures on its sidewall (10 on each side), while the other three channels were straight channels without any structures. The piezoelectric transducer, activated by amplified sine wave signals from a function generator (AFG3011C, Tektronix) and an amplifier (25A250A, Amplifier Research), was used to acoustically oscillate the sharp-edge structures to generate acoustic streaming effects. As shown in Fig. 6.1(b), the tilted sharp-edge structure, acoustically oscillated by the activation of the piezoelectric transducer, generates an acoustic streaming pattern around its tip; since the sharp-edge structures are tilted to the right, the streaming results in a net force directed to the right. Fluid pumping occurs because the generated net forces push the bulk fluid.

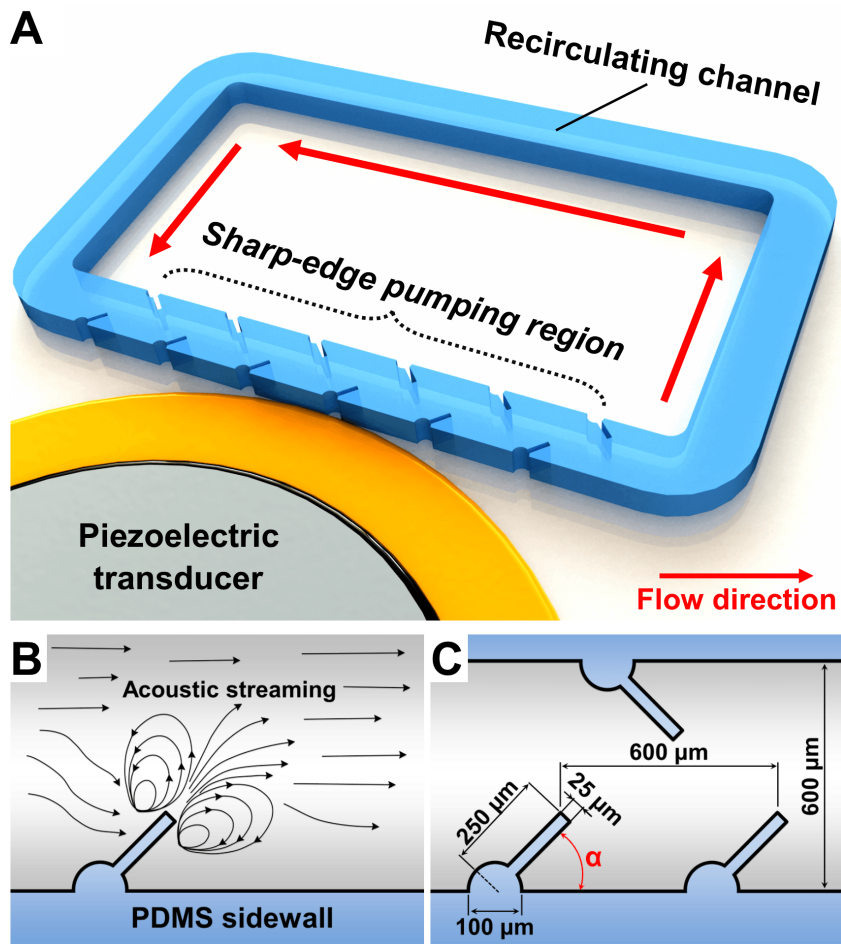


Figure 6.1. (a) Schematic of the sharp-edge-based acoustofluidic micropump. This device includes a PDMS microfluidic channel and a piezoelectric transducer. (b) Schematic showing the acoustic streaming phenomenon around the tip of a tilted oscillating sharp-edge structure. (c) Schematic showing the design of the channel and sharp-edge structure.

Fig. 6.1(c) shows the design of our acoustofluidic device. The microchannel has a width of $600\ \mu\text{m}$ and a depth of $100\ \mu\text{m}$, and each sharp-edge structure is identical. Different tilting angles (α) of the sharp-edge structures, including 30° , 45° , 60° , and 75° , were chosen to investigate the resulting pumping behavior and determine the best angle for optimal pumping performance.

6.2 Results and discussion

6.2.1 Streaming patterns and numerical simulations

To prove our concept and determine the working frequency of the piezoelectric transducer, the pumping device with 30° tilted sharp-edge structures was experimentally and numerically tested first. A solution containing DI water and dragon green fluorescent beads (Bangs Laboratory) with a diameter of $1.9 \mu\text{m}$ was injected into the channel to characterize the acoustic streaming patterns induced by the oscillation of tilted sharp-edge structures. After injecting the solution, the inlet/outlet ports were sealed by two separate tubes connected to two separate syringes, such that no pressure difference is present between the inlet and the outlet. By sweeping the frequency with a 50 Hz increment from 1 kHz to 100 kHz, we observed that the acoustic streaming patterns were developed around the tips of the oscillating sharp-edge structures when the piezoelectric transducer was activated at 6.5 kHz, as shown in Fig. 6.2(a). Based on these results, 6.5 kHz appeared to be the working frequency for the piezoelectric transducer to activate our pump. As a result, we used this frequency for all of the following experiments. Additionally, using the simulation approach we reported in Section 2.2.3 [38] to model the acoustically driven oscillating 30° tilted sharp-edge structures shown in Fig. 6.2(b), we found that the acoustic streaming effect produces a net flow of the fluid from left to right. These simulation results indicate pumping behavior and are also in good agreement with the experimental results we acquired. It should also be noted that in the simulations a flow singularity was observed at the sharp-edge structures, similar to that observed in our previous study [42], which is indicated by the maximum velocity at the tips of sharp-edge structures. This velocity increases with the mesh refinement and our solution is strictly valid only outside the boundary layer.

6.2.2 Visualization and characterization of pumping performance

To further visualize and characterize the pumping behavior, DI water mixed with polystyrene beads of different diameters ($10 \mu\text{m}$ and $0.9 \mu\text{m}$) was injected into the

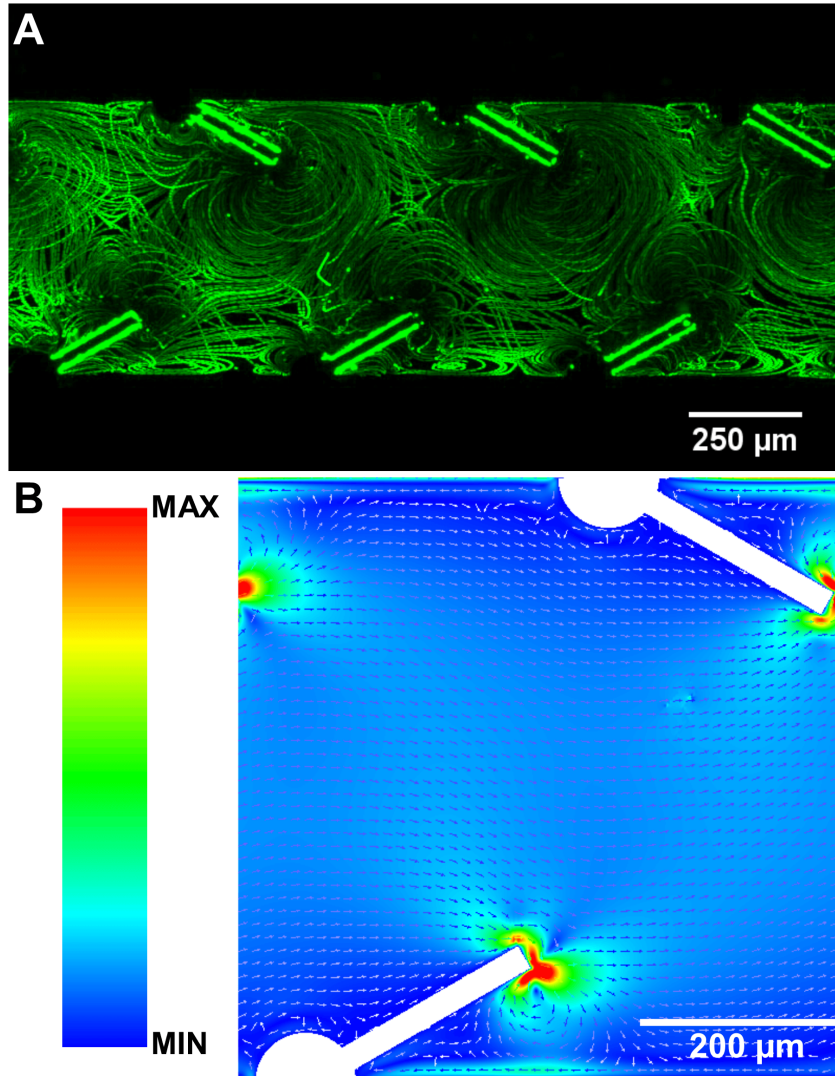


Figure 6.2. (a) Characterization of the acoustic streaming patterns developed around the tips of the 30° tilted sharp-edge structures. (b) Simulated results showing the streaming velocity in our pump in the presence of an acoustic field: a net flow of fluid from left to right is generated.

channel. Fig. 6.3 shows the movement of polystyrene beads over time in the upper channel when the piezoelectric transducer was on (input voltage applied to the piezoelectric transducer = 20 V_{PP}), using the pumping device with 30° tilted sharp-edge structures. The results reveal that with the piezoelectric transducer activated, the representative groups of the beads (circled in red, yellow and blue) were moving from right to left, showing evidence that the fluid was being pumped and flowing along the recirculating channel.

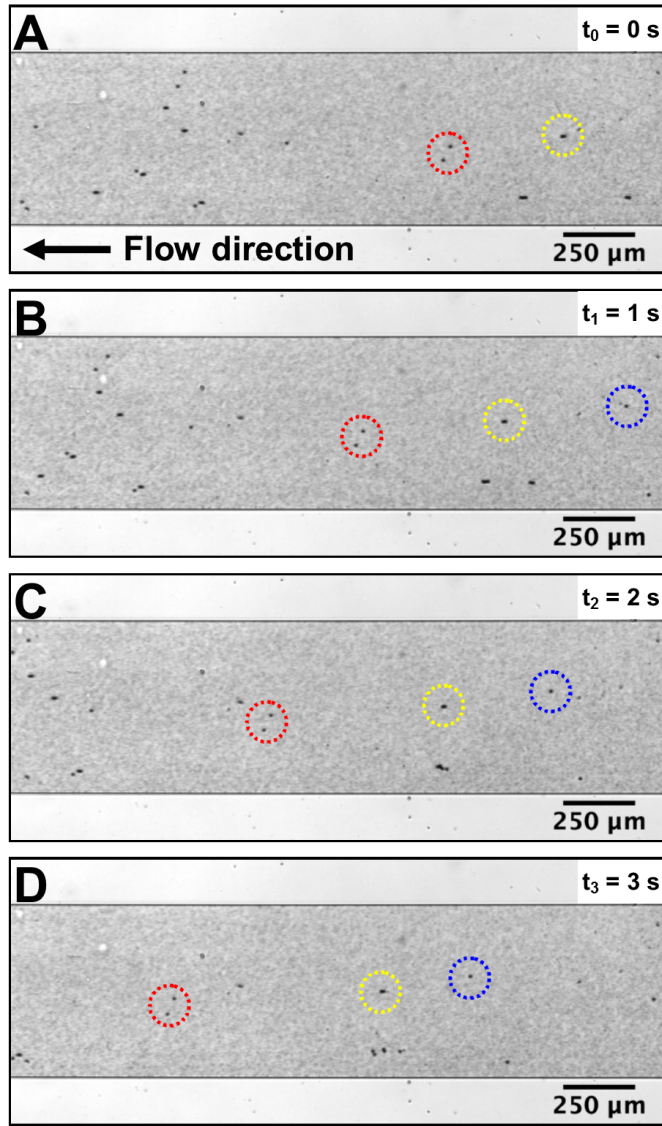


Figure 6.3. Experimental images showing the pumping behavior by indicating the movement of polystyrene beads at different time frames: a) $t_0 = 0$ sec, (b) $t_1 = 1$ sec, (c) $t_2 = 2$ sec, and (d) $t_3 = 3$ sec (red, yellow, and blue circles indicate three representative groups of beads).

After proving the proposed pumping concept and determining the working frequency for the piezoelectric transducer, we further investigated the influence of the tilting angle of sharp-edge structure on the pumping performance. To quantitatively do so, we estimated the average flow rate inside the channel. The average flow rate was calculated by tracking the average velocities of $10 \mu\text{m}$ beads in the upper channel, in which ~ 100 beads were randomly selected and tracked for each

independent experiment. In addition to the effect of the tilting angle, the pumping performance under different input voltages of the piezoelectric transducer was also characterized. Fig. 6.4(a) shows the pumping performance for the four different tilting angles of sharp-edge structures under different input voltages. The results show that when the piezoelectric transducer was activated with voltages ranging from 5 V_{PP} to 50 V_{PP} , pumping took place in all of the devices, regardless of the tilting angle of the sharp-edge structure. As the tilting angle decreased, the generated pumping flow rate increased. As shown in Fig. 6.4(a), of the four different tilting angles, the device with 30° tilted sharp-edge structures generated a significantly larger pumping flow rate, and with a voltage of 50 V_{PP} , it generated a flow rate as high as 8 $\mu\text{L}/\text{min}$. Using Poiseuille’s law [14] and considering the channel length (25 mm), this flow rate corresponds to a calculated pumping pressure of 76 Pa. The lower pumping flow rates generated by the 45°, 60°, and 75° tilted sharp-edge structures can be attributed to the fact that as the tilting angle increases, the component of the generated net force that is perpendicular to the flow direction also increases. As a result, the parallel component of the force that could push the bulk fluid to flow forward is decreased. Further work including different geometries of sharp-edge structure with smaller tilting angles to further improve the efficiency of our acoustofluidic pumps is under way. In addition, the results show a concurrent increase of the flow rate with voltage, demonstrating that the pumping flow rate could be controlled by adjusting the input voltages.

We discovered that our sharp-edge-based acoustofluidic micropump can conveniently achieve a wide range of pumping flow rates, from nanoliters to microliters per minute, by adjusting the input voltage applied to the piezoelectric transducer. Aside from the function of continuous fluid pumping, we also demonstrated that by alternately switching the piezoelectric transducer on and off at various burst frequencies (*e.g.*, 0.5 and 2 Hz), our sharp-edge-based acoustofluidic micropump can achieve pulsatile fluid pumping as shown in Fig. 6.4(b). These results imply that the profile of the pumping flow rate can possibly be modulated by programming the input signal to the piezoelectric transducer. Future work should include evaluation and optimization of pumping performance within different microchannel designs (*e.g.*, a straight, non-circulating microchannel).

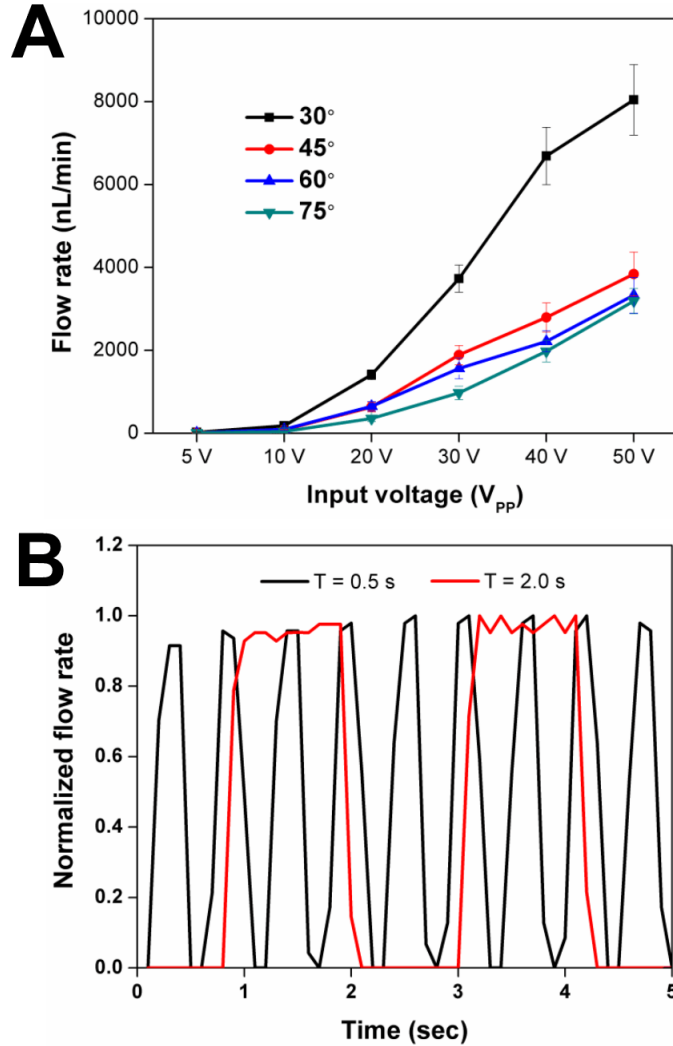


Figure 6.4. Experimental results illustrating the controllability and tunability of our sharp-edge-based acoustofluidic micropump. (a) Comparison of generated pumping flow rates with various tilting angles of sharp-edge structure as a function of the voltages applied to the PZT. The 30° tilted sharp-edge structures could generate a flow rate as high as 8 $\mu\text{L}/\text{min}$ under 50 V_{PP} . (b) Characterization of flow rate profiles by alternately switching the PZT on and off with different burst frequencies: burst frequency of 2 Hz (black) and burst frequency of 0.5 Hz (red).

6.3 Summary

In summary, we demonstrate a new class of acoustically driven, reliable, and programmable microfluidic pumps based on the oscillating tilted sharp-edge structures. Our sharp-edge-based acoustofluidic micropump could generate a pumping

flow rate as high as $8 \mu\text{L}/\text{min}$, and with more sharp-edge structures, the generation of higher flow rates can be expected. By tuning the input voltage, a wide range of pumping flow rates, from nanoliters to microliters per minute, could also be generated by a single pump. Moreover, by programming the input signal to the piezoelectric transducer, we could modulate the profiles of the pumping flow rates. In fact, it is possible to achieve various kinds of flow operations by programming the input signals to the piezoelectric transducer. With such features, our sharp-edge-based acoustofluidic micropump offers advantages over other microfluidic pumps in terms of not only simplicity, stability, reliability, and cost-effectiveness but also controllability and flexibility, which, when combined, make it valuable in many lab-on-a-chip applications.

Conclusions and Prospects

7.1 Conclusions

Over the past few decades, microfluidics has emerged as a powerful tool for a wide variety of applications, from chemical applications, such as monitoring of chemical reactions and material synthesis, to biological applications, such as cell differentiation and single-cell virology. We have also witnessed the rapid advancement of related technologies. Despite the advancement, the adoption of microfluidic devices in human daily life for diagnostic and therapeutic purposes is still very limited, the reason being that, to date only a few powerful fluid manipulation devices have been proposed. As an powerful fluid manipulation device, it has to operate in a simple, controllable, reliable manner with performance that is comparable to existing technologies, while minimizing the use of hardwares. Undoubtedly, the pneumatic-valves based fluid manipulation platform invented by Prof. Steven Quake [165,166], is by far the most powerful fluid manipulation technique among those available. The pneumatic-valves based fluid manipulation platform, however, not only necessitates the use of external bulky gas tanks and solenoid valves, but also complicates the design and fabrication of devices. To bring the whole microfluidic community several steps further toward the development of truly integrated microfluidic devices, there has been a pressing need to develop fluid manipulation devices that are simple in terms of fabrication, operation, and device configuration, reliable and controllable in terms of device performance, require minimum external hardwares, and the last, yet the most important — can be integrated with other microfluidic

components.

Implementing acoustic streaming effects in microfluidics, we have developed a series of acoustofluidic technologies that are able to control and manipulate fluids and micro-objects using acoustic streaming effect that is induced by oscillating sharp-edge structures. The sharp-edge-based acoustofluidic devices possess advantages including high biocompatibility, ease of manipulation, high flexibility and controllability, and low power consumption; these advantages altogether, make our sharp-edge-based acoustofluidic devices invaluable for many microfluidic applications. This dissertation contributes to understand, design, and prototype a new class of acoustofluidic devices to pave the foundation for applications, ranging from biomedical/chemical research to clinical applications. Taking a systematic approach toward **Oscillating-Sharp-Edge based Acoustofluidic Microdevices**, we have reached several milestones outlined as follows.

On-demand fluid mixing

An acoustofluidic micromixer was developed where rapid and homogeneous mixing of fluid was achieved *via* the acoustic streaming induced by oscillating sharp-edge structures. The acoustic streaming induced by the oscillation of sharp-edge structures allowed two fluids to interchange and thus enhances the mass transport across the channel, greatly improving the mixing efficiency. The effects of the driving frequency and driving voltage of piezoelectric transducer, the tip angle of sharp-edge structure, and the flow rate condition were thoroughly investigated and characterized. A mixing time as short as 180 ms was demonstrated at a flow rate of 4 $\mu\text{L}/\text{min}$ under a driving voltage of $\sim 31 V_{\text{PP}}$. Our sharp-edge-based acoustofluidic micromixer possesses desirable characteristics, including excellent mixing performance, simplicity, convenient and stable operation, fast mixing speed, and ability to be toggled on-and-off, which makes it a promising candidate for a wide variety of lab-on-a-chip applications.

Highly-viscous clinical human sputum liquefaction

Extending the capability of our sharp-edge-based acoustofluidic micromixer developed in Chapter 3, we demonstrated for the first time, to the best of our knowledge, the microfluidic liquefaction of clinical human sputum samples. By modifying our

sharp-edge-based acoustofluidic micromixer, we were able to consistently liquefy human sputum samples at a throughput of 30 $\mu\text{L}/\text{min}$ without compromising cell viability or sample integrity. The sputum samples liquefied using our sputum liquefier were comparable to those liquefied using a standard vortex mixer through analysis including visual comparison in the appearance, cell morphology, cell content, cell viability, and flow cytometry. Our sharp-edge-based acoustofluidic sputum liquefier could liquefy sputum samples over a range of viscosities. Our findings suggest that our acoustofluidic sputum liquefier is a promising candidate for incorporation with other on-chip components that will enable the development of a fully integrated, self-contained sputum processing and analysis platform. Moreover, our demonstration of liquefying sputum samples opens the gate for applications that require the processing of highly viscous fluids.

Spatioemporal generation of chemical gradients

The ability to generate stable, spatiotemporally controllable concentration gradients is critical for resolving the dynamics of cellular response to a chemical microenvironment. Engineering the acoustic streaming patterns generated inside the microfluidic channel, we demonstrated the generation of concentration gradients of chemical as a result of serial mixing of different solutions. By controlling the driving voltage of piezoelectric transducer, the generation of spatially controllable chemical gradient profiles were demonstrated. Furthermore, through the modulation of the actuation time of piezoelectric transducer, we generated temporally controllable chemical gradients. With these two characteristics combined, our sharp-edge-based acoustofluidic gradient generator could generate spatiotemporally controllable concentration gradients. The biocompatibility of our sharp-edge-based acoustofluidic gradient generator was validated by carrying out experiments where cells migrated in response to the concentration gradient generated by our gradient generator, and by preserving the cell viability after long-term exposure to an acoustic field. Our device features advantages such as simple fabrication and operation, compact and biocompatible device, and generation of spatiotemporally tunable gradients.

Reliable, programmable fluid pumping

Fluid pumping is another vital function needed for the development of integrated LOC devices. Expanding the potential of acoustic streaming induced by oscillating sharp-edge structure, we developed a programmable acoustofluidic micropump that utilizes the acoustic streaming generated by acoustically oscillating sharp-edge structures. To achieve this, we engineered the geometry of sharp-edge structure, specifically, tilted the sharp-edge structure, which in turn, varies the acoustic streaming patterns generated inside the channel. This altered streaming pattern then produced a net force pointing toward the direction where the sharp-edge structure was tilted; fluid pumping motion occurred because of the net force, along the parallel direction where the sharp-edge structure was tilted. The effect of the sharp-edge structures with different tilting angles on the pumping performance was investigated and characterized. The developed sharp-edge-based acoustofluidic micropump was capable of generating stable flow rates as high as $8 \mu\text{L}/\text{min}$ with a pumping pressure of $\sim 76 \text{ Pa}$, and was able to modulate flow rates across a wide range, from several nanoliters to several microliters per minute. Furthermore, by programming the input signal to the piezoelectric transducer, our sharp-edge-based acoustofluidic micropump could modulate the profiles of the pumping flow rates. Our sharp-edge-based acoustofluidic micropump offers advantages over other microfluidic pumps in terms of not only simplicity, stability, reliability, and cost-effectiveness but also controllability and flexibility, which, when combined, make it valuable in many lab-on-a-chip applications.

7.2 Prospects

This dissertation has centered on the development of a series of acoustofluidic devices that are capable of manipulating fluids, specifically, based on the acoustic streaming effect induced by the oscillating sharp-edge structures. Despite the successful development and demonstration on these devices, the work has been highly experimental, and that, to a large extent, is because the topic contains uncovered matters, particularly in its physics and mechanisms. Meanwhile, the work has also opened a field for further fundamental studies on streaming patterns, establishment of numerical models, as well as other microfluidic applications. A lot of

tasks have to be done before we can fully expand the capability of sharp-edge-based acoustofluidic devices.

Firstly, fundamental studies including basic physics and mechanisms have yet to be explored and understood on how acoustic streaming is actually induced around oscillating sharp-edge structures. Though we can generate acoustic streaming around oscillating sharp-edge structure and then use them to demonstrate different applications; however, the work is still of qualitative because the physics and mechanisms is yet unclear. We will need to take one step back to the fundamental studies. Once the physics and mechanisms are well understood, we are able to properly design sharp-edge-based devices to avoid the unnecessary loss of acoustic energy; in other words, the devices can perform better than before.

Another pressing task is to establish a numerical model that is applicable for the devices constructed with sharp-edge structures of different geometries and arrangements. The numerical model should be able to produce simulation results that are in good agreement with experimental results. Once the numerical model is established and based upon the simulation results it provides, we should be able to predict the performance of the device of interest and as such, before we come to the step of fabricating device, we can modify the device numerically until we get an optimized device design. Doing this will significantly shorten our time on experimentally testing devices with different designs.

Thirdly, further integration of different devices has to be done. In this dissertation, we have demonstrated a series of sharp-edge-based acoustofluidic devices for fluid mixing and pumping; however, each single device has only one function. To enable the future development of fully-functioning LOC device, device-to-device integration is inevitable and as a result, the integrability of each of our differently-purposed devices has to be proved. To prove so, we will integrate only one single-function device with another at a time; for example, our sharp-edge-based micromixer may be first integrated with our sharp-edge-based micropump to enable concurrent fluid mixing-pumping in a single device. Once it is achieved, we will take one step further, namely, integrate the concurrent mixing-pumping device with another on-chip component (*e.g.*, detection/sensing component), to demonstrate applications such as on-chip immunosensing.

Finally, the acoustic streaming effect induced by oscillating sharp-edge structures have been proved to be extremely useful and powerful for fluid mixing and

pumping; however, there are many applications that can also be achieved using acoustic streaming including, but not limited to, particle/cell trapping and enrichment, size-based particle/cell separation, cell lysis, cell mechanotransduction (shear-stress stimulation). Furthermore, we can even integrate existing microfluidic devices with our sharp-edge-based micropump to enable even versatile applications, such as pumpless cell separation and pumpless droplet generation. Along the line, we truly believe more and more applications will be enabled by sharp-edge-based acoustofluidic devices, and we are confident that sharp-edge-based acoustofluidic devices will become powerful microfluidic tools.

Bibliography

- [1] J. Lighthill, “Acoustic streaming,” *Journal of sound and vibration*, vol. 61, no. 3, pp. 391–418, 1978.
- [2] N. Riley, “Steady streaming,” *Annual Review of Fluid Mechanics*, vol. 33, no. 1, pp. 43–65, 2001.
- [3] M. Wiklund, R. Green, and M. Ohlin, “Acoustofluidics 14: Applications of acoustic streaming in microfluidic devices,” *Lab on a Chip*, vol. 12, no. 14, pp. 2438–2451, 2012.
- [4] P. M. Tribler, *Acoustic streaming in microchannels*. PhD thesis, Technical University of Denmark, Denmark, 2012.
- [5] W. L. Nyborg, “Innovation and intellectual property rights,” in *Nonlinear Acoustics* (M. F. Hamilton and D. T. Blackstock, eds.), pp. 207–231, San Diego, CA: Academic Press, 1998.
- [6] H. J. Schlichting, “Die unendlichkeit ist grün,” *Physik in unserer Zeit*, vol. 41, no. 6, pp. 306–306, 2010.
- [7] L. Rayleigh, “On the circulation of air observed in kundt’s tubes, and on some allied acoustical problems,” *Philosophical Transactions of the Royal Society of London*, vol. 175, pp. 1–21, 1884.
- [8] W. L. Nyborg, “Acoustic streaming near a boundary,” *The Journal of the Acoustical Society of America*, vol. 30, no. 4, pp. 329–339, 1958.
- [9] R. H. Liu, J. Yang, M. Z. Pindera, M. Athavale, and P. Grodzinski, “Bubble-induced acoustic micromixing,” *Lab on a chip*, vol. 2, pp. 151–7, aug 2002.
- [10] A. R. Tovar and A. P. Lee, “Lateral cavity acoustic transducer,” *Lab on a chip*, vol. 9, pp. 41–3, jan 2009.
- [11] D. Ahmed, X. Mao, B. K. Juluri, and T. J. Huang, “A fast microfluidic mixer based on acoustically driven sidewall-trapped microbubbles,” *Microfluidics and Nanofluidics*, vol. 7, pp. 727–731, apr 2009.

- [12] D. Ahmed, X. Mao, J. Shi, B. K. Juluri, and T. J. Huang, “A millisecond micromixer via single-bubble-based acoustic streaming.,” *Lab on a chip*, vol. 9, pp. 2738–41, sep 2009.
- [13] K. Ryu, S. K. Chung, and S. K. Cho, “Micropumping by an acoustically excited oscillating bubble for automated implantable microfluidic devices,” *Journal of the Association for Laboratory Automation*, vol. 15, no. 3, pp. 163–171, 2010.
- [14] A. R. Tovar, M. V. Patel, and A. P. Lee, “Lateral air cavities for microfluidic pumping with the use of acoustic energy,” *Microfluidics and Nanofluidics*, vol. 10, pp. 1269–1278, jan 2011.
- [15] W.-F. Fang and A. P. Lee, “Lcat pump optimization for an integrated microfluidic droplet generator,” *Microfluidics and Nanofluidics*, vol. 18, no. 5-6, pp. 1265–1275, 2015.
- [16] P. Rogers and A. Neild, “Selective particle trapping using an oscillating microbubble.,” *Lab on a chip*, vol. 11, pp. 3710–5, nov 2011.
- [17] C. Wang, S. V. Jalikop, and S. Hilgenfeldt, “Size-sensitive sorting of microparticles through control of flow geometry,” *Applied Physics Letters*, vol. 99, no. 3, p. 034101, 2011.
- [18] C. Wang, S. V. Jalikop, and S. Hilgenfeldt, “Efficient manipulation of microparticles in bubble streaming flows.,” *Biomicrofluidics*, vol. 6, pp. 12801–1280111, mar 2012.
- [19] R. Thameem, B. Rallabandi, and S. Hilgenfeldt, “Particle migration and sorting in microbubble streaming flows,” *Biomicrofluidics*, vol. 10, no. 1, p. 014124, 2016.
- [20] M. V. Patel, A. R. Tovar, and A. P. Lee, “Lateral cavity acoustic transducer as an on-chip cell/particle microfluidic switch.,” *Lab on a chip*, vol. 12, pp. 139–45, jan 2012.
- [21] M. V. Patel, I. A. Nanayakkara, M. G. Simon, and A. P. Lee, “Cavity-induced microstreaming for simultaneous on-chip pumping and size-based separation of cells and particles,” *Lab on a Chip*, vol. 14, no. 19, pp. 3860–3872, 2014.
- [22] S. K. Chung and S. K. Cho, “On-chip manipulation of objects using mobile oscillating bubbles,” *Journal of Micromechanics and Microengineering*, vol. 18, no. 12, p. 125024, 2008.
- [23] S. K. Chung and S. K. Cho, “3-d manipulation of millimeter-and micro-sized objects using an acoustically excited oscillating bubble,” *Microfluidics and nanofluidics*, vol. 6, no. 2, pp. 261–265, 2009.

- [24] K. H. Lee, J. H. Lee, J. M. Won, K. Rhee, and S. K. Chung, “Micromanipulation using cavitation microstreaming generated by acoustically oscillating twin bubbles,” *Sensors and Actuators A: Physical*, vol. 188, pp. 442–449, 2012.
- [25] P. Marmottant and S. Hilgenfeldt, “Controlled vesicle deformation and lysis by single oscillating bubbles.,” *Nature*, vol. 423, pp. 153–6, may 2003.
- [26] P.-H. Huang, M. Ian Lapsley, D. Ahmed, Y. Chen, L. Wang, and T. Jun Huang, “A single-layer, planar, optofluidic switch powered by acoustically driven, oscillating microbubbles.,” *Applied physics letters*, vol. 101, p. 141101, oct 2012.
- [27] V. H. Lieu, T. a. House, and D. T. Schwartz, “Hydrodynamic Tweezers: Impact of Design Geometry on Flow and Microparticle Trapping.,” *Analytical chemistry*, vol. 84, pp. 1963–1968, feb 2012.
- [28] T. A. House, V. H. Lieu, and D. T. Schwartz, “A model for inertial particle trapping locations in hydrodynamic tweezers arrays,” *Journal of Micromechanics and Microengineering*, vol. 24, no. 4, p. 045019, 2014.
- [29] B. R. Lutz, J. Chen, and D. T. Schwartz, “Microfluidics without microfabrication.,” *Proceedings of the National Academy of Sciences of the United States of America*, vol. 100, pp. 4395–8, apr 2003.
- [30] B. R. Lutz, J. Chen, and D. T. Schwartz, “Microscopic steady streaming eddies created around short cylinders in a channel: Flow visualization and Stokes layer scaling,” *Physics of Fluids*, vol. 17, no. 2, p. 023601, 2005.
- [31] B. R. Lutz, J. Chen, and D. T. Schwartz, “Characterizing homogeneous chemistry using well-mixed microeddies.,” *Analytical chemistry*, vol. 78, pp. 1606–12, mar 2006.
- [32] B. R. Lutz, J. Chen, and D. T. Schwartz, “Hydrodynamic Tweezers : 1 . Noncontact Trapping of Single Cells Using Steady Streaming Microeddies ability to gently position cells for repeated measurements,” *Methods*, vol. 78, no. 15, pp. 5429–5435, 2006.
- [33] M. E. Gurtin, E. Fried, and L. Anand, *The mechanics and thermodynamics of continua*. Cambridge University Press, 2010.
- [34] S. S. Sadhal, “Acoustofluidics 13: Analysis of acoustic streaming by perturbation methods,” *Lab on a Chip*, vol. 12, no. 13, pp. 2292–2300, 2012.
- [35] N. Nama, P.-H. Huang, T. J. Huang, and F. Costanzo, “Investigation of micromixing by acoustically oscillated sharp-edges,” *Biomicrofluidics*, vol. 10, no. 2, p. 024124, 2016.

- [36] T. Frommelt, D. Gogel, M. Kostur, P. Talkner, P. Hänggi, and A. Wixforth, “Flow patterns and transport in rayleigh surface acoustic wave streaming: Combined finite element method and raytracing numerics versus experiments,” *Ultrasonics, Ferroelectrics, and Frequency Control, IEEE Transactions on*, vol. 55, no. 10, pp. 2298–2305, 2008.
- [37] X. Ding, P. Li, S.-C. S. Lin, Z. S. Stratton, N. Nama, F. Guo, D. Slotcavage, X. Mao, J. Shi, F. Costanzo, and T. J. Huang, “Surface acoustic wave microfluidics.,” *Lab on a chip*, vol. 13, pp. 3626–49, sep 2013.
- [38] N. Nama, P.-H. Huang, T. J. Huang, and F. Costanzo, “Investigation of acoustic streaming patterns around oscillating sharp edges,” *Lab on a chip*, vol. 14, pp. 2824–2836, jun 2014.
- [39] D. Käuster, *Numerical simulation of acoustic streaming on SAW-driven biochips*. PhD thesis, Universität Augsburg, Germany, 2006.
- [40] J. Stuart, “Double boundary layers in oscillatory viscous flow,” *Journal of Fluid Mechanics*, vol. 24, no. 04, pp. 673–687, 1966.
- [41] C. Bradley, “Acoustic streaming field structure: The influence of the radiator,” *The Journal of the Acoustical Society of America*, vol. 100, no. 3, pp. 1399–1408, 1996.
- [42] P. B. Muller, R. Barnkob, M. J. H. Jensen, and H. Bruus, “A numerical study of microparticle acoustophoresis driven by acoustic radiation forces and streaming-induced drag forces,” *Lab on a Chip*, vol. 12, no. 22, pp. 4617–4627, 2012.
- [43] M. Settnes and H. Bruus, “Forces acting on a small particle in an acoustical field in a viscous fluid,” *Physical Review E*, vol. 85, no. 1, p. 016327, 2012.
- [44] R. Barnkob, *Physics of microparticle acoustophoresis: Bringing theory and experiment*. PhD thesis, Technical University of Denmark, Denmark, 2012.
- [45] L. K. Zarembo, “Acoustic streaming,” in *High-intensity ultrasonic fields* (L. Rozenberg, ed.), pp. 135–199, Springer, 1971.
- [46] O. Bühler, *Waves and Mean Flows*. Cambridge University Press, 2009.
- [47] J. Vanneste and O. Bühler, “Streaming by leaky surface acoustic waves,” in *Proceedings of the Royal Society of London A: Mathematical, Physical and Engineering Sciences*, vol. 467, pp. 1779–1800, The Royal Society, 2011.
- [48] W. Bangerth, R. Hartmann, and G. Kanschat, “deal.ii – A general-purpose object-oriented finite element library,” *ACM Transactions on Mathematical Software (TOMS)*, vol. 33, no. 4, p. 24, 2007.

- [49] W. Bangerth, R. Hartmann, and G. Kanschat, “deal. ii differential equations analysis library” technical reference, 1998–2006.”
- [50] P.-H. Huang, Y. Xie, D. Ahmed, J. Rufo, N. Nama, Y. Chen, C. Y. Chan, and T. J. Huang, “An acoustofluidic micromixer based on oscillating sidewall sharp-edges,” *Lab on a chip*, vol. 13, pp. 3847–3852, oct 2013.
- [51] L. Pollack, M. W. Tate, N. C. Darnton, J. B. Knight, S. M. Gruner, W. a. Eaton, and R. H. Austin, “Compactness of the denatured state of a fast-folding protein measured by submillisecond small-angle x-ray scattering,” *Proceedings of the National Academy of Sciences*, vol. 96, pp. 10115–10117, aug 1999.
- [52] Y. Xie, D. Ahmed, M. I. Lapsley, S.-C. S. Lin, A. A. Nawaz, L. Wang, and T. J. Huang, “Single-shot characterization of enzymatic reaction constants K_m and k_{cat} by an acoustic-driven, bubble-based fast micromixer,” *Analytical chemistry*, vol. 84, pp. 7495–501, sep 2012.
- [53] J. DeMello and A. DeMello, “Microscale reactors: nanoscale products,” *Lab on a Chip*, vol. 4, no. 2, p. 11N, 2004.
- [54] L.-H. Hung, S.-Y. Teh, J. Jester, and A. P. Lee, “PLGA micro/nanosphere synthesis by droplet microfluidic solvent evaporation and extraction approaches,” *Lab on a chip*, vol. 10, pp. 1820–5, jul 2010.
- [55] C.-m. Ho and Y.-c. Tai, “REVIEW : MEMS and Its Applications for Flow Control,” *Journal of Fluids Engineering*, vol. 118, pp. 437–447, 1996.
- [56] G. M. Whitesides, “The origins and the future of microfluidics,” *Nature*, vol. 442, pp. 368–73, jul 2006.
- [57] N.-T. Nguyen and Z. Wu, “Micromixers—a review,” *Journal of Micromechanics and Microengineering*, vol. 15, pp. R1–R16, feb 2005.
- [58] H. Song and R. F. Ismagilov, “Millisecond kinetics on a microfluidic chip using nanoliters of reagents,” *Journal of the American Chemical Society*, vol. 125, pp. 14613–9, nov 2003.
- [59] E. M. Miller and A. R. Wheeler, “Digital bioanalysis,” *Analytical and bioanalytical chemistry*, vol. 393, pp. 419–26, jan 2009.
- [60] C.-H. Hsu and A. Folch, “Spatio-temporally-complex concentration profiles using a tunable chaotic micromixer,” *Applied Physics Letters*, vol. 89, no. 14, p. 144102, 2006.

- [61] J. Knight, A. Vishwanath, J. Brody, and R. Austin, "Hydrodynamic Focusing on a Silicon Chip: Mixing Nanoliters in Microseconds," *Physical Review Letters*, vol. 80, pp. 3863–3866, apr 1998.
- [62] T.-H. Wang, Y. Peng, C. Zhang, P. K. Wong, and C.-M. Ho, "Single-molecule tracing on a fluidic microchip for quantitative detection of low-abundance nucleic acids.," *Journal of the American Chemical Society*, vol. 127, pp. 5354–9, apr 2005.
- [63] M. Sigurdson, D. Wang, and C. D. Meinhart, "Electrothermal stirring for heterogeneous immunoassays.," *Lab on a chip*, vol. 5, pp. 1366–73, dec 2005.
- [64] J. T. Coleman, J. McKechnie, and D. Sinton, "High-efficiency electrokinetic micromixing through symmetric sequential injection and expansion.," *Lab on a chip*, vol. 6, pp. 1033–9, aug 2006.
- [65] C. K. Harnett, J. Templeton, K. a. Dunphy-Guzman, Y. M. Senousy, and M. P. Kanouff, "Model based design of a microfluidic mixer driven by induced charge electroosmosis.," *Lab on a chip*, vol. 8, pp. 565–72, apr 2008.
- [66] C. Neils, Z. Tyree, B. Finlayson, and A. Folch, "Combinatorial mixing of microfluidic streams.," *Lab on a chip*, vol. 4, pp. 342–50, aug 2004.
- [67] T. W. Lim, Y. Son, Y. J. Jeong, D.-Y. Yang, H.-J. Kong, K.-S. Lee, and D.-P. Kim, "Three-dimensionally crossing manifold micro-mixer for fast mixing in a short channel length.," *Lab on a chip*, vol. 11, pp. 100–3, jan 2011.
- [68] K. S. Ryu, K. Shaikh, E. Goluch, Z. Fan, and C. Liu, "Micro magnetic stir-bar mixer integrated with parylene microfluidic channels.," *Lab on a chip*, vol. 4, pp. 608–13, dec 2004.
- [69] G.-P. Zhu and N.-T. Nguyen, "Rapid magnetofluidic mixing in a uniform magnetic field.," *Lab on a chip*, vol. 12, pp. 4772–80, nov 2012.
- [70] J.-h. Tsai and L. Lin, "Active microfluidic mixer and gas bubble filter driven by thermal bubble micropump," *Sensors and Actuators A: Physical*, vol. 97–98, pp. 665–671, apr 2002.
- [71] A. N. Hellman, K. R. Rau, H. H. Yoon, S. Bae, J. F. Palmer, K. S. Phillips, N. L. Allbritton, and V. Venugopalan, "Laser-induced mixing in microfluidic channels.," *Analytical chemistry*, vol. 79, pp. 4484–92, jun 2007.
- [72] S.-C. S. Lin, X. Mao, and T. J. Huang, "Surface acoustic wave (SAW) acoustophoresis: now and beyond.," *Lab on a chip*, vol. 12, pp. 2766–70, aug 2012.

- [73] A. R. Rezk, A. Qi, J. R. Friend, W. H. Li, and L. Y. Yeo, “Uniform mixing in paper-based microfluidic systems using surface acoustic waves.,” *Lab on a chip*, vol. 12, pp. 773–9, feb 2012.
- [74] W.-K. Tseng, J.-L. Lin, W.-C. Sung, S.-H. Chen, and G.-B. Lee, “Active micro-mixers using surface acoustic waves on Y-cut 128Å LiNbO₃,” *Journal of Micromechanics and Microengineering*, vol. 16, pp. 539–548, mar 2006.
- [75] A. Wixforth, C. Strobl, C. Gauer, A. Toegl, J. Scriba, and Z. v Guttenberg, “Acoustic manipulation of small droplets.,” *Analytical and bioanalytical chemistry*, vol. 379, pp. 982–91, aug 2004.
- [76] T. Frommelt, M. Kostur, M. Wenzel-Schäfer, P. Talkner, P. Hänggi, and A. Wixforth, “Microfluidic Mixing via Acoustically Driven Chaotic Advection,” *Physical Review Letters*, vol. 100, p. 034502, jan 2008.
- [77] G. G. Yaralioglu, I. O. Wygant, T. C. Marentis, and B. T. Khuri-Yakub, “Ultrasonic mixing in microfluidic channels using integrated transducers.,” *Analytical chemistry*, vol. 76, pp. 3694–8, jul 2004.
- [78] K. Sritharan, C. J. Strobl, M. F. Schneider, A. Wixforth, and Z. Guttenberg, “Acoustic mixing at low Reynold’s numbers,” *Applied Physics Letters*, vol. 88, no. 5, p. 054102, 2006.
- [79] H. Yu, J. Kwon, and E. Kim, “Microfluidic Mixer and Transporter Based on PZT Self-Focusing Acoustic Transducers,” *Journal of Microelectromechanical Systems*, vol. 15, pp. 1015–1024, aug 2006.
- [80] Z. Yang, S. Matsumoto, H. Goto, M. Matsumoto, and R. Maeda, “Ultrasonic micromixer for microfluidic systems,” *Sensors and Actuators A: Physical*, vol. 93, pp. 266–272, oct 2001.
- [81] S. Oberti, A. Neild, and T. W. Ng, “Microfluidic mixing under low frequency vibration,” *Lab on a Chip*, vol. 9, no. 10, pp. 1435–1438, 2009.
- [82] K. Rodaree, T. Maturros, S. Chaotheing, T. Pogfay, N. Suwanakitti, C. Wongsombat, K. Jaruwongrungrunsee, A. Wisitsoraat, S. Kamchonwongpaisan, T. Lomas, and A. Tuantranont, “DNA hybridization enhancement using piezoelectric microagitation through a liquid coupling medium.,” *Lab on a chip*, vol. 11, pp. 1059–64, mar 2011.
- [83] D. Ahmed, C. Y. Chan, S.-C. S. Lin, H. S. Muddana, N. Nama, S. J. Benkovic, and T. J. Huang, “Tunable, pulsatile chemical gradient generation via acoustically driven oscillating bubbles.,” *Lab on a chip*, vol. 13, pp. 328–31, feb 2013.

- [84] A. Hashmi, G. Yu, M. Reilly-Collette, G. Heiman, and J. Xu, "Oscillating bubbles: a versatile tool for lab on a chip applications.," *Lab on a chip*, vol. 12, pp. 4216–27, nov 2012.
- [85] P. Garstecki, M. J. Fuerstman, M. A. Fischbach, S. K. Sia, and G. M. Whitesides, "Mixing with bubbles: a practical technology for use with portable microfluidic devices," *Lab on a Chip*, vol. 6, no. 2, pp. 207–212, 2006.
- [86] P.-H. Huang, L. Ren, N. Nama, S. Li, P. Li, X. Yao, R. a. Cuento, C.-H. Wei, Y. Chen, Y. Xie, A. A. Nawaz, Y. G. Alevy, M. J. Holtzman, J. P. McCoy, S. J. Levine, and T. J. Huang, "An acoustofluidic sputum liquefier," *Lab on a Chip*, vol. 15, no. 15, pp. 3125–3131, 2015.
- [87] S. Vidal, J. Bellido-Casado, C. Granel, A. Crespo, V. Plaza, and C. Juárez, "Flow cytometry analysis of leukocytes in induced sputum from asthmatic patients," *Immunobiology*, vol. 217, no. 7, pp. 692–697, 2012.
- [88] J. L. Simpson, R. Scott, M. J. Boyle, and P. G. Gibson, "Inflammatory subtypes in asthma: Assessment and identification using induced sputum," *Respirology*, vol. 11, no. 1, pp. 54–61, 2006.
- [89] R. McNerney, M. Maeurer, I. Abubakar, B. Marais, T. D. McHugh, N. Ford, K. Weyer, S. Lawn, M. P. Grobusch, Z. Memish, S. B. Squire, G. Pantaleo, J. Chakaya, M. Casenghi, G. B. Migliori, P. Mwaba, L. Zijenah, M. Hoelscher, H. Cox, S. Swaminathan, P. S. Kim, M. Schito, A. Harari, M. Bates, S. Schwank, J. O'Grady, M. Pletschette, L. Ditui, R. Atun, and A. Zumla, "Tuberculosis diagnostics and biomarkers: Needs, challenges, recent advances, and opportunities," *Journal of Infectious Diseases*, vol. 205, no. SUPPL. 2, pp. S147–158, 2012.
- [90] A. Zumla, P. Nahid, and S. T. Cole, "Advances in the development of new tuberculosis drugs and treatment regimens.," *Nature reviews. Drug discovery*, vol. 12, no. 5, pp. 388–404, 2013.
- [91] X. Fang, H. Chen, L. Xu, X. Jiang, W. Wu, and J. Kong, "A portable and integrated nucleic acid amplification microfluidic chip for identifying bacteria.," *Lab on a chip*, mar 2012.
- [92] L.-Y. Hung, T.-B. Huang, Y.-C. Tsai, C.-S. Yeh, H.-Y. Lei, and G.-B. Lee, "A microfluidic immunomagnetic bead-based system for the rapid detection of influenza infections: From purified virus particles to clinical specimens," *Biomedical Microdevices*, vol. 15, no. 3, pp. 539–551, 2013.
- [93] D. Kim and C. L. Haynes, "Neutrophil chemotaxis within a competing gradient of chemoattractants.," *Analytical chemistry*, vol. 84, pp. 6070–8, jul 2012.

- [94] M. Liong, M. Fernandez-Suarez, D. Issadore, C. Min, C. Tassa, T. Reiner, S. M. Fortune, M. Toner, H. Lee, and R. Weissleder, “Specific pathogen detection using bioorthogonal chemistry and diagnostic magnetic resonance,” *Bioconjugate Chemistry*, vol. 22, no. 12, pp. 2390–2394, 2011.
- [95] M. Liong, A. N. Hoang, J. Chung, N. Gural, C. B. Ford, C. Min, R. R. Shah, R. Ahmad, M. Fernandez-Suarez, S. M. Fortune, M. Toner, H. Lee, and R. Weissleder, “Magnetic barcode assay for genetic detection of pathogens.,” *Nature communications*, vol. 4, p. 1752, 2013.
- [96] P.-H. Huang, N. Nama, Z. Mao, P. Li, J. Rufo, Y. Chen, Y. Xie, C.-H. Wei, L. Wang, and T. J. Huang, “A reliable and programmable acoustofluidic pump powered by oscillating sharp-edge structures,” *Lab on a chip*, vol. 14, no. 22, pp. 4319–4323, 2014.
- [97] A. Efthimiadis, A. Spanevello, Q. Hamid, M. M. Kelly, M. Linden, R. Louis, M. M. M. Pizzichini, E. Pizzichini, C. Ronchi, F. Van Overvel, and R. Djukanović, “Methods of sputum processing for cell counts, immunocytochemistry and in situ hybridisation.,” *The European respiratory journal. Supplement*, vol. 37, pp. 19s–23s, 2002.
- [98] S. K. Lai, Y. Y. Wang, D. Wirtz, and J. Hanes, “Micro- and macrorheology of mucus,” *Advanced Drug Delivery Reviews*, vol. 61, no. 2, pp. 86–100, 2009.
- [99] J. Beier, K. M. Beeh, O. Kornmann, and R. Buhl, “Induced sputum methodology: Validity and reproducibility of total glutathione measurement in supernatant of healthy and asthmatic individuals,” *Journal of Laboratory and Clinical Medicine*, vol. 144, no. 1, pp. 38–44, 2004.
- [100] I. S. Woolhouse, D. L. Bayley, and R. A. Stockley, “Effect of sputum processing with dithiothreitol on the detection of inflammatory mediators in chronic bronchitis and bronchiectasis.,” *Thorax*, vol. 57, no. 8, pp. 667–671, 2002.
- [101] P.-H. Huang, C. Y. Chan, P. Li, N. Nama, Y. Xie, C.-H. Wei, Y. Chen, D. Ahmed, and T. J. Huang, “A spatiotemporally controllable chemical gradient generator via acoustically oscillating sharp-edge structures,” *Lab on a Chip*, vol. 15, no. 21, pp. 4166–4176, 2015.
- [102] E. K. Sackmann, A. L. Fulton, and D. J. Beebe, “The present and future role of microfluidics in biomedical research.,” *Nature*, vol. 507, no. 7491, pp. 181–189, 2014.
- [103] E. Berthier and D. J. Beebe, “Gradient generation platforms: new directions for an established microfluidic technology.,” *Lab on a chip*, vol. 12, pp. 3241–3247, 2014.

- [104] S. Kim, H. J. Kim, and N. L. Jeon, “Biological applications of microfluidic gradient devices.,” *Integrative biology*, vol. 2, pp. 584–603, nov 2010.
- [105] T. M. Keenan and A. Folch, “Biomolecular gradients in cell culture systems.,” *Lab on a chip*, vol. 8, no. 1, pp. 34–57, 2008.
- [106] D. Irimia, “Microfluidic technologies for temporal perturbations of chemotaxis.,” *Annual review of biomedical engineering*, vol. 12, pp. 259–284, 2010.
- [107] A. Ainla, E. T. Jansson, N. Stepanyants, O. Orwar, and A. Jesorka, “A microfluidic pipette for single-cell pharmacology,” *Analytical Chemistry*, vol. 82, no. 11, pp. 4529–4536, 2010.
- [108] J. van Zon, M. Barkoulas, and A. van Oudenaarden, “Cells change their sensitivity to an EGF morphogen gradient to control EGF-induced gene expression.,” *Nature communications*, vol. 6, no. May, pp. 1–11, 2014.
- [109] D. Jowhar, G. Wright, P. C. Samson, J. P. Wikswo, and C. Janetopoulos, “Open access microfluidic device for the study of cell migration during chemotaxis.,” *Integrative biology*, vol. 2, no. 11-12, pp. 648–658, 2010.
- [110] T. S. Shimizu, Y. Tu, and H. C. Berg, “A modular gradient-sensing network for chemotaxis in *Escherichia coli* revealed by responses to time-varying stimuli.,” *Molecular systems biology*, vol. 6, no. 382, p. 382, 2010.
- [111] N. L. Jeon, H. Baskaran, S. K. W. Dertinger, G. M. Whitesides, L. Van de Water, and M. Toner, “Neutrophil chemotaxis in linear and complex gradients of interleukin-8 formed in a microfabricated device.,” *Nature biotechnology*, vol. 20, pp. 826–830, aug 2002.
- [112] A. Nakajima, S. Ishihara, D. Imoto, and S. Sawai, “Rectified directional sensing in long-range cell migration,” *Nature Communications*, vol. 5, p. 5367, 2014.
- [113] B. Meier, A. Zielinski, C. Weber, D. Arcizet, S. Youssef, T. Franosch, J. O. Rädler, and D. Heinrich, “Chemotactic cell trapping in controlled alternating gradient fields.,” *Proceedings of the National Academy of Sciences of the United States of America*, vol. 108, pp. 11417–11422, jul 2011.
- [114] A. Shamloo, M. Heibatollahi, and M. R. K. Mofrad, “Directional migration and differentiation of neural stem cells within three-dimensional microenvironments,” *Integrative biology*, vol. 7, pp. 335–344, 2015.
- [115] J. Park, I. C. Kim, J. Baek, M. Cha, J. Kim, S. Park, J. Lee, and B. Kim, “Micro pumping with cardiomyocyte-polymer hybrid.,” *Lab on a chip*, vol. 7, pp. 1367–70, oct 2007.

- [116] B. G. Chung, L. a. Flanagan, S. W. Rhee, P. H. Schwartz, A. P. Lee, E. S. Monuki, and N. L. Jeon, "Human neural stem cell growth and differentiation in a gradient-generating microfluidic device.," *Lab on a chip*, vol. 5, pp. 401–406, apr 2005.
- [117] S. J. Wang, W. Saadi, F. Lin, C. Minh-Canh Nguyen, and N. Li Jeon, "Differential effects of EGF gradient profiles on MDA-MB-231 breast cancer cell chemotaxis," *Experimental Cell Research*, vol. 300, no. 1, pp. 180–189, 2004.
- [118] B. Lin, T. Yin, Y. I. Wu, T. Inoue, and A. Levchenko, "Interplay between chemotaxis and contact inhibition of locomotion determines exploratory cell migration," *Nature Communications*, vol. 6, p. 6619, 2015.
- [119] S. Boyden, "The Chemotactic Effect of Mixtures of Antibody and Antigen on Polymorphonuclear Leucocytes," *The Journal of experimental medicine*, vol. 115, pp. 453–466, 1962.
- [120] S. H. Zigmond, "Ability of polymorphonuclear leukocytes to orient in gradients of chemotactic factors," *The Journal of Cell Biology*, vol. 75, pp. 606–616, 1977.
- [121] D. Zicha, G. a. Dunn, and a. F. Brown, "A new direct-viewing chemotaxis chamber.," *Journal of cell science*, vol. 99 (Pt 4), pp. 769–775, 1991.
- [122] R. W. Gundersen and J. N. Barrett, "Neuronal chemotaxis: chick dorsal-root axons turn toward high concentrations of nerve growth factor.," *Science (New York, N.Y.)*, vol. 206, no. 4422, pp. 1079–1080, 1979.
- [123] H. Song, G. Ming, Z. He, M. Lehmann, L. McKerracher, M. Tessier-Lavigne, and M. Poo, "Conversion of neuronal growth cone responses from repulsion to attraction by cyclic nucleotides.," *Science (New York, N.Y.)*, vol. 281, no. 5382, pp. 1515–1518, 1998.
- [124] F. Lin, W. Saadi, S. W. Rhee, S.-J. Wang, S. Mittal, and N. L. Jeon, "Generation of dynamic temporal and spatial concentration gradients using microfluidic devices.," *Lab on a chip*, vol. 4, pp. 164–167, jun 2004.
- [125] D. Irimia, S.-Y. Liu, W. G. Tharp, A. Samadani, M. Toner, and M. C. Poznansky, "Microfluidic system for measuring neutrophil migratory responses to fast switches of chemical gradients.," *Lab on a chip*, vol. 6, pp. 191–198, feb 2006.
- [126] T. M. Keenan, C. H. Hsu, and A. Folch, "Microfluidic "jets" for generating steady-state gradients of soluble molecules on open surfaces," *Applied Physics Letters*, vol. 89, no. 11, p. 114103, 2006.

- [127] B. G. Chung, F. Lin, and N. L. Jeon, “A microfluidic multi-injector for gradient generation.,” *Lab on a chip*, vol. 6, no. 6, pp. 764–768, 2006.
- [128] B. Mosadegh, C. Huango, J. W. Park, H. S. Shin, B. G. Chung, S. K. Hwang, K. H. Lee, H. J. Kim, J. Brody, and N. L. Jeon, “Generation of stable complex gradients across two-dimensional surfaces and three-dimensional gels,” *Langmuir*, vol. 23, no. 22, pp. 10910–10912, 2007.
- [129] A. Shamloo, N. Ma, M.-M. Poo, L. L. Sohn, and S. C. Heilshorn, “Endothelial cell polarization and chemotaxis in a microfluidic device.,” *Lab on a chip*, vol. 8, no. 8, pp. 1292–1299, 2008.
- [130] S. K. W. Dertinger, D. T. Chiu, N. L. Jeon, and G. M. Whitesides, “Generation of Gradients Having Complex Shapes Using Microfluidic Networks,” *Analytical Chemistry*, vol. 73, pp. 1240–1246, mar 2001.
- [131] N. L. Jeon, S. K. W. Dertinger, D. T. Chiu, I. S. Choi, A. D. Stroock, and G. M. Whitesides, “Generation of Solution and Surface Gradients Using Microfluidic Systems,” *Langmuir*, vol. 16, pp. 8311–8316, oct 2000.
- [132] H. Wu, B. Huang, and R. N. Zare, “Generation of complex, static solution gradients in microfluidic channels,” *Journal of the American Chemical Society*, vol. 128, no. 13, pp. 4194–4195, 2006.
- [133] J. Atencia, J. Morrow, and L. E. Locascio, “The microfluidic palette: a diffusive gradient generator with spatio-temporal control.,” *Lab on a chip*, vol. 9, no. 18, pp. 2707–2714, 2009.
- [134] K. Hattori, S. Sugiura, and T. Kanamori, “Generation of arbitrary monotonic concentration profiles by a serial dilution microfluidic network composed of microchannels with a high fluidic-resistance ratio.,” *Lab on a chip*, vol. 9, no. 12, pp. 1763–1772, 2009.
- [135] G. Destgeer, S. Im, B. Hang Ha, J. Ho Jung, M. Ahmad Ansari, and H. Jin Sung, “Adjustable, rapidly switching microfluidic gradient generation using focused travelling surface acoustic waves,” *Applied Physics Letters*, vol. 104, no. 2, p. 023056, 2014.
- [136] H. Bruus, “Acoustofluidics 2: Perturbation theory and ultrasound resonance modes,” *Lab on a Chip*, vol. 12, no. 1, pp. 20–28, 2012.
- [137] I. Iranmanesh, R. Barnkob, H. Bruus, and M. Wiklund, “Tunable-angle wedge transducer for improved acoustophoretic control in a microfluidic chip,” *Journal of Micromechanics and Microengineering*, vol. 23, no. 10, p. 105002, 2013.

- [138] A. K. Au, H. Lai, B. R. Utela, and A. Folch, “Microvalves and Micropumps for BioMEMS,” *Micromachines*, vol. 2, pp. 179–220, may 2011.
- [139] B. D. Iverson and S. V. Garimella, “Recent advances in microscale pumping technologies: a review and evaluation,” *Microfluidics and Nanofluidics*, vol. 5, pp. 145–174, feb 2008.
- [140] M. Zimmermann, H. Schmid, P. Hunziker, and E. Delamarche, “Capillary pumps for autonomous capillary systems,” *Lab on a chip*, vol. 7, pp. 119–25, jan 2007.
- [141] G. M. Walker and D. J. Beebe, “A passive pumping method for microfluidic devices.,” *Lab on a chip*, vol. 2, pp. 131–4, aug 2002.
- [142] S.-H. Chao and D. R. Meldrum, “Spontaneous, oscillatory liquid transport in surface tension-confined microfluidics.,” *Lab on a chip*, vol. 9, pp. 867–9, apr 2009.
- [143] M. a. Unger, H. P. Chou, T. Thorsen, a. Scherer, and S. R. Quake, “Monolithic Microfabricated Valves and Pumps by Multilayer Soft Lithography,” *Science*, vol. 288, pp. 113–116, apr 2000.
- [144] A. Brask, D. Snakenborg, J. P. Kutter, and H. Bruus, “AC electroosmotic pump with bubble-free palladium electrodes and rectifying polymer membrane valves.,” *Lab on a chip*, vol. 6, pp. 280–8, feb 2006.
- [145] P. J. Resto, E. Berthier, D. J. Beebe, and J. C. Williams, “An inertia enhanced passive pumping mechanism for fluid flow in microfluidic devices.,” *Lab on a chip*, vol. 12, pp. 2221–8, mar 2012.
- [146] E. Berthier and D. J. Beebe, “Flow rate analysis of a surface tension driven passive micropump.,” *Lab on a chip*, vol. 7, pp. 1475–8, nov 2007.
- [147] J. Leach, H. Mushfique, R. di Leonardo, M. Padgett, and J. Cooper, “An optically driven pump for microfluidics.,” *Lab on a chip*, vol. 6, pp. 735–9, jun 2006.
- [148] S. Maruo and H. Inoue, “Optically driven viscous micropump using a rotating microdisk,” *Applied Physics Letters*, vol. 91, no. 8, p. 084101, 2007.
- [149] M. Gao and L. Gui, “A handy liquid metal based electroosmotic flow pump.,” *Lab on a chip*, vol. 14, pp. 1866–72, jun 2014.
- [150] M. Bazant and T. Squires, “Induced-charge electrokinetic phenomena: theory and microfluidic applications,” *Physical Review Letters*, vol. 92, p. 066101, 2004.

- [151] M. M. Gregersen, A. Brask, M. F. Hansen, and H. Bruus, “Flow reversal at low voltage and low frequency in a microfabricated ac electrokinetic pump,” *Physical Review E*, vol. 76, p. 056305, 2007.
- [152] H. Ren, S. Xu, and S.-T. Wu, “Liquid crystal pump.,” *Lab on a chip*, vol. 13, pp. 100–5, jan 2013.
- [153] S.-K. Fan, W.-J. Chen, T.-H. Lin, T.-T. Wang, and Y.-C. Lin, “Reconfigurable liquid pumping in electric-field-defined virtual microchannels by dielectrophoresis.,” *Lab on a chip*, vol. 9, pp. 1590–5, jun 2009.
- [154] J. Atencia and D. J. Beebe, “Magnetically-driven biomimetic micro pumping using vortices.,” *Lab on a chip*, vol. 4, pp. 598–602, dec 2004.
- [155] B. a. Malouin, M. J. Vogel, J. D. Olles, L. Cheng, and A. H. Hirska, “Electromagnetic liquid pistons for capillarity-based pumping.,” *Lab on a chip*, vol. 11, pp. 393–7, feb 2011.
- [156] Y. Chen, T.-H. Wu, and P.-Y. Chiou, “Scanning laser pulses driven microfluidic peristaltic membrane pump.,” *Lab on a chip*, vol. 12, pp. 2–5, mar 2012.
- [157] H.-Y. Tseng, C.-H. Wang, W.-Y. Lin, and G.-B. Lee, “Membrane-activated microfluidic rotary devices for pumping and mixing.,” *Biomedical microdevices*, vol. 9, pp. 545–54, aug 2007.
- [158] H. Chen, J. Cornwell, H. Zhang, T. Lim, R. Resurreccion, T. Port, G. Rosen Garten, and R. E. Nordon, “Cardiac-like flow generator for long-term imaging of endothelial cell responses to circulatory pulsatile flow at microscale.,” *Lab on a chip*, vol. 13, pp. 2999–3007, aug 2013.
- [159] H. Andersson, W. V. D. Wijngaart, P. Nilsson, P. Enoksson, and G. Stemme, “A valve-less diffuser micropump for microfluidic analytical systems,” *Sensors and Actuators B . . .*, vol. 72, pp. 259–265, 2001.
- [160] N. Nguyen and X. Huang, “Miniature valveless pumps based on printed circuit board technique,” *Sensors and Actuators A: Physical*, vol. 88, pp. 104–111, 2001.
- [161] H. Bruus, J. Dual, J. Hawkes, M. Hill, T. Laurell, J. Nilsson, S. Radel, S. Sadhal, and M. Wiklund, “Forthcoming Lab on a Chip tutorial series on acoustofluidics: acoustofluidics-exploiting ultrasonic standing wave forces and acoustic streaming in microfluidic systems for cell and particle manipulation.,” *Lab on a chip*, vol. 11, pp. 3579–3580, nov 2011.
- [162] L. Schmid, D. a. Weitz, and T. Franke, “Sorting drops and cells with acoustics: acoustic microfluidic fluorescence-activated cell sorter,” *Lab on a Chip*, jul 2014.

- [163] G. Destgeer, K. H. Lee, J. H. Jung, A. Alazzam, and H. J. Sung, “Continuous separation of particles in a PDMS microfluidic channel via travelling surface acoustic waves (TSAW).,” *Lab on a chip*, vol. 13, pp. 4210–6, nov 2013.
- [164] L. Schmid, A. Wixforth, D. a. Weitz, and T. Franke, “Novel surface acoustic wave (SAW)-driven closed PDMS flow chamber,” *Microfluidics and Nanofluidics*, vol. 12, pp. 229–235, aug 2011.
- [165] M. A. Unger, H.-P. Chou, T. Thorsen, A. Scherer, and S. R. Quake, “Monolithic microfabricated valves and pumps by multilayer soft lithography,” *Science*, vol. 288, no. 5463, pp. 113–116, 2000.
- [166] T. Thorsen, S. J. Maerkl, and S. R. Quake, “Microfluidic large-scale integration,” *Science*, vol. 298, no. 5593, pp. 580–584, 2002.

Vita

Po-Hsun Huang

EDUCATION

- 2012-2016 **Ph.D. in Engineering Science and Mechanics**
The Pennsylvania State University, University Park, PA, USA
- 2006-2008 **M.S. in Mechanical Engineering**
National Taiwan University, Taipei, Taiwan
- 2004-2006 **B.S. in Mechanical Engineering**
National Taiwan University of Science and Technology, Taipei, Taiwan
- 1999-2004 **A.E. in Mechanical Engineering**
National Kaohsiung University of Applied Sciences, Kaohsiung, Taiwan

HONORS AND AWARDS

- 2016 **PSU Distinguished Doctoral Scholar Medal**
- 2016 **PSU Alumni Association Dissertation Award**
- 2016 **The 2016 JALA Top Ten Breakthroughs of the Year Award**
- 2015 **PSU Inventor Incentive Award**
- 2013 **Chemical and Biological Microsystems Society Travel Award**

PUBLICATIONS

1. **PH Huang** *et al.*, A spatiotemporally controllable chemical gradient generator via acoustically oscillating sharp-edge structures. *Lab Chip*, 15, 4166-4176, 2015.
2. **PH Huang** *et al.*, An acoustofluidic sputum liquefier, *Lab Chip*, Vol. 15, 3125-3131, 2015.
3. **PH Huang** *et al.*, A reliable and programmable acoustofluidic pump powered by oscillating sharp-edge structures. *Lab Chip*, Vol. 14, 4319-4323, 2014.
4. **PH Huang** *et al.*, An acoustofluidic micromixer based on oscillating sidewall sharp-edges. *Lab Chip*, Vol. 13, 3847-3852, 2013.
5. **PH Huang** *et al.*, A Single-Layer, Planar, Optofluidic Switch Powered By Acoustically Driven, Oscillating Microbubbles. *Appl. Phys. Lett.*, Vol. 101, 141101, 2012.
6. **PH Huang** *et al.*, Bubble-free large area replication of microstructures using gas-assisted UV embossing with modified reversal imprinting and gap-retained vacuuming. *JVST-B*, Vol. 31, 031602, 2013.
7. N Nama, **PH Huang** *et al.*, Investigation of micromixing by acoustically oscillated sharp-edges. *Biomicrofluidics*, Vol. 10, 024124, 2016.
8. N Nama, **PH Huang** *et al.*, Investigation of acoustic streaming patterns around oscillating sharp-edges. *Lab Chip*, Vol. 14, 2824-2836, 2014
9. CY Chan, **PH Huang** *et al.*, Accelerating drug discovery via organs-on-chips. *Lab Chip*, Vol. 13, 4697-4710, 2013.